UNIVERSITÀ
DEGLI STUDI
DI TRIESTE

UNIVERSITÀ DEGLI STUDI DI TRIESTE

XXXVII CICLO DEL DOTTORATO DI RICERCA IN

NANOTECHNOLOGY

ARCHITECTED MATERIALS FOR FUNCTIONAL PROPERTIES

Settore scientifico-disciplinare: **ING-IND/22**

DOTTORANDO
SYED ABDUL BASIT SHAH

COORDINATORE
PROF. ALBERTO MORGANTE

SUPERVISORE DI TESI
PROF. VANNI LUGHI

CO-SUPERVISORE DI TESI
PROF. CHRISTIAN KLINKE
(UNIVERSITY OF ROSTOCK)

ANNO ACCADEMICO 2024/2025

Abstract

This thesis investigates the influence of nanomaterial morphology and interfacial engineering on charge transfer dynamics in a heterostructure system. The study begins with a systematic evaluation of TiO_2 nanoparticles and nanotube arrays (TNTAs), revealing that anatase-phase TNTAs with an optimized height of 8 μm exhibit superior hydrogen evolution reaction (HER) activity, driven by enhanced charge transport pathways and suitable morphology. Subsequently, the role of surface chemistry in governing interfacial charge transfer was explored using $CsPbBr_3$ perovskite nanocrystals (PNCs) with controlled ligand chain lengths. Short-chain ligands facilitated more effective electron transfer to TiO_2 nanostructures, with nanotube arrays outperforming nanoparticle films in solid-state configurations. Mn-doped perovskites further highlighted the morphology-dependent quenching behaviour of TiO_2, though deeper insights into charge carrier dynamics require advanced spectroscopic techniques. Finally, CdTe/CdSe core–shell quantum dots were interfaced with TiO_2 morphologies, revealing contrasting behaviours between solution and thin-film phases. In solution, TiO_2 nanoparticles promoted stronger quenching, while in thin films, TNTAs enabled more efficient charge extraction and directional transport leading to efficient photocatalytic degradation of aqueous Rhodamine B dye. Collectively, this work demonstrates that fine-tuning nanomaterial morphology, phase, and surface chemistry is critical to optimizing charge transfer processes and photocatalytic activity. The insights gained may provide a pathway for designing high-performance, hybrid nanostructures for photocatalysis and other optoelectronic applications.

Abstract in Italian

Questa tesi analizza l'influenza della morfologia dei nanomateriali e dell'ingegneria interfacciale sulla dinamica del trasferimento di carica in sistemi eterostrutturati. Lo studio inizia con una valutazione sistematica di nanoparticelle di TiO_2 e di array di nanotubi di TiO_2 (TNTAs), rivelando che i TNTAs in fase anatase con un'altezza ottimizzata di 8 μm mostrano un'attività superiore nella reazione di evoluzione dell'idrogeno (HER), grazie a percorsi di trasporto di carica migliorati e a proprietà elettroniche favorevoli. Successivamente, è stato esplorato il ruolo della chimica superficiale nel controllo del trasferimento di carica interfacciale utilizzando nanocristalli di perovskite $CsPbBr_3$ (PNCs) con lunghezze di catena dei leganti controllate. I leganti a catena corta hanno facilitato un trasferimento elettronico più efficiente verso le nanostrutture di TiO_2, con gli array di nanotubi che hanno superato le pellicole di nanoparticelle nelle configurazioni allo stato solido. Le perovskiti drogati con Mn hanno ulteriormente evidenziato il comportamento di quenching dipendente dalla morfologia del TiO_2, sebbene approfondimenti più dettagliati sulla dinamica dei portatori di carica richiedano tecniche spettroscopiche avanzate. Infine, i quantum dots core–shell CdTe/CdSe sono stati interfaccati con morfologie di TiO_2, rivelando comportamenti contrastanti tra le fasi in soluzione e in film sottile. In soluzione, le nanoparticelle di TiO_2 hanno promosso un quenching più marcato, mentre nei film sottili, i TNTAs hanno consentito un'estrazione di carica più efficiente e un trasporto direzionale, portando a una degradazione fotocatalitica efficace del colorante Rhodamine B in soluzione acquosa. Complessivamente, questo lavoro dimostra che l'ottimizzazione della morfologia, della fase e della chimica superficiale dei nanomateriali è fondamentale per migliorare i processi di trasferimento di carica e l'attività fotocatalitica. Le conoscenze acquisite offrono una strada per la progettazione di nanostrutture ibride ad alte prestazioni per la generazione fotocatalitica di idrogeno e per applicazioni optoelettroniche correlate.

Acknowledgements

First and foremost, I thank Allah for guiding me throughout this journey and enabling me to pursue this path.

I am deeply grateful to my parents and family, whose unwavering support and love have been my foundation throughout my life. I cannot express enough gratitude for everything they have done for me.

I would like to extend my heartfelt thanks to my supervisor, Professor Vanni Lughi, for his invaluable guidance, trust in my research choices, constant dedication and support. I am truly grateful for his mentorship and a very dear friendship.

I also wish to thank my co-supervisor, Professor Christian Klinke, with whom I had the pleasure of collaborating during my Erasmus exchange at the Institute of Physics, University of Rostock. I am sincerely grateful for his support, mentorship, fruitful collaboration, and the dedication he devoted.

This Erasmus journey was not only part of my PhD but also began during my master's when I spent a year at Department of Metallurgical and Materials Engineering, Sakarya University in Turkey under the supervision of Professor Mehmet Oğuz Güler. That experience laid the foundation for my research ideas and helped shape my academic path. My heartfelt thanks to Professor Güler and his research group for accepting me, hosting my research stay and providing training on technical equipment.

Additionally, I would like to thank Professor Patrick Schmuki of the University of Erlangen-Nürnberg, where I had the opportunity to spend a month in his lab as an Erasmus exchange student. I learned a great deal during that time, and I am thankful for the knowledge and experience he provided.

I would also like to express my gratitude to the coordinator and deputy coordinator of the PhD Nanotechnology School, as well as to the reviewers of my PhD thesis, for their guidance and feedback.

A special thanks to Dr. Sushant Ghimire, Dr. Rostyslav Lesyuk and Dr. Luca Cozzarini for their insightful contributions and support.

I am also grateful to all my colleagues and friends, at the Universities of Trieste and Rostock, especially those I shared the PhD office with over the past three and a half years. Your support and camaraderie have been invaluable.

Thank you all from the bottom of my heart.

Syed Abdul Basit Shah

Table of Contents

List of figures

List of tables

Motivation for this work

The modern world faces a growing set of environmental challenges largely driven by human activities mainly the reliance on fossil fuels for energy. The burning of coal, oil, and natural gas releases large quantities of greenhouse gases such as carbon dioxide (CO_2) and methane (CH_4), which trap heat in the atmosphere and contribute significantly to global warming. As a result, we are witnessing rising global temperatures.

One of the key approaches to address these environmental challenges is reducing greenhouse gas emissions by transitioning away from fossil fuels and adopting low-carbon or carbon-neutral energy sources. This could be achieved by transitioning to green energy which is derived from renewable and sustainable sources such as solar, wind, hydro, geothermal, and biomass. Green energy produces little to no greenhouse gas emissions during operation and is often less damaging to the environment.

Among the many green energy solutions, carbon neutral fuels (produced by converting CO_2 back to fuels) and hydrogen have emerged as promising clean fuels due to high energy content and zero emissions when used. However, producing these fuels in an environmentally friendly way remains a challenge. One of the most promising and sustainable methods is photocatalysis. This process uses sunlight and a semiconductor material known as a photocatalyst to drive the chemical reaction that can initiate reaction for CO_2 conversion and splitting water (H_2O) into hydrogen (H_2) and oxygen (O_2).

Photocatalysis offers several advantages:

- It uses abundant solar energy, a free and renewable resource.
- It relies on raw material that is widely available.
- It produces clean fuels without emitting greenhouse gases or pollutants.

Research into TiO_2 as a photocatalysts is ongoing to improve the efficiency, stability, and scalability of this technology. One of the ways to improve the efficiency is by combining TiO_2 with nanomaterials which improve the ability of TiO_2 to absorb more solar energy and produce hydrogen more effectively. This thesis investigates the interaction mechanisms between TiO_2 with varying morphologies and distinct classes of nanomaterials specifically nanocubes, nanosheets, and quantum dots, under different experimental conditions to determine optimal performance parameters. The nanomaterials are produced through colloidal synthesis and are introduced to TiO_2. These nanomaterials, capable of absorbing solar energy, act as photosensitizers and transfer the harvested energy to TiO_2 upon contact. As a result, the effective solar energy input for photocatalytic hydrogen production is enhanced compared to bare TiO_2.

We explore perovskite and II-VI semiconductor as potential nanomaterials. As part of the research presented in this thesis, a peer-reviewed manuscript titled *"Tailoring Charge Donor–Acceptor Interaction in $CsPbBr_3$ Perovskite Nanocrystals through Ligand Exchange"* was published in *Small Science* in 2024. This work focuses on modifying the surface chemistry of $CsPbBr_3$ perovskite nanocrystals via ligand exchange to systematically tune charge donor–acceptor interactions.

Based on my background as a Mechanical engineer, the knowledge obtained from this study will be utilized to scale up solar energy harvesting systems.

Thesis overview

This thesis is divided into 6 chapters

Chapter 1 This chapter introduces nanomaterials, describing their optical properties under the quantum confinement effect and provides material classification by bandgap. It discusses photoluminescence (steady-state and time-resolved), synthesis via nucleation theory, and the role of surface ligands. The chapter also examines photocatalysis, using TiO_2 as a model system, explores nanoheterostructures and charge transfer, and proposes modifications to enhance TiO_2 photocatalytic performance. It concludes by identifying knowledge gaps and defining the study's objectives.

Chapter 2 This chapter focuses on the comparative evaluation of hydrogen evolution performance across different TiO_2 morphologies. It begins by detailing the fabrication process of TiO_2 nanotube arrays and the subsequent platinum photodeposition technique. The chapter then examines variations in photocatalytic activity among TiO_2 morphologies and ultimately compares the photocatalytic performance of anatase-phase TiO_2 nanotube arrays having different heights.

Chapter 3 This chapter investigates the role of perovskite nanocubes (PNC) surface chemistry in tuning charge transfer within Perovskite/TiO_2 systems. It presents the hot-injection synthesis of PNCs followed by post-synthetic ligand exchange to tailor surface properties. The chapter systematically examines PNC–TiO_2 interactions in both colloidal dispersions and thin-film architectures. Finally, it evaluates the interfacial behaviour of PNCs with TiO_2 nanotube arrays.

Chapter 4 This chapter presents the interactions between Mn doped $CsPbBr_3$ and different morphologies of TiO_2. It sheds light on variation in charge carrier dynamics of bulk and surface doped Mn atoms of these systems upon introduction of nanoparticles, nanotubes and nanorods of TiO_2 in liquid phase and thin film phase. Finally, it briefly demonstrates the UV to visible down conversion capability of these materials.

Chapter 5 This chapter deals with utilizing the concept of wave function engineering to prolong the charge carrier lifetime in core-shell structures and study the charge transfer in core-shell/TiO_2 systems. It examines the interactions between the CdTe-CdSe core-shell structures and TiO_2 (nanoparticles and nanotubes) in liquid and thin film configurations. Furthermore, it demonstrates the enhanced photocatalytic behaviour of as a result of these interactions.

Chapter 6 This chapter summarizes the overall outcomes and provides conclusive remarks on the thesis work.

1 Introduction

1.1 Nanoscale

The nanoscale encompasses structures and phenomena occurring within the dimensional range of 1 to 100 nanometres (nm), where 1 nm = 10^{-9} meters. As reported by[1], this size nearly corresponds to three to five atoms in width (having size less than 10 Å) or roughly to a few de Broglie wavelengths. At this scale, materials exhibit unique properties that differ significantly from their bulk counterparts, due to quantum effects and increased surface area-to-volume ratios.

1.2 Nanomaterials and their optical properties

As discussed in the previous section, nanomaterials develop certain unique properties due to quantum effects. In case of semiconductor materials, these properties are determined by the size and shape and play dominant role in the determining the optoelectronic performance of the materials. This is due to a phase change that occurs when bulk materials are converted into nanomaterials. [2] et al classify nanoscale matter as a separate state of matter, other than solid, liquid, gas and plasma.

European Commission and ISO/TS 80004 define 'nanomaterial' as a material with 50% or more of the particles in the number size distribution, and it should have at least one dimension in the range of 1-100 nm[3], [4], [5]. This gives rise to different morphologies of nanostructures such as 0D, 1D and 2D. The 0D nanostructures have all three dimensions under 100 nm such as spherical nanoparticles (quantum dots), 1D have at least two dimensions under 100 nm like nanofibers and nanorods or nanowires, and 2D have only one dimension in the 'nanomaterial' range which include nanosheets and nanolayers or thin films. There is another category here, called 3D nanomaterials, which are not actually nanomaterials in terms of size range but have structures that correspond to nanoscale range. In any case, the described morphologies of nanomaterials lead to different applications, which are specific to a particular shape and size. This is a consequence of quantum confinement effect, which is discussed below.

1.2.1 Band theory of solids and the quantum confinement effect

According to band theory of solids [6], during the formation of material, atoms come together and start bonding. This process of bonding is dominated by splitting and overlapping of orbitals leading to formation of conduction and valence bands. The difference between these two bands is referred to as 'bandgap' (Eg) and based on it, the solids are classified into three types, conductors (mostly metals), semiconductors and insulators, as shown in the Figure 1.1 below

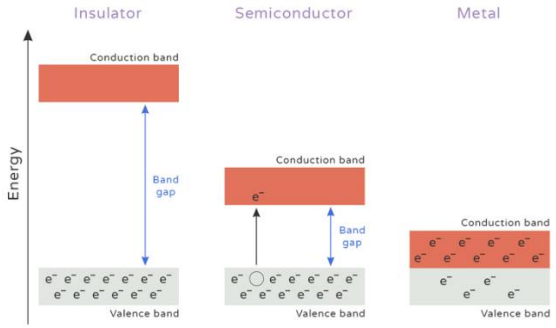

Figure 1.1) Classification of materials based on bandgap

In case of conductors, there is effectively no bandgap (0 eV), and electrons can move freely against the applied potential. On the contrary, insulators have a large E_g value and hence electrons do not move against any photo or electric potential. For semiconductor materials, the bandgap is sufficiently small enough so that an incoming photon of light, or an applied electric potential can excite the electron to the conduction band, leaving behind a hole in the valence band. These electron and holes recombine either by radiative or non-radiative paths.

If the size of material is allowed to increase, the splitting and overlapping of orbitals proceeds and results in formation of continuous dense bands of energy. The electrons and holes can freely move through these energy levels in conduction and valence band, respectively. On the other hand, if the growth of the material is restricted to few hundred of atoms (<100 nm), then non-continuous energy levels without any continuation appear. Thus, electrons and holes are only allowed to move to particular energy levels, known as quantized states. This phenomenon is called quantum confinement effect, as shown in the figure 1.2 below

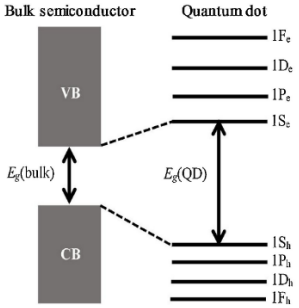

Figure 1.2) Bulk semiconductor vs nanocrystals, copied from [7]

The smaller is the size of the structures, lesser are the energy levels formed and the smaller is the confined space for electrons and holes to occupy, hence large is the energy difference between the quantized states. The origin of quantized states in relation to the morphological shape shown in the Figure 1.3 below

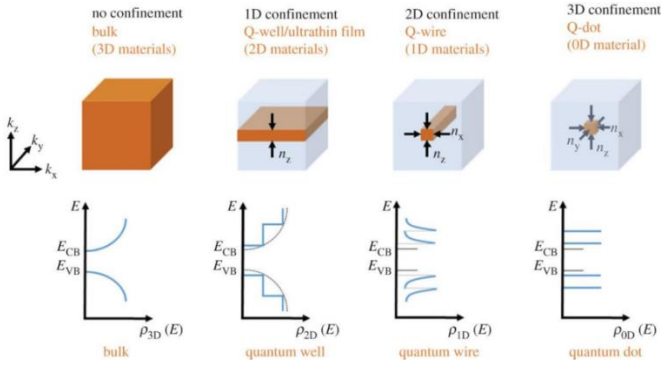

Figure 1.3) Quantum confinement depending on the shape of nanostructures, copied from [8]

As evident, the band energy structure for each shape varies and it depends on the degree of confinement.

For 0D spherical nanomaterials such as quantum dots (QDs) which are confined in all directions, the size should not exceed the Bohr exciton radius of the corresponding bulk material[9]. Under these conditions, sharp and discrete energy levels known as quantum size levels (QSLs) appear. For 1D and 2D nanomaterials, same condition applies to the size of the direction in which quantum confinement appears. This quantized states in the 0D QDs are more discreate, hence no electrons can move freely in any direction and the QDs starts to mimic an 'atom'. In comparison, the 1D and 2D nanomaterials show confinement in only specific directions. The energy of the QSLs of QDs is governed by the following equation:

$$E_{l,n}^{e,h} = \frac{h^2 \Phi_{l,n}{}^2}{2m_{e,h}d^2} \quad 1\text{-}1$$

Here, $m_{e,h}$ represents the electron and hole effective masses, d is the crystal size and $\Phi_{l,n}$ is the n^{th} root of spherical Bessel function of order l.

In any case, the evolution of quantized states allows the semiconductor nanostructures to absorb certain wavelengths of light to generate charge carriers, which if recombine through radiative recombination emit at particular higher wavelengths.

1.2.1.1 Direct and indirect bandgap

As discussed above, semiconductors experience exciton formation under irradiation of certain wavelength of light. This photo excitation transition obeys the selection rule dominated by Bloch wavefunction, where momentum has to be conserved. In this wavefunction, energy is plotted as function of electron momentum (quantum number, k). If the conduction band minima have the same electron momentum 'k' as the valence band maxima, the semiconductor is classified as a direct bandgap. On the contrary, different 'k' value lead to indirect bandgap. For radiative recombination, semiconductors should have a direct band gap[10], as shown in Figure 1.4

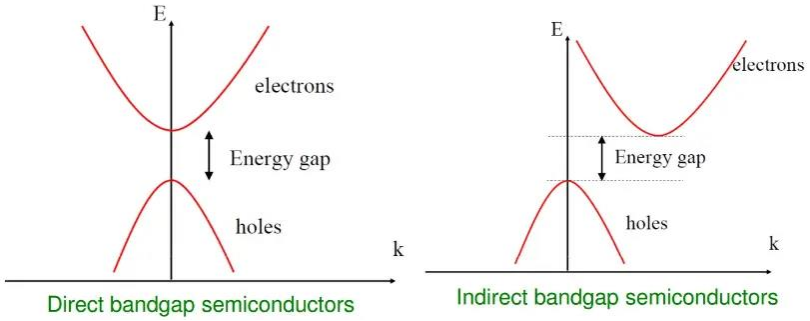

Figure 1.4) Direct and Indirect band gap semiconductors

1.2.2 Absorption Spectra

Absorption is a typical feature of nanomaterials and is plotted as absorbance vs wavelength (nm) which is representative of photon energy. It can be defined in mathematical terms as

$$A = log_{10}\left(\frac{I_o}{I}\right) \quad 1\text{-}2$$

Where I_o and I are incident light intensity and transmitted light intensity, respectively. For nanocrystals of semiconductor materials, the absorption spectra indicate the position of excitonic absorption peaks, corresponding to the quantized energy states. The first excitonic peak (FEP) corresponds to the excitation of an electron from the valence band to the conduction band. A typical absorption spectra and its corresponding quantized states are shown in Figure 1.5 below

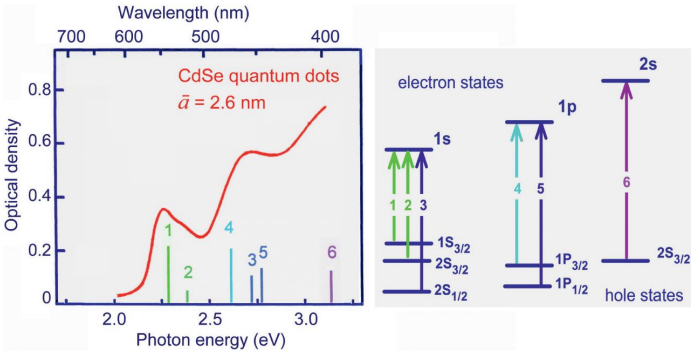

Figure 1.5) Typical absorption spectra of CdSe QDs and its corresponding quantized states, copied from [11]

The position of FEP along the wavelength (nm) indicates the diameter in case of QDs and thickness of material in case of nanosheets. Small sized QDs and thinner nanosheets have strong confinement, hence the larger bandgap and corresponding FEP is blue shifted compared to large QDs or thicker nanosheets. The dependence of Eg on size or thickness of nanostructures is shown in the Figure 1.6 below

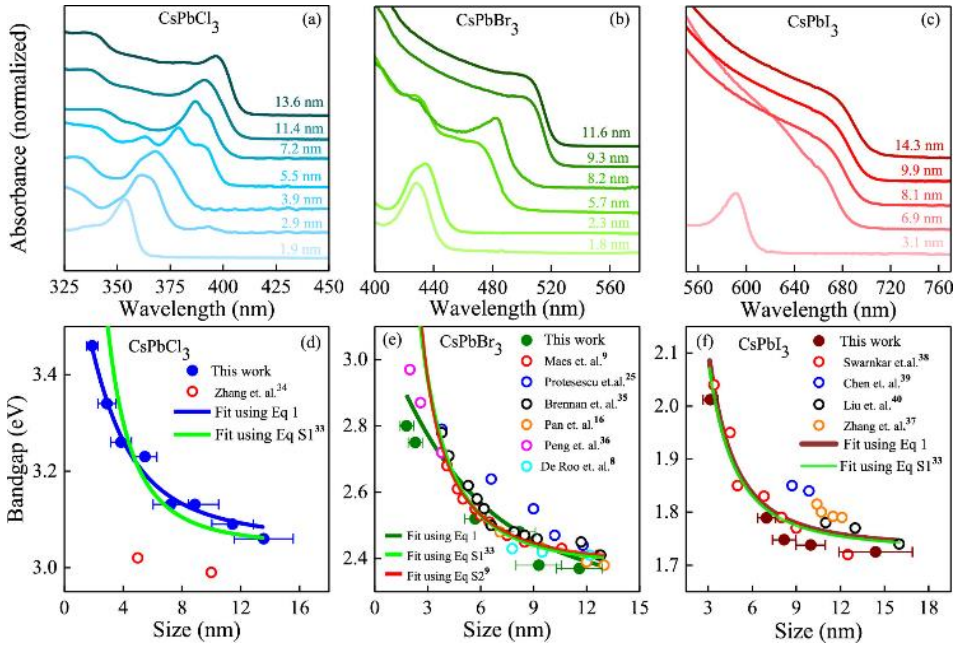

Figure 1.6) Absorption spectra for CsPbX3 QDs (X=Cl, Br, I) corresponding to variation in size, copied from [12]

The optical Eg of semiconductor nanocrystals is determined by Tauc plot, represented by equation below

$$(\alpha h\nu)^n = A(h\nu - E_g) \qquad 1\text{-}3$$

α = absorption coefficient, hν = photon energy, Eg = optical band gap, and n = ½ for direct band gap, 2 for indirect band gap materials.

1.2.3 Steady state Photoluminescence (PL) emission

A particular distinctive feature of nanomaterials is their ability to emit photons of light at certain wavelengths, depending on the Eg size. This emission is always red shifted compared to absorption peak and it is called Stokes shift. Its evolution is attributed to the difference in the singlet and triplet state of the nanocrystals. As the electron is excited to the singlet state in conduction band, it cools down the edge of CB edge by thermalizing with the lattice of the nanocrystal. This leads to loss of energy and hence the red shift in emission spectra.

Its magnitude is inversely related to the size of the nanocrystals. Brennan et al [13] reported that the relationship of stokes shift to size of nanocrystal is dominated by changes in intrinsic electronic structure due to change in quantum confinement, as shown in Figure 1.7 below

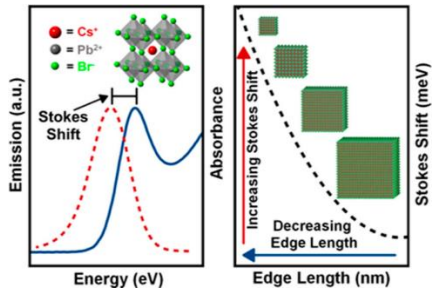

Figure 1.7) Stokes shift and its dependence on size of $CsPbBr_3$ QDs, copied from [13]

1.2.4 Time resolved photoluminescence

Time-resolved photoluminescence (TRPL) is a technique used to measure the dynamics of photoexcited states—typically excitons—in nanomaterials such as QDs and 2D materials. It provides detailed insights into recombination lifetimes, energy and charge transfer processes. It tracks the PL intensity decay over time, after the nanocrystals are excited by a short excitation pulse of a certain frequency. This decay plotted against time reveals a decay profile that shows at how long it takes for the electrons and holes to recombine. For nanostructures such as QDs and 2D materials, this measurement spans from a few hundred picoseconds to tens of nanoseconds. These values of time are obtained by fitting the decay profile by suitable exponential decay function.

1.2.5 Photoluminescence Quantum Yield (PLQY)

It is a fundamental metric that describes the efficiency of photon emission from a nanocrystal after it is excited by photon of light. It represents the percentage of charge carriers that recombine through radiative recombination and is represented by the formula

$$\text{PLQY} = \frac{Number\ of\ photons\ emitted}{Number\ of\ photons\ absorbed} \qquad 1\text{-}4$$

Materials with high quantum yield have less defects and trap states in the band gap, therefore a lower non-radiative recombination. Such materials are suitable for optical applications.

1.3 Colloidal synthesis of Nanomaterials

It is a bottom up, wet chemical reaction designed for synthesis of nanomaterials in a liquid media, preferably a non-coordinating solvent, to have a controlled and nearly uniform size, shape and chemical composition. The atoms of the chemical precursors react in the liquid media, and aggregate to form 'nuclei' which act as seeds for growth of nanoparticles. This phase of the reaction is called nucleation phase, and it is followed by the growth phase where the atoms start to grow on the nucleated seeds to increase the size of nanoparticles. This reaction takes place in the presence of ligands which act as stabilizing agents to prevent the agglomeration of nanoparticles. The reaction kinetics of a colloidal synthesis are governed by the nucleation theory.

1.3.1 Nucleation theory for Quantum dots

To synthesize a monodisperse and uniform sized colloidal solution of quantum dots, the nucleation phase should be brief and discrete like a 'burst', followed by a slow and steady growth phase, according to LaMer model [14]. This emphasizes that if nucleation phase only appears for a brief moment and ceases during the growth phase, the final particles will have most uniform size and a narrow size distribution. On the contrary, if both the phases persist at the same time, it would lead to broad size distribution and hence different sized populations of nanostructures. The Figure 1.8 below shows the La Mer plot.

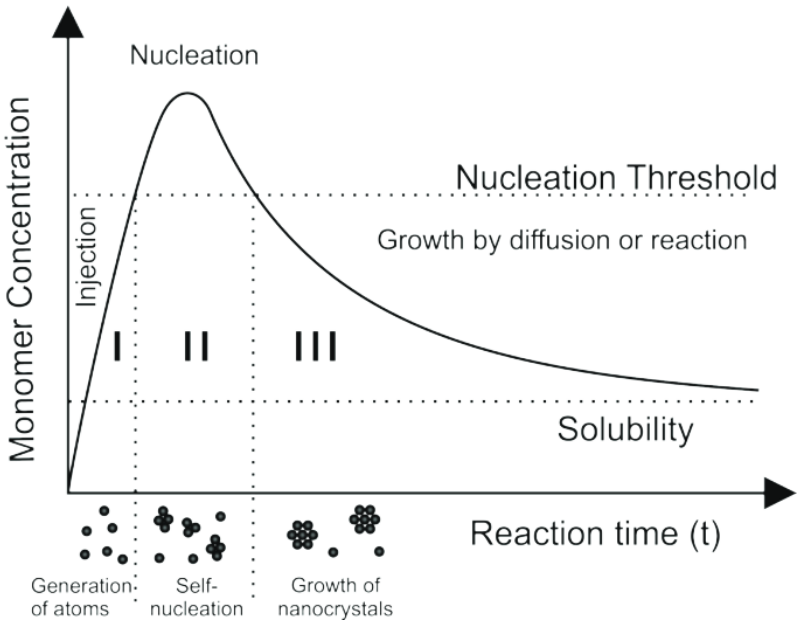

Figure 1.8) Representation of La Mer nucleation theory, copied from [15]

To have a burst nucleation event is an important factor for growth of uniform sized QDs. The Gibbs free energy change ΔG for 0D spherical QDs formation of radius 'r' can be calculated by

$$\Delta G = 4\pi r^3\gamma + \frac{4}{3}\pi r^3 \Delta G_v \qquad 1\text{-}5$$

Where,

γ = surface free energy per unit area
$\Delta G_v = -RT \ln S/V_m$

The ΔG_v plotted against radius 'r' shows a maximum called critical radius 'r_C'. In order for a nuclei to form, its radius should be greater than r_C, calculated by the equation

$$r_c = \frac{2\gamma V_m}{RT\ lnS} \qquad 1\text{-}6$$

Here, V_m and S represent the molar volume of the bulk material and the supersaturation of the solution, respectively. Therefore, a lower value of r_C can facilitate homogeneous nucleation, and it can be attained by high concentration of precursors.

Here it is essential to mention that the thermodynamic barrier for homogeneous nucleation is greater as compared to heterogeneous nucleation. Therefore, the latter can occur at lower concentrations and/or lower temperatures. The change in Gibbs free energy for heterogeneous nucleation can be represented by formula

$$\Delta G_{hetrogeneous\ nucleation} = \Delta G_{homogeneous\ nucleation}\ \text{x}\ f(\theta) \qquad 1\text{-}7$$

θ represents the contact angle between the surface of nucleating crystal and the existing surface. Higher is the θ, lower is the interfacial tension between the growing material and the nucleating crystal, and hence less lattice mismatch. Heterogeneous nucleation occurs more conveniently if the lattice mismatch is low.

1.3.2 Single Phase and multiphase nanocrystals

As evident from their name, single phase nanocrystals contain one phase only. The size of single-phase quantum dot can be related to its band gap (E_{gNC}) and its bulk bandgap (E_{GBULK}) by Brus equation [16]

$$E_{GNC} = E_{GBULK} + \frac{h^2}{2r^2}\cdot\left(\frac{1}{m_e}+\frac{1}{m_h}\right) - \frac{1}{r}.\frac{1.8e^2}{\varepsilon} \qquad 1\text{-}8$$

where E_{Gbulk} is the bandgap of the bulk material, m_e and m_h are electron and hole effective masses,

h the Planck's constant, e the elementary charge and ε the absolute permittivity of bulk material.

The Figure 1.9 below depicts the relationship between bandgap of a spherical QD semiconductor nanostructure and its size

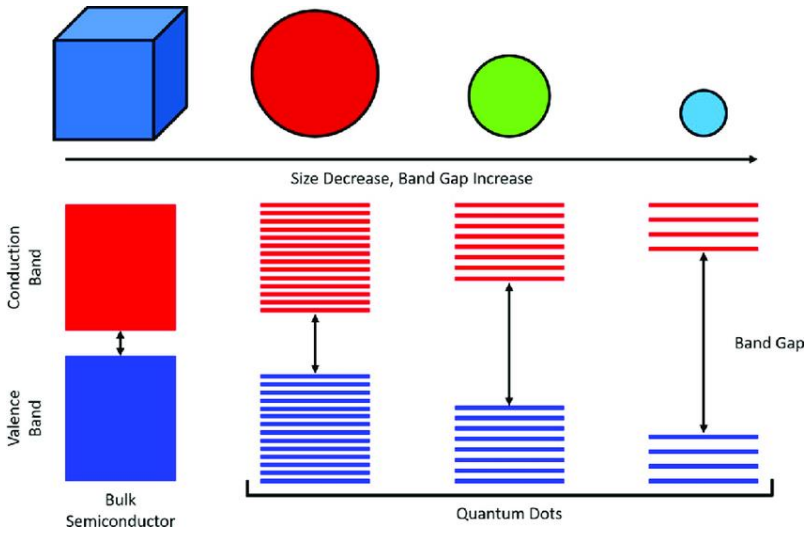

Figure 1.9) Dependence of QDs bandgap on size

Multiphase nanocrystals are composed of two more than two semiconductor materials in a 'core-shell' or 'core-multishell' configuration. Due to the presence of different materials, the optical properties of these materials are determined by the combination size and chemical composition of both the core and the shell. Therefore, Brus equation cannot be used to determine the bandgap of multiphase nanocrystals. The inner core and shell materials should have minimum lattice mismatch for low interfacial strain.

The shell in the multiphase materials acts as a protective barrier for core [17], [18], from the surrounding media in addition to curing the surface defects. This leads in increase in radiative recombination of charge carries. The choice of core and shell material based on their band alignment could be utilized to tailor the charge carrier dynamics of the nano-heterostructure, and eventually, the absorption, steady state PL and TRPL and PLQY. Based on the band alignment between the core and the shell, multishell materials can be divided into two categories

1.3.2.1 Type-I core-shell heterostructures

The band of shell material is larger than the core material and the conduction and valence bands of core lie within the band gap of shell. Since electron prefer to reside in lowest energy state, and holes prefer

to be in higher energy state, this configuration allows for electrons and holes to be confined in the core due to its lower CB level and higher VB level. This leads to enhanced band edge (B.E) recombination in core, and lower defect states, hence the rate of radiative recombination increases and of non-radiative recombination decreases, resulting in higher PLQY. In summary, the electron and hole wavefunction are forced to overlap, as shown in Figure 1.10

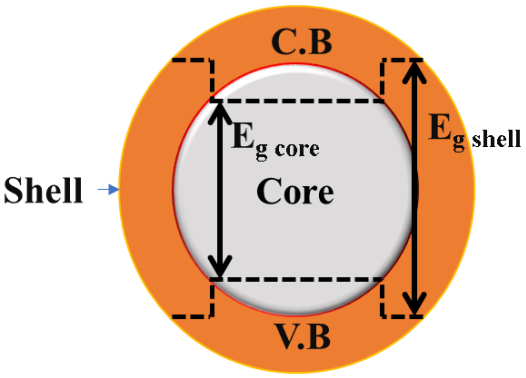

Figure 1.10) Type I core-shell QD structure

1.3.2.2 Type-II core-shell heterostructures

This configuration has a staggered band alignment, in which either one, out of the conduction band or the valence band, of the core material lies in between the conduction band and valence band of shell material. The band alignment leads to spatial separation of charge carries, in a way that the wavefunctions of electrons and holes are not overlapping and are localized in two different regions. This leads to prolonged lifetime of charge carries, and the probability of scavenging of carriers increases. The localization of wavefunctions depends on the relative positions of conduction band of core to the conduction band of shell, as shown in Figure 1.11.

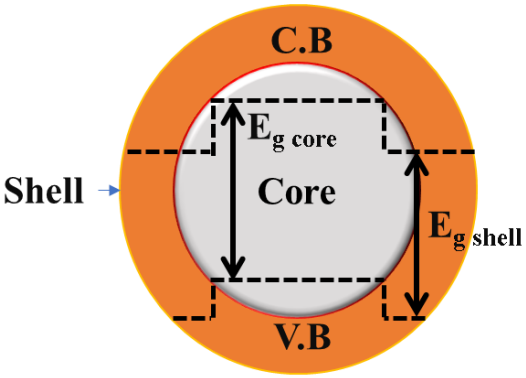

Figure 1.11) Type-II core-shell QD structure

1.3.3 Colloidal Synthesis techniques for nanostructures

Here we discuss the synthesis techniques used in this work

1.3.3.1 Single phase nanocrystals

1.3.3.1.1 Hot injection

The Bawendi group [19] pioneered this method involving the swift injection of precursors into a heated solvent, causing a sudden surge in monomer concentration that exceeds the threshold for homogeneous nucleation. This rapid burst leads to an intense but brief nucleation phase, during which monomer levels quickly drop, slowing down further nucleation activity. If the rate of precursor supply does not surpass its consumption, additional nuclei will not form—favouring growth on already existing particles instead

of new nucleation. This technique has become a standard approach for producing high-quality semiconductor nanocrystals.

1.3.3.2 Multiphase core-shell structures

Epitaxial shells on pre-synthesized core nanocrystals can be developed by keeping in view the following points

a) The lattice mismatch value between the core and the shell material should be as low as possible. A higher lattice mismatch leads to interfacial strain and degrades the core-shell nanostructure quality.
b) The temperature should be optimal for shell growth only. Higher temperature might lead to either alloying of core and shell material or homogeneous nucleation of a second phase
c) The rate of shell precursor addition should be slow, so that the concentration of precursors in the reaction mixture do not surpass the minimum limit for homogeneous nucleation

1.3.3.2.1 Successive ionic layer adsorption and reaction

Li[20] et al. were the first to introduce the Successive Ion Layer Adsorption and Reaction (SILAR) approach, a stepwise deposition method where precisely measured amounts of shell precursors are added one after another. This alternating injection strategy enables near-monolayer precision in building up the shell structure, layer by layer. By minimizing the simultaneous presence of both cationic and anionic species in the solution, the SILAR technique significantly reduces the risk of undesired homogeneous nucleation. Additionally, it provides excellent control over the development of optical characteristics throughout the process. This method typically results in particles with a more uniform size and supports the fabrication of a wide range of nanostructured materials.

1.3.3.2.2 Non injection technique

In this strategy, both the shell precursors are introduced into a dispersion of as synthesized core nanocrystals at ambient conditions. Following this, the entire mixture is gradually brought to the desired reaction temperature. If reaction conditions—such as temperature, concentration, and ligand environment—are carefully optimized, the shell material preferentially nucleates epitaxially on the surface of the existing cores rather than nucleation of a second nanocrystals phase composed solely of the shell constituents. This method significantly simplifies the fabrication of complex, multiphase nanocrystals by reducing procedural complexity and limiting second phase nucleation. However, its applicability is system-dependent; not all core–shell combinations are compatible with this technique due to differences in lattice mismatch, interfacial energy, or precursor reactivity, which can lead to undesired nucleation or poor shell growth.

1.3.4 Surface ligands

They play crucial role in determining the nucleation and growth of nanocrystals, depending on the strength of ligand binding. A stronger binding leads to less homogeneous nucleation and larger particles. The facet-specific binding of ligands to the nanocrystals leads to desired shape control. After the synthesis, they provide steric hindering and prevent aggregation of nanocrystals. Depending on the size and shape of ligand, they can provide surface passion and suppress the defects by interacting with the dangling bonds. In addition, the extent of interaction of nanocrystal with the surrounding environment is also meditated by ligands. Finally, the ligands determine the dispersion of nanocrystals in the solvent.

1.3.4.1 Ligand exchange process

This is the process of substituting the existing ligand with another[21]. As discussed earlier, the size and shape of nanocrystals is determined by the surface ligands. For post synthesis applications, the surface chemistry needs alteration, and it is achieved by changing the encapsulation of ligands. This is

accomplished by exposing the nanocrystals to high concentration of desired ligands for a particular time to ensure the original ligands are replaced. The process can be repeated several times to ensure complete exchange of ligands. This is followed by a cleaning process of exposing the ligand exchanged nanocrystals to a mix of polar and non-polar solvents to promote the phase separation and obtain the ligand exchanged nanocrystals. The nature of surface ligands can be characterized by Fourier Transform Infrared Spectroscopy (FTIR).

1.4 Photocatalysis

Photocatalysis is the process of utilizing solar energy to excite the charge carriers in a semiconductor catalyst for redox reactions with the surrounding media under appropriate conditions. In essence, a photocatalyst provides activation energy required for the chemical reaction to proceed by creating favourable pathways for a reactant to be converted into a product (photoredox reaction).

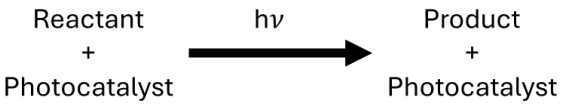

These photoredox reactions occur at the surface of semiconductor material having the minimum potential energy level in a nano-heterostructure (lower reduction potential for electrons and lower oxidation potential for holes). Typically, such reactions are carried out in an aqueous media.

1.4.1 Influencing factors

Generally, higher number of charge carriers generated results in higher photocatalytic activity, therefore, semiconductor nanostructures with E_g small enough to allow generation of electron and holes under visible light irradiation are considered to be ideal candidates, as demonstrated by Schmuki et al [22] and Verbruggen et al [23].

In addition, the following parameters are crucial for the photocatalytic activity

i. Surface traps
ii. Reactivity
iii. Photo adsorption of the reactants and desorption of the products
iv. Relative energy levels suitable for photoredox reactions to occur also determine the final efficiency
v. Transport of the reactant to and from the photocatalyst surface

Out of the above-mentioned factors, point (v) depends on the surrounding media, whereas the rest of the factors strongly depend on the morphology, electronic structure as well as the crystal structure of the photocatalyst. Figure 1.12 shows commonly used photocatalysts

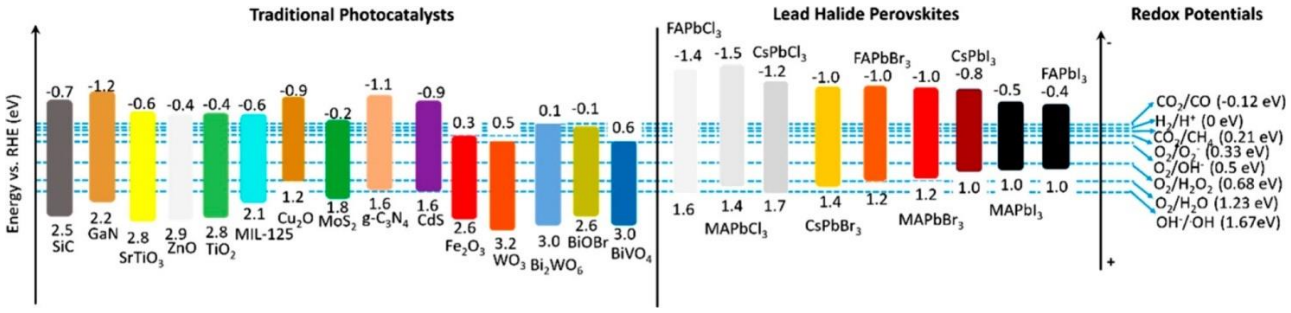

Figure 1.12) Some well-known photocatalysts, copied from [24]

1.4.2 Titanium dioxide as a photocatalyst

Titanium dioxide (TiO_2-Titania) is well known photocatalyst, extensively studied for its application in photocatalysis due to its reactivity, stability, durability, non-toxic nature and low cost synthesis [25]. Its physical and chemical properties are highly dependent on its crystalline phase, morphology, and electronic structure.

1.4.2.1 Crystal structure of TiO_2

TiO_2 exists primarily has three crystal structures, anatase, rutile and brookite. All three phases are fundamentally composed of TiO_6 octahedra, where Ti^{4+} ions are coordinated by six O^{2-} anions, forming Ti–O bonds arranged in distinct structural configurations[26], [27].

In the anatase phase, these octahedra share vertices, giving rise to a tetragonal crystal structure. A similar tetragonal structure is found in the rutile phase; however, it is characterized by edge-sharing of octahedra along the (001) planes. In contrast to the previous two, the brookite phase exhibits a more complex orthorhombic structure, where both edge- and vertex-sharing of octahedra occur.

These crystal structures have been extensively studied for a wide range of technological applications. Among these, rutile and anatase are of particular significance in photocatalysis for solar energy conversion processes, including photocatalytic water splitting and pollutant degradation. Anatase is especially noted for its superior photocatalytic activity as compared to rutile[28], [29]. This is attributed to the higher specific surface area, resulting from its smaller crystallite size, which provides a greater density of reactive surface sites—particularly those exposed on the (001) facets. Additionally, anatase demonstrates an increased surface adsorption affinity for water molecules, molecular oxygen, and hydroxyl groups, further contributing to its photocatalytic performance.

1.4.2.1.1 Morphologies of TiO_2

Different morphologies of TiO_2 have been reported at nanoscale such as nanoparticles, hollow nano spheres, nanorods/wires, nanotubes and nanoflowers. Under the scope of this thesis, we limit our discussion to following morphologies

i. Nanoparticles: These morphologies exhibit high specific surface area, which is advantageous for surface-mediated processes. Anatase-phase nanoparticles are particularly more efficient in photocatalytic applications due to their superior reactivity and favourable surface chemistry.

ii. Nanorods, nanowires, and nanotubes: These one-dimensional (1D) nanostructures facilitate directed charge transport along the longitudinal axis, effectively minimizing charge recombination. They are commonly fabricated through electrochemical anodization techniques and are widely utilized in photoelectrochemical and sensing devices

1.4.2.1.2 Optoelectronic properties of TiO_2

The electronic structure of TiO_2 has been extensively investigated through both theoretical and experimental approaches. Density of States (DOS) analysis and Density Functional Theory (DFT) calculations provide theoretical predictions, while applied techniques—including UV-Vis spectroscopy, synchrotron radiation-based photoemission spectroscopy and PL offer empirical validation. Across all major polymorphs (anatase, rutile, and brookite), the conduction band (CB) and valence band (VB) edges are predominantly composed of Ti 3d and O 2p orbitals, respectively. This configuration results in TiO_2 having a large bandgap value of ~3.2 eV, depending on the specific phase under consideration. corresponding to first excitonic peak in the UV spectrum.

1.4.2.1.3 Charge carrier dynamics of TiO_2

The photocatalytic efficiency of TiO_2 is governed by factors such as particle size, morphology, crystal phase, surface area, and porosity. In addition, the bandgap (Eg) defines the positions of the conduction

and valence bands and hence determines light absorption and hence the ability to carry out the redox reaction[30]. Upon UV illumination with energy ≥ Eg, TiO_2 generates electron-hole (e^-–h^+) pairs, but <10% contribute to surface redox reactions due to rapid recombination via radiative or non-radiative pathways. Femtosecond spectroscopy reveals that charge carrier trapping in TiO_2 occurs within ~100–200 fs [31], followed by radiative or non-radiative decay on the picosecond to nanosecond timescale. Electrons and holes may localize at Ti^{3+} sites and surface O^{2-} or OH^- groups, though their precise trapping sites remain debated. Smaller particles (<15 nm) enhance surface trapping and prolong charge carrier availability. Anatase TiO_2, with longer electron lifetimes (μs scale) than rutile (tens of ns), shows superior photocatalytic activity, partly due to higher defect-related trapping[32], [33]. Efficient redox reactions require suppressed recombination and may need co-catalyst loading or sacrificial agents to overcome limitations in electron availability for reduction processes.

1.4.2.1.4 TiO_2 as a photocatalyst

The benchmark intrinsic properties an efficient photocatalyst are, such as small E_g, slower charge carrier recombination, band alignment, stability and non-toxic nature. Considering TiO_2 as a photocatalyst, it has the following advantages

a) Suitable band alignment for photocatalytic redox reactions (Hydrogen evolution, Carbon dioxide reduction and degradation of pollutants-Figure 1.12)
b) Chemical and photo stability, durable and non-toxic
c) Abundance in nature

On the other hand, the draw backs are

a) Large E_g value (absorption in UV, mostly below 400 nm)
b) Fast charge carrier recombination

By addressing the draw backs of TiO_2, the photocatalytic activity can be optimized. One of the promising techniques to resolve these limitations is to develop heterostructures, which enable broad absorption range and spatial charge carrier separation.

1.5 Semiconductor nano-heterostructures

Nanoheterostructures (NHSs) are unique materials created by combining two nanoscale segments into one. Their intricate architectures and versatile properties (due to synergistic effect) make them highly promising for applications across electronics, optoelectronics, and catalysis. Such systems allow for precise tuning of charge carriers due to their ability to create new channels for radiative or non-radiative decay. These structures can be prepared by various methods such as solution synthesis [34], [35] (core-shell structures), Ligand assisted reprecipitation, wet impregnation method [36], ball milling [37] or simply through post synthesis electrostatic self-assembly[38] by stirring the two nanostructures together in a suitable media (both nanostructures are synthesized separately).

1.5.1 Applications of nano-heterostructures

Generally, they are designed to enhance the electronic, optical or catalytic properties. The final properties of nano-heterostructures are determined on the basis of band alignment between the two or more components, as well as the structural arrangement, as shown in Figure 1.13. There could be either a

- type-I[39], [40], [41]: both holes and electrons are confined in one of the two nanocrystals. Such systems have high PLQY and are useful in optical applications, as well as for UV to visible down conversion. Since these structures have both the components of the system exposed to the surrounding media, they can also be utilized for photocatalytic activity.

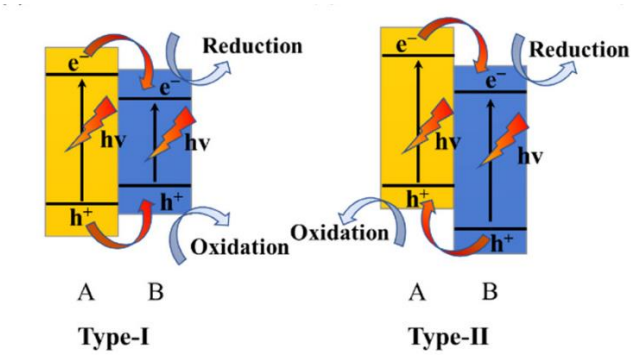

Figure 1.13) Heterostructures based on their band alignment, copied from [29]

- type-II[42], [43], [44], [45], [46]: electrons and holes are confined in separate nanocrystals, paving the way for charge carrier separation and efficient transfer out of heterostructure for photovoltaic or photocatalytic applications.

1.5.2 Charge and energy transfer in nano-heterostructures

As discussed in the previous section, the dynamics of charge carriers can be precisely tuned in nanoheterostructures (NHS) to enhance the functional properties as compared to single component systems. Charge transfer (CT) between the components of nanoheterostructures is the key essential process for driving the desired properties. Photoexcitation of these NHS leads to generation of excitons (electron-hole pairs), these can be separated into individual components for applications in photovoltaic or photocatalytic applications [47]. The separation of excitons in NHS itself, in addition to transfer of individual electron or holes to external quencher constitute charge transfer. The nature of interface in the NHS and type of quencher (molecular acceptor, redox enzyme or semiconductor material) dominate the CT process[48], [49], [50]. Charge transfer studies from quantum dots began in the 1980s with Brus [51], [52] and Kamat [53] showing electron transfer from CdS QDs to small molecules. El-Sayed [54]and Zhang [55] advanced the field using sub-picosecond transient absorption spectroscopy to show charge transfer from quantum dots and Alivisatos reported CT from core-shell QD structures to metallic Pt tips for photocatalytic activity [56]. Recent studies have been focused on interfacial charge transfer in quantum dots based solar cells [57], [58]and photocatalytic reactions [59], [60].

1.5.2.1 Charge transfer/separation dynamics inside the nanocrystals

The existence of electrons and holes in nanocrystals is defined by their respective wavefunctions. As discussed in the earlier sections that band alignment, chemical composition and size determine their spatial localization in core-shell as well as in nano heterostructures. This is the first step to optimize charge transfer in NHS and is termed as 'wavefunction engineering', it is more notable in semi-conductor QD core-shell structures whereby controlling the thickness of shell, the wavefunction of holes and electrons can either be forced to overlap or vice versa. This internal charge separation/transfer can be tailored to optimize the rate of CT to the external quenchers.

1.5.2.2 Charge transfer from nanocrystals to quencher

For non-adiabatic charge transfer process from a nanocrystal to external quencher, the electron transfer rate constant (K_{ET}) can be described by the Marcus theory through the following equation

$$k_{ET} = \frac{2\pi}{h}|E_{DA}|^2 \frac{1}{\sqrt{4\pi\lambda k_B T}} exp\left(\frac{(\lambda + \Delta G_0)^2}{4\lambda k_B T}\right) \quad 1\text{-}9$$

Where,

ΔG_0 is the driving force (free energy difference between the initial and final states)

λ is the reorganization energy of the donor-acceptor system

$|E_{DA}|^2$ is the electronic coupling strength between initial and final states

1.5.2.2.1 Driving force (ΔG_0)

It is the thermodynamic force required to induce CT across the interface of the two components[61]. It is based on the following

1. band offset between the orbitals of donor (E_D) and acceptor (E_A) (potential energy difference). Higher the value, more the driving force. Furthermore, for an efficient CT, the donor should have low oxidation potential (easy to lose electron) and the acceptor should have low reduction potential (easy to gain electron).
2. Charging energy ($E_{C\text{-}E}$), it is due to the transition of components from initial neutral states to charged states after CT.
3. Coulombic interactions in excited states (E_{ex}) and charge separated states (($E_{ex\text{-}sep}$ - after CT). These interactions also depend on the salvation energies of the surrounding media. Nonpolar solvents allow for a stronger coulomb interactions owing to lower salvation energy.

The overall expression for thermodynamic driving force for CT can be written as

$$\mathbf{\Delta G_0} = E_A + E_{C\text{-}E} - E_D + E_{ex\text{-}sep} - E_{ex} \qquad 1\text{-}10$$

1.5.2.2.2 Reorganization energy

It is defined as the energy required to distort one state to the equilibrium geometry of the state and is comprised of two components

- λ_i (internal reorganization energy): it arises from nuclear displacement of Donor-Acceptor systems
- λ_s (solvent reorganization energy): it is the solvent dielectric response and its contribution to the CT process is given by the equation

$$\lambda_0 = \frac{e^2}{4\pi\varepsilon_0}\left(\frac{1}{\varepsilon_{op}} - \frac{1}{\varepsilon_s}\right)\left(\frac{1}{d_D} + \frac{1}{d_A} - \frac{1}{r_{DA}}\right) \qquad 1\text{-}11$$

ε_{op}= solvent high frequency optical constant
ε_s= solvent static dielectric constant
d_D= diameter of spherical donor
d_A= diameter of acceptor
r_{DA}= center to center distance between donor and acceptor

the dependence of reorganization energy on the polarity of solvent and dimensions of the donor-acceptor nanostructures allow for variation in rate of CT. For a nonpolar solvent, the value of dielectric constant leads to negligible contribution to the reorganization energy. As the electron-phonon coupling varies in 0D and 2D NCs, the λ_i also varies, therefore different morphologies of donor NCs and acceptors should show distinct rate of CT.

1.5.2.2.3 Electronic coupling

It is the overlap of the electronic wavefunctions of donor and acceptors. The electronic orbitals of both the components need to overlap for CT to occur.

1.5.2.3 Charge transfer from nanocrystals to Titanium dioxide nanostructures

As discussed previously, Titanium dioxide (TiO_2) is a robust and durable semiconductor material widely investigated for its applications in photovoltaics [62], [63], [64] and photocatalytic activity [65], [66],

[67], [68]. Due to its wide bandgap, its photo absorption range lies in the UV region. The Figure 1.14 shows the solar spectra having maximum intensity per unit area in the visible region

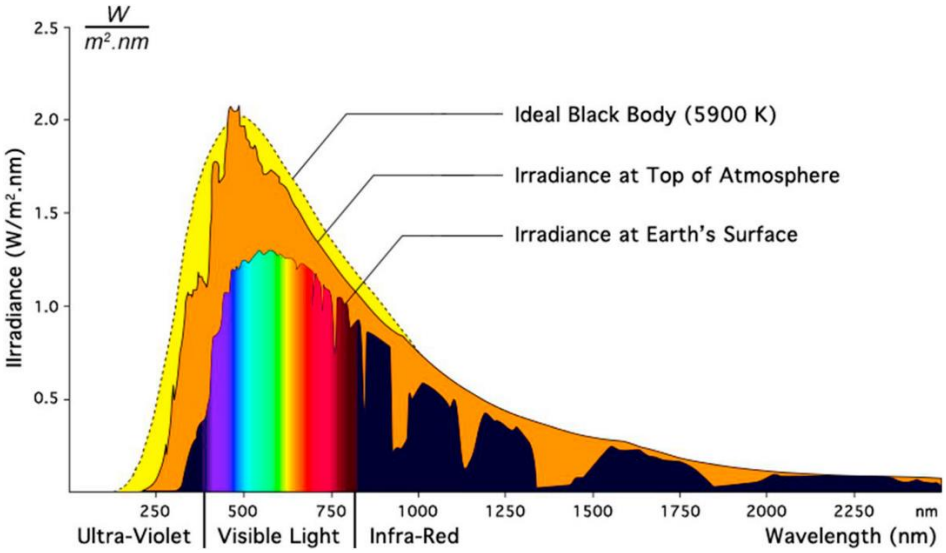

Figure 1.14) Solar spectra plotted, copied from [69]

For the purpose of maximizing the photovoltaic and photocatalytic activity, nano-heterostructures of semiconductor QDs with TiO_2 are developed to shift the absorption from UV to visible region. Kamat et al pioneered the development of QDs-TiO_2 nano-heterostructures and studied the charge carrier [70], [71], [72], [73]. Recently, Hua et al [74]demonstrated use of strongly coupled Cd based II-VI QDs with TiO_2 for photocatalytic visible light degradation of benzene and reported the CdS-TiO_2 as the most efficient nanocomposite system. Subramanian et al [75] bridged the effect of multiexciton generation and hot electron transfer in CdTe QDs decorated TiO_2 nanostructures for photocatalytic activity and demonstrated supervisor photocatalytic activity owing to improved spectral coverage. Li et al [76]studied the effect of size and morphology of CdTe QDs and CdTe QDs sensitized TiO_2 nanostructures on the degrading methyl orange (MO) and methyl blue (MB) in aqueous solution under visible light irradiation. Further similar studies have been conducted by Benavente et al [77], Ma et al [78], An et al [79] and Lv et al [80] to evaluate the photocatalytic performance of TiO_2 decorated with QDs. The effectiveness of TiO_2 decorated with QDs for functional applications is driven by the availability of surplus charge carries from QD sensitizers. The transfer of these charge carriers from QDs to TiO_2 nanostructure crucial for the efficiency of these nano-heterostructures. In this thesis, we focus on studying the effect of surface engineering, doping and wavefunction engineering on the charge carriers dynamics of nano-heterostructures of perovskite and II-VI semiconductors with different morphologies of TiO_2.

1.6 Gap of knowledge

As discussed in the section 1.5.2.3, although considerable developments have been made to enhance and study the effectiveness of charge transfer from QDs to TiO_2 nanostructures, some interesting aspects still remain unexplored . Farrugia et al [81] investigated how different morphologies of TiO_2 nanotube arrays, obtained by altering synthesis parameters, affect their photocatalytic activity. The study found that the diameter of the nanotubes and the thickness of the layer were the primary factors influencing photocatalytic performance. Lee et al. [82] compared the photo response of various TiO_2 morphologies, including nanoparticles and nanotubes, following post-synthesis processing. They found that TiO_2 nanotube arrays exhibited a superior photo response compared to the counterparts. Similar study conducted by Antony M et al [83] depicts the effect of Pt-loaded TiO_2 geometry on the photocatalytic response. It can be deduced that morphology/geometry of the TiO_2 nanostructures have dominant role

in determining electronic structure[84], which subsequently effects the photo response[85]. Hence, the persistent challenges can be summarized, which are, but not limited to, as following:

i. The role of morphology of TiO_2 in accepting excited charge carriers from nanocrystals. TiO_2 nanotubes, nanowires, nanoparticles and compact nanotube arrays can have different tendency to quench charges?
ii. The effect of configuration of working media on the charge transfer from nanocrystals to TiO_2. The nanostructures interaction in liquid phase and thin film phase
iii. Surface engineering of nanocrystals can alter the charge transfer between the nanostructures, but is the magnitude of impact dependent on the working media?
iv. Doping of nanocrystals alters the charge carrier lifetime, how does it behave under the influence of TiO_2 morphologies?
v. Wavefunction engineering of nanocrystals for charge separation and transfer to TiO_2 morphologies.

1.7 Thesis objectives and research scope

Although much research has been focused on analyzing and optimizing the charge transfer between a sensitizer and a photocatalyst, more efforts are needed to fully understand the dynamics. This thesis focuses on the synthesis, and interfacial engineering of nanomaterials for optoelectronic applications. The study encompasses the investigation of various TiO_2 morphologies (nanoparticles, nanotubes, nanorods) acting as quenchers.

It explores hybrid systems incorporating perovskite nanocubes (PNCs), Mn-doped $CsPbBr_3$ perovskites, and core–shell quantum dots (CdTe–CdSe), with an emphasis on tuning surface chemistry, doping effects, and quantum confinement to optimize charge transfer processes. Both colloidal dispersions and thin-film configurations are examined to provide a comprehensive understanding of nanomaterial–TiO_2 interactions.

The scope includes photocatalytic hydrogen evolution measurements, synthesis techniques such as hot-injection and ligand exchange for PNCs, doping strategies for perovskites nanosheets, and wavefunction engineering in core–shell structures. Photophysical characterizations focus on steady-state PL and TRPL, and absorption spectroscopy. The goal is based on establishing material design principles for improving stability, efficiency, and functionality of nanomaterial-based photocatalytic systems.

The structure of this thesis is based on the main objectives of the research work, which are

- To evaluate the influence of TiO_2 morphology (nanoparticles and nanotubes) on photocatalytic hydrogen evolution efficiency (HER). Chapter 2 compares the HER of nanoparticles to that of nanotubes. In addition, the effect of axial dimensions of nanotubes on their HER capability is also investigated.
- To synthesize and engineer the surface chemistry of perovskite nanocubes (PNCs) for optimized charge transfer in hybrid Perovskite/TiO_2 systems in both liquid-phase and thin-film architectures. Chapter 3 highlights $CsPbBr_3$ PNCs as a model system to study the amine ligands-based interactions with TiO_2.
- To examine the effects of doping on charge carrier dynamics and interfacial behaviour with various TiO_2 morphologies, chapter 4 focuses on Mn doped $CsPbBr_3$ perovskite nanosheets and their interactions with different morphologies of TiO_2.
- To employ wavefunction engineering in core–shell quantum dots to extend charge carrier lifetimes and to study charge transfer mechanisms in core–shell/TiO_2 hybrid systems. This is demonstrated in chapter 5 by introducing CdTe–CdSe CSQDs as promising candidates to study these interactions.

2 Hydrogen evolution reaction for TiO_2 nanostructures

Anodically grown nanotube arrays of TiO_2 (TNTAs) have a key advantage over TiO_2 nanoparticles (TNPs) in terms of preparation and handling. While nanoparticles require complicated synthesis techniques, TNTAs can be grown using convenient electrochemistry. In addition, collection of nanopowders after liquid phase HER require centrifugation steps, whereas TNTAs can be simply pulled out of the photocatalytic reactor. Finally, the substrate of TNTAs can be scratched to remove nanotubes and reused after polishing to grow new TNTAs. These advantages make TNTAs interesting candidates for photocatalysis.

The chapter investigates the photocatalytic ability of nanoparticles and nanotubes of TiO_2 to perform HER. TNPs and TNTAs were photo deposited with platinum (Pt) nanoparticles subjected to HER under ultraviolet light (UV). In addition, the optimal height of TNTAs for HER reaction was also determined. All the nanostructures were also characterized for their crystal structure by X-ray diffraction (XRD) and for their morphology by scanning electron microscopy (SEM).

2.1.1 Hydrogen evolution reaction (HER)

The most established method for hydrogen production via photocatalysis is water splitting. This reaction can only be driven by photocatalysts whose conduction B.E lies at a more negative potential than H^+/H_2 reduction potential, and oxidation potential lies at more positive potential than O_2/H_2O oxidation potential, enabling the reduction of protons to hydrogen and oxidation of water, respectively. Water splitting occurs in a photocatalytic cell containing an aqueous electrolyte and two electrodes, an anode and a cathode, immersed in the solution. When an appropriate bias is applied across the electrodes, the cathode facilitates the reduction half-reaction, generating hydrogen gas, while the anode carries out the oxidation half-reaction, producing oxygen. The overall process can be represented by the following equations

Half reaction at cathode	$2H^+ + 2e^- \rightarrow H_2$	2-1
Half reaction at anode	$H_2O \rightarrow \frac{1}{2}O_2 + 2H^+ + 2e^-$	2-2
Overall reaction	$H_2O \rightarrow H_2 + \frac{1}{2}O_2$	2-3

According to thermodynamics, the reaction 2-3 is only feasible if an overpotential around 1.2 eV is applied from an external source at room temperature and ambient atmospheric conditions. The external source is solar energy in the case of photocatalysis.

One of the limiting factors in HER is the formation of H_2O_2, which can compete with HER by enabling recombination of H_2 and O_2, the backward reaction. To overcome this hurdle, photodeposition of noble metals is done. In addition, organic compounds capable of donating electrons are used as hole scavengers which effectively consume the photogenerated holes, leaving behind electrons in the photocatalyst.

2.1.2 Anodic oxidation reaction

Referred to as anodization, it is an electrochemical process in which a metal anode is oxidized for the intention of growing a functional oxide layer (for the purpose of protection or chemical process). Most notably, it has been utilized to develop nanostructured oxide layer of titanium (Titanium dioxide) on a titanium sheet or a magnetron sputtered titanium thin film. This layer of TiO_2 is composed of arrays of closely packed and aligned individual nanotubes, hence the name titanium dioxide nanotube arrays (TNTA)[86], [87], [88].

The process takes place in an aqueous glycerol electrolyte containing a fluoride ion source, a noble metal cathode and the substrate anode (titanium in this case). As appropriate and consistent potential is applied using a potentiostat, the following reaction takes place at anode

Oxidation of Ti metal	$Ti + 2\,H_2O \rightarrow TiO_2 + 4H^+ + 4e^-$	2-4

This continuous oxidation reactions leads to formation of a compact oxide barrier layer. In parallel, the fluoride ions start dissolving the

Fluoride assisted dissolution	$TiO_2 + 6F^- + 4H^+ \rightarrow [TiF_6]^{2-} + 2\,H_2O$	2-5

The dissolution leads to formation of pits/pores, that acts as the primary stage towards the tube formation.

These process proceed simultaneously, and an equilibrium is attained. This leads to formation of long-standing nanotubes. The process parameters can be used to tune the morphology of nanotubes. Briefly, the time of anodic oxidation controls the height of TNTAs, the applied voltage controls the internal diameter of nanotubes, and subsequently the walls thickness as well.

2.1.3 Platinum photodeposition

The existence of Platinum (Pt) nanoparticles on the surface of a photocatalyst enhances the overall photocatalytic activity by acting as a reservoir for photogenerated electrons. This reduces carrier recombination, and hence increased number of photoexcited charge carriers are at disposal for reduction reaction. In addition, specifically for hydrogen evolution process, presence of Pt prohibits the backward reaction initiated by formation of H_2O_2.

To deposit Pt nanoparticles onto the surface of TiO_2, an aqueous solution of Pt source (conventionally chloroplatinic acid - H_2PtCl_6) and TiO_2 nanostructure is exposed to UV light irradiance. This causes the excitation of electrons into the conduction band of TiO_2. These electrons are captured by the Pt^{+4} adsorbed on the surface of TiO_2 and it reduces to metallic Pt^0, according to following reaction [89]

Pt reduction	$H_2PtCL_6 + 2\,H_2O \rightarrow Pt^0 + 6H^+ + 6Cl^- + O_2$	2-6

Hole scavengers are also used to prevent the recombination of excited electrons with holes, therefore directing the electrons to the Pt. The size of Pt nanoparticles may vary depending on the crystal structure (anatase or rutile).

2.1.4 Objectives

- Photocatalytic HER evolution based on morphology of TiO_2 nanostructures
- HER capability based on height of TNTAs

2.2 Experimental

2.2.1 Materials used

All the materials were ordered from Sigma Aldrich and used without any further purification, which Ammonium fluoride (NH_4F), Ethylene glycol ($C_2H_6O_2$), Chloroplatinic acid (H_2PtCl_6), Titania nanoparticles Anatase (99.7% , <25 nm) and Ti sheets.

2.2.2 Growth of Titania nanotube arrays

The growth of TNTAs can be referred to as an anodic oxidation process. It involves applying electric potential to a Ti substrate in the presence of an electrolyte, as reported by Waseem et al [90] . The details of the process are given below

2.2.2.1 Preparation of electrolyte

200 mL of ethylene glycol was mixed with 1.1 g of Ammonium fluoride and 6.67 g of water was added to this mixture to prepare a 3 wt% water solution. The mixture was stirred at room temperature for 2 hours.

2.2.2.2 Preparation of Ti substrate

The Ti substrates (I.5 cm x 1.5 cm) were polished to obtain a smooth surface, followed by ultrasonication in acetone and ethanol to for 5 minutes to ensure complete removal of impurities. Finally, the cleaned substrate was rinsed with ultrapure distilled water and dried with Nitrogen.

2.2.2.3 Growth of titania nanotubes arrays and annealing

The electrolyte was poured into a container and Ti substrates was dipped into it. A circular Platinum (Pt) electrode with 0.45 cm radius was immersed in the electrolyte parallel to the Ti substrate (typically 1.5 cm x 1.5 cm) at a distance of 6 cm, was used as a counter electrode. A 60 V potential difference was applied for three-time ranges (15, 18 and 21 minutes). The time of process determines the final height of the nanotubes. Finally, the obtained tubes were submerged in ethanol for 1 hour, cleaned with distilled water, and dried with Nitrogen. The sample was annealed at 450°C for 1 hour in air atmosphere to obtain anatase phase. The Figure 2.1 shown schematic of the process of nanotubes growth

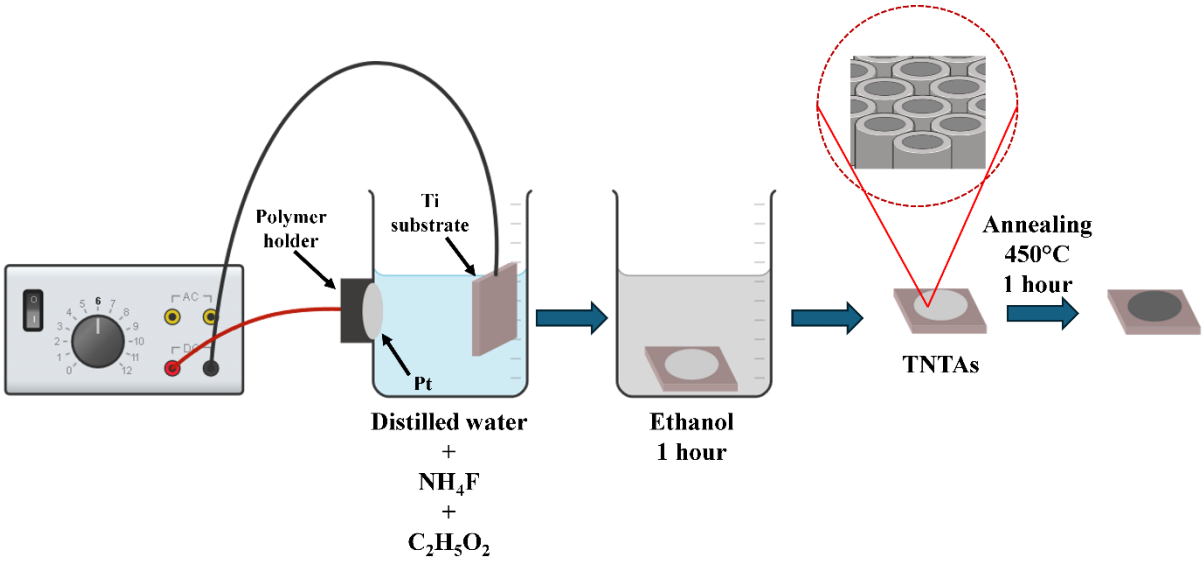

Figure 2.1) Schematic showing TNTAs growth process through anodic oxidation and subsequent treatment

The as prepared TNTAs were annealed at 450°C for 1 hour in air atmosphere to obtain anatase phase.

2.2.3 Platinum photodeposition

2.2.3.1 On TNTA

Titania nanotubes substrates were immersed in 0.075 mM H_2PtCl_6 10mL mix of distilled water and methanol (50Vol%:50Vol%). This was followed by exposure to 365 nm UV lamp for 1 hour under constant argon bubbling to achieve 0.5wt% Pt loading. Afterwards, the substrate was rinsed with distilled water and dried using nitrogen gas.

2.2.3.2 On Titania nanoparticles

Titania nanoparticles (60 mg) were suspended 0.075 mM H_2PtCl_6 30mL mix of distilled water and methanol (50Vol%:50Vol%). followed by exposure to 365 nm UV lamp for 1 hour under constant stirring at 600 rpm and argon bubbling to achieve 0.5 wt% Pt loading. The grey coloured nanoparticles were centrifuged out at 3600 rpm and dried in oven at 40°C for 24 hours.

2.2.4 Characterization

2.2.4.1 XRD

XRD for TNTAs and powder samples was measured using an Aeris X-ray diffractometer from Malvern Panalytical (Cu Kα1, 1.5406 Å). The TNPs sample was prepared by drop-casting the colloidal suspension on a low-background silicon disc.

2.2.4.2 SEM

SEM images of anodically grown TNTAs and nanoparticles were recorded on a Gemini Supra 25 field-emission SEM from Zeiss at an acceleration voltage of 10 kV.

2.2.4.3 Photocatalytic activity

The photocatalytic hydrogen (H_2) evolution performance of both Pt-TiO_2 samples was assessed in aqueous solutions containing 50 vol% methanol. 2 mg Anatase powders and 8µL heigh TNTAs (corresponding to 2 mg in weight) were tested. For each experiment, a quartz tube reactor was filled with the reaction solution, and a sample was submerged in it. The system was purged with argon gas for 15 minutes to remove dissolved oxygen, then sealed tightly. The sample was then continuously illuminated using a UV-LED light source (λ_{max} = 365 nm) at a calibrated irradiance of 65 $mWcm^{-2}$. Hydrogen gas generation was monitored after each hour of illumination using gas chromatography (GCMS-QP2010 SE, Shimadzu, Japan) with a thermal conductivity detector (TCD).

2.2.4.3.1 Calculations to determine rate of hydrogen evolution

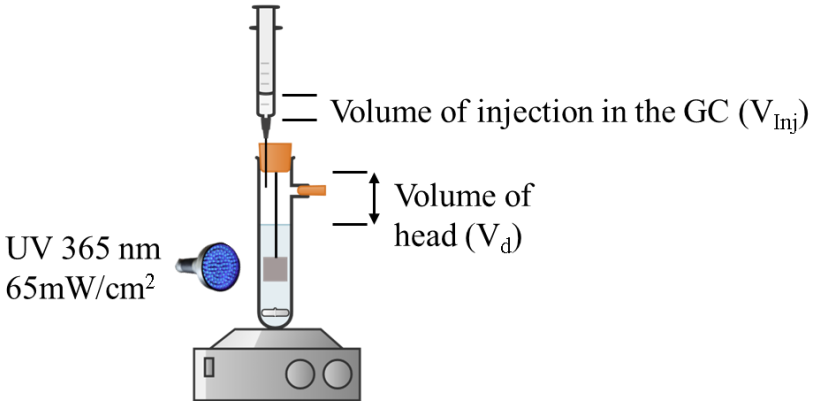

After each hour, a specific volume (V_{Inj}= 200 µL) was analysed using the CGMS, and corresponding concentration of H_2 was obtained (%H_2). The volume of generated H_2 was calculated using the following equations

$$V_{H2}\ \text{generated}\ (\mu L) = \frac{\%H_2}{100} \times V_d(mL) \times 1000 \quad (2\text{-}7)$$

$$H_2\ \text{production rate}\ (\mu L\ h^{-1}\ g^{-1}) = \frac{V_{H2}}{\text{hours} \times (\text{weight of photocatalyst in grams})} \quad (2\text{-}8)$$

2.3 Results and discussion

2.3.1 XRD analysis

The X-ray diffraction (XRD) pattern of the TNTAs exhibits characteristic peaks corresponding to the anatase phase of TiO_2, as illustrated in Figure 2.2. Prominent diffraction signals are identified at 2θ values of 25.3°, 38.3°, and 48°, which correspond to the (101), (004), and (200) crystallographic planes, respectively, as per JCPDS card No. 21-1272. Notably, the peak at 38.1° can be attributed to both the (004) plane of anatase and the underlying titanium substrate, due to their overlapping diffraction signals.

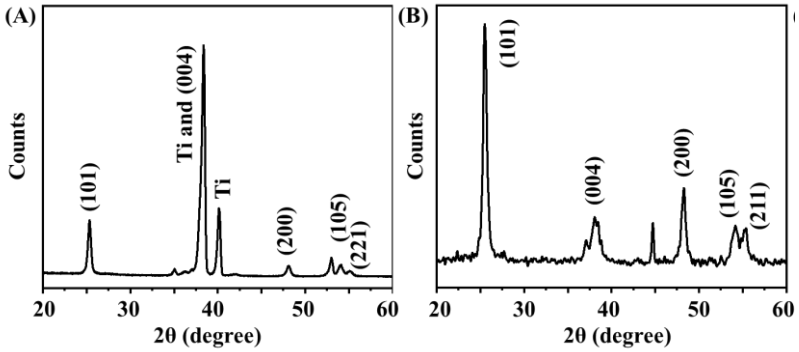

Figure 2.2) XRD patterns of TiO_2 (A) TNTAs and (B) TNPs-Anatase

In the case of TNPs, the anatase phase reveals diffraction peaks corresponding to the (101), (004), (200), (105), and (211) planes, observed at 2θ values of 25.1°, 38.3°, 48°, 48°, 54.1°, and 55.4°, respectively. The peak at 44° which is not indexed, corresponds to (210) plane of rutile phase.

2.3.2 SEM analysis

2.3.2.1 Bare TNTAs

The SEM images of the as grown TNTAs are shown in the Figure 2.3 The as-grown TNTAs exhibit an average height of approximately 8.1 µm. The inner and outer diameters of the individual nanotubes are estimated to be around 110 nm and 130, respectively nm, respectively. Due to the direct growth of TNTAs on a titanium substrate, conventional cross-sectional imaging techniques are not feasible. To overcome this limitation, a simple mechanical detachment approach is employed: the surface is gently scratched using a finely sharpened blade.

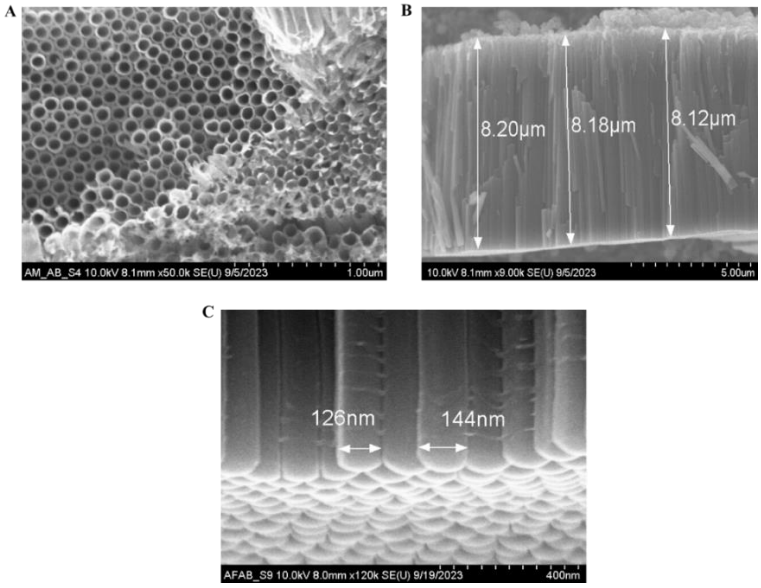

Figure 2.3) SEM images of TNTAs A) Top view, B) Side view and C) Side and bottom view

This process facilitates the partial removal of the nanotube layer from the substrate, enabling accurate height measurements via SEM.

2.3.2.2 Pt photo deposited on TiO_2

All the samples of titania were loaded with Pt nanoparticles, and confirm by SEM analysis, as shown in the Figure 2.4

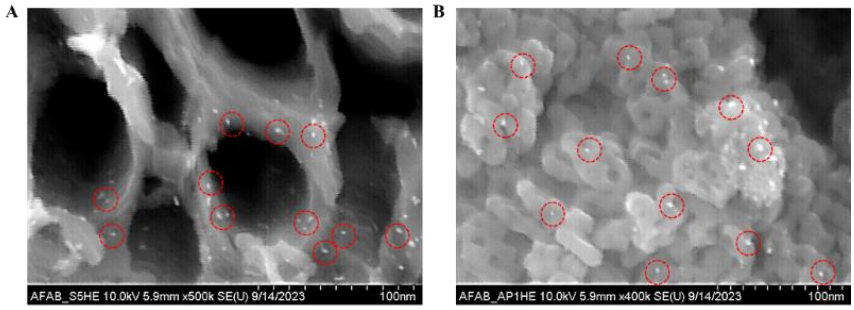

Figure 2.4) SEM images after Pt photodeposition on A) TNTA, and B) TNPs-Anatase. The red dotted circles show Pt nanoparticles

Since the amount of precursor and all the deposition parameters were kept constant for both the samples, the EDS spectra show 0.52 wt% presence of Pt on the samples. In any case, the chemisorption of Pt onto the TiO_2 morphologies helps to prevent the backward reaction initiated by H_2O_2 [91].

2.3.3 Hydrogen evolution reaction (HER)

2.3.3.1 Influence of phase and morphology

Upon successful deposition of Pt nanoparticles on the TiO_2 nanostructures, the samples were evaluated for their photocatalytic performance. Since the photocatalytic efficiency is largely influenced by the amount of material exposed to the reaction environment, TiO_2 nanoparticles are a well-established morphology for this application. This is attributed to the high surface area of TiO_2. The 2 mg anatase powders and 8.1 µm long anatase nanotubes (corresponding to 2 mg) were evaluated for their water splitting capability to generate hydrogen in the presence of methanol acting as a hole scavenger. The results of the hydrogen evolution reaction (HER) are presented in Figure 2.5

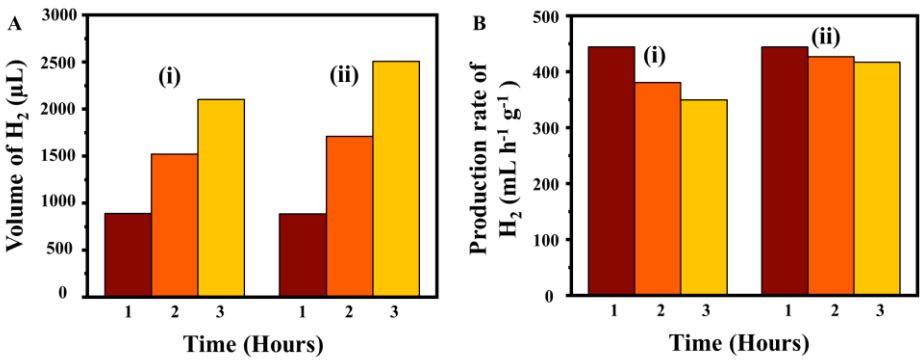

Figure 2.5) (A) Photocatalytic hydrogen evolution capability of (i) TNPs-Anatase (ii) TNTAs and (B) their corresponding hydrogen production rates. Two measurements were recorded per each point and the maximum deviation obtained is 20µL

Anatase phase nanoparticles are known for better HER capability as compared to rutile phase, possibly due to longer lifetime of charge carriers in the range of µs [30] and bulk transport of excitons to the surface [92]. Zhang et al [93] analysed the band structure, density of states and effective mass of photoexcited charge carriers in anatase and rutile phase of TiO_2 using first principle density functional theory and attributed relatively higher photocatalytic activity of anatase to its indirect bandgap, which causes longer lifetime for excited carriers. In addition, it was also reported that the anatase had the lightest average effective mass for electrons and holes, hence faster mobility to the surface and reduced recombination in the bulk state. Similar conclusions were reported by Žerjav et al [94], where indirect bandgap of anatase was cited as the main reason for its higher photocatalytic activity, and deep electron traps in rutile were reported to be limiting factor.

The Figure 2.5A shows TNTAs with 8.1 µm height outperform the anatase phase nanoparticles. The efficient photocatalytic activity of TNTAs as compared to nanoparticles could be attributed to the ligand free growth, well-developed contact area with the reactants to efficient diffusion into the nanotubular structure, efficient absorption of light and charge separation [95], [96] and fast-long uni-directional electron transport due to 1D structure [97], [98], [99], lack of aggregation and better geometry that supports light absorption. In addition, as evident from Figure 2.5B, TNTAs have the capability to maintain rate of production with the passage of time, as compared to the TNPs.

To understand the effect of height of TNTAs on the hydrogen evolution, different heights of nanotubes were tested.

2.3.3.2 Influence of height of TNTAs

Three TNTA samples designated as S1, S2 and S3 were prepared to analyse the effect of height of nanotubes on the relative HER capability. The growth parameters are shown in Table 2.1

Table 2.1) Parameters adopted for TNTAs growth during anodic oxidation

Sample	Electrolyte	Applied voltage	Time of growth	Height of TNTAs
S1	3wt% Aqueous electrolyte – 0.15 moles NH_4F – Ethylene glycol	60 V	15 min	5.7 ± 0.021 µm
S2			18 min	8.1 ± 0.041 µm
S3			21 min	10.5 ± 0.18 µm

The figure below shows the SEM analysis of TNTAs grown for different time periods having distinct difference in size. The SEM images of all the three samples are shown in the Figure 2.6

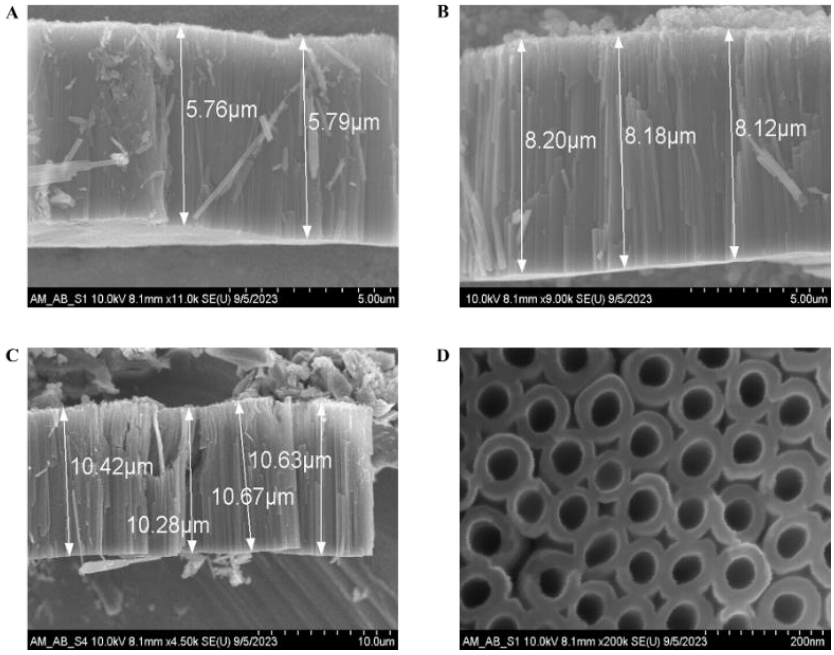

Figure 2.6) SEM images of TNTAs grown for different time periods

As the time of growth increases, the height of the nanotubes also increases. The HER results for corresponding samples are shown in the Figure 2.7

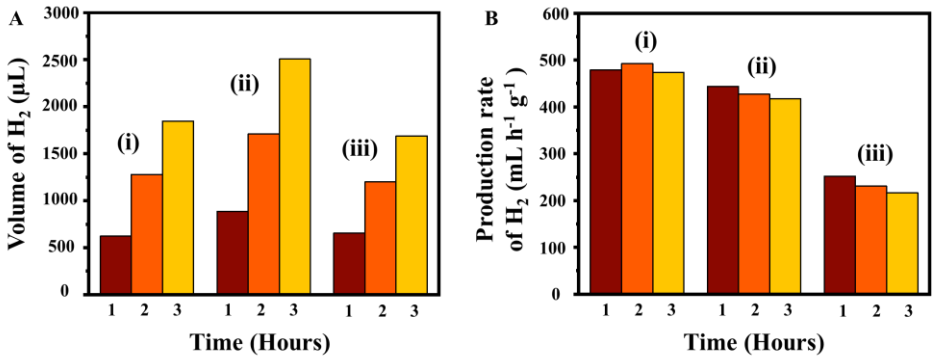

Figure 2.7) (A) Photocatalytic hydrogen evolution using TNTAs having different heights (i) 5.7 µm, (ii) 8.1 µm, (iii) 10.5 µm. and (B) their corresponding hydrogen production rates. Two measurements were recorded per each point and the maximum deviation obtained is 23 µL

The TNTAs with 8.1 µm height show the optimal activity, however 5.7 µm nanotube show better production rate, possibly due to the effect of enhanced light harvesting capability. Liu et al [100], reported the dependence of photocatalytic on the height of nanotubes and demonstrated that short

nanotubes perform better under 3.1 $mWcm^{-2}$. In any case, the overall analysis suggests that the TNTAs have ability to perform better in terms of hydrogen evolution, as compared to well established nanoparticles. In addition, the TNTAs can conveniently be removed from the reaction media without additional centrifugation step. Furthermore, the TNTAs are reuseable, and even can be scratched and polished to obtain a smooth Ti substrate, that can be utilized to grown regrow TNTAs.

2.4 Summary

The influence of TiO_2 morphology on the HER capability was studied. At first, anatase phase nanoparticles and 8.1 µm high TNTAs were subjected to HER and the results were compared to decide the effectiveness of morphology. In the second step , TNTAs having average height value of 5.7 µm, 8.1 µm and 10.5 µm were grown and subjected to HER. The final results show that

- Anatase phase TNTAs have relatively better HER capability as compared to TNPs.
- 8.1 µm is the ideal height of nanotubes for the best photocatalytic activity.

Having established these outcomes and based on discussion in the section 1.4, it can be concluded that morphology play a crucial role in determining the electronic structure and charge carrier dynamics. In light of discussion in section 1.5, we select the phase and structures with best HER performance and try to analyse electron transfer from external sensitizers to these nanostructures of TiO_2.

3 Tailoring Charge Donor–Acceptor Interaction in $CsPbBr_3$ Perovskite Nanocrystals through Ligand Exchange

In this chapter, we introduce Nanocrystals (NCs) of lead halide perovskite, specifically Cesium Lead Bromide ($CsPbBr_3$), as promising candidates for the role of sensitizers for different morphologies of TiO_2. This is because $CsPbBr_3$ PNCs absorb in the visible range (where solar spectra is maximum), are more stable as compared to $CsPbI_3$ and provide better control over synthesis and size tuning, as compared to $CsPbCl_3$. In addition, they also allow for a simple and swift post synthesis ligand exchange process compared to other semiconductor materials. The concept of surface engineering was utilized to tailor the charge transfer from perovskite nanocubes (PNCs) to TNPs and TNTAs in liquid phase and thin film phase. The aim was to study the ligand-based interactions between PNCs and TiO_2 morphologies, to access the most suitable configuration for electron transfer. Furthermore, we demonstrate a convenient and effective post synthesis ligand exchange process that yields stable PNCs functionalized with shorter ligands compared to the original ones.

3.1 Perovskites (ABX_3)

Three-dimensional (3D) ABX_3 perovskites are outstanding semiconductors due to their superior optoelectronic properties and broad applications, such as photovoltaics, LEDs, photodetectors, lasers, and photocatalysis [101]. In this structure, A represents a monovalent cation like Cs^+, methylammonium (MA), or formamidinium (FA), which resides in a cavity formed by corner-sharing $(BX_6)^{4-}$ octahedra composed of a divalent metal ion B^{2+} (B = Pb, Sn, Ge) and halide ions X^- (X = Cl, Br, I). Among the different formulations of metal halide perovskites, all-inorganic perovskite nanocrystals (PNCs) have attracted attention due to their remarkable stability, near-unity PLQY, and compatibility with optoelectronic devices [102]. Tuning the surface of these PNCs via ligand engineering is essential to enhance their performance and expand their utility. Figure 3.1 shows the crystal structure and PL emission under UV light for $CsPbX_3$ (X=Br, I)

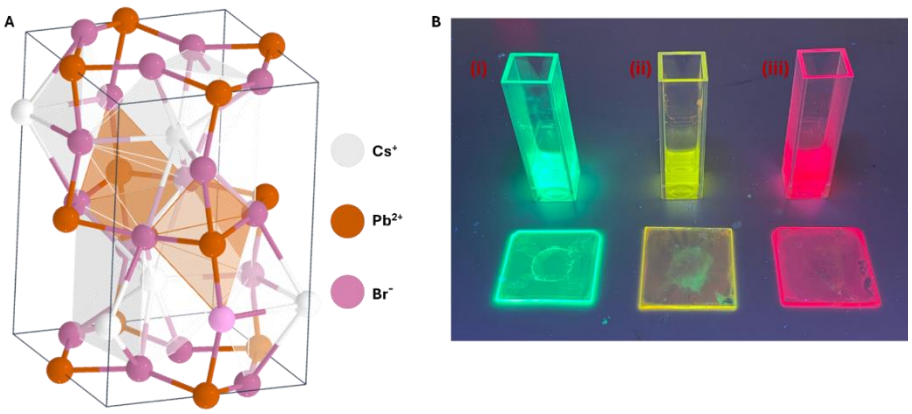

Figure 3.1) (A) The unit cell for $CsPbBr_3$ perovskites, B) PNCs of $CsPbX_3$ (i) X=Br, (ii) X=I (PNC size < 7 nm) and (iii) X=I (PNC size > 8 nm)

3.1.1 Role of surface ligands in ABX_3

Surface ligands serve a vital role in controlling not only the morphology and the dimensions of ABX_3 PNCs [103] but also their optoelectronic behaviour, durability, and surface characteristics [102], [104]. Surface passivation of PNCs through ligands mitigates intrinsic defects and blocks external molecules

like water and oxygen from interacting with their surfaces. This, on one hand, reduces nonradiative decay routes for excitons, thereby enhancing PL QY and charge carrier performance, and on the other hand, boosts both intrinsic and environmental robustness. While oleic acid and oleylamine represent the standard Lewis acid–Lewis base ligand pair employed to produce morphology-controlled, stable, and highly luminescent PNCs and quantum dots (QDs) [105], other ligands including phosphine/phosphine oxide,[106], [107] sulfonate, [108] quarternary ammonium,[109] and zwitterionic or bidentate ligands [110], [111] are also applied, either alongside the conventional ones or separately, to obtain high-performance nanocrystals. In every instance, the influence of surface ligands in maintaining and enhancing ABX_3 PNC properties remains essential.

In addition to controlling shape and size, enabling defect passivation, and enhancing stability, surface ligands play a crucial role in mediating the photophysical interactions of PNCs with each other and with other semiconductors, metals, or molecular systems, potentially facilitating charge or energy transfer processes [112], [113], [114], [115], [116], [117], [118], [119], [120]. Bulky surface ligands can serve as insulating barriers that hinder charge transfer between PNCs and adjacent charge-donating or -accepting species. This significantly impacts the performance of devices employing ABX_3 PNCs as photoactive layers, whether for light absorption or emission[104], [121], [122]. Furthermore, such ligands can restrict the application of PNCs in photocatalytic systems, where efficient exciton dissociation and charge separation are essential for driving heterogeneous photoredox reactions [118]. Conversely, partial or complete removal of surface ligands can enhance charge transfer kinetics but often comes at the cost of reduced colloidal stability and compromised optoelectronic properties[123], [124], [125]. Therefore, an optimized ligand environment is critical to achieving efficient charge transfer while maintaining the structural integrity and functional performance of PNCs.

The incorporation of aromatic or π-conjugated ligands during the synthesis of metal halide perovskites has been shown to facilitate charge delocalization across the ligand–nanocrystal interface [112], [115], [116], [119], [120], [126]. Vickers et al. reported that $MAPbBr_3$ quantum dot (QD) films synthesized with benzylamine and benzoic acid ligands exhibited significantly enhanced electrical conductivity, prolonged carrier lifetimes, and more efficient charge transfer to fluorine-doped tin oxide (FTO) substrates compared to QDs capped with insulating ligands [112]. Furthermore, the use of short-chain ligands during the surface passivation of ABX_3 PNCs has been found to improve electronic coupling either between adjacent PNCs or with external charge donor/acceptor species, thereby facilitating more efficient charge transfer processes [114], [115], [123]. In this context, Kumar et al. demonstrated that reducing the alkyl chain length of aliphatic amine ligands from sixteen to six carbon atoms in $FA_{0.5}MA_{0.5}PbBr_3$-based light-emitting diodes (LEDs) led to increased current density and luminance, along with a reduced turn-on voltage [114]. These enhancements were attributed to improved charge transport between nanocrystals, resulting in more efficient charge injection into the emissive PNC layer of the device.

Controlling the morphology of three-dimensional (3D) ABX_3 PNCs through the use of conjugated/aromatic or short-chain ligands during synthesis presents a significant challenge. Short-chain ligands, for instance, can promote the formation of quasi-two-dimensional (2D) perovskite nanosheets or a heterogeneous mixture of nanosheets and nanocubes[127], [128], [129]. Similarly, the incorporation of conjugated, aromatic, or short-chain ligands may favour the formation of layered 2D Ruddlesden–Popper phases over the targeted 3D perovskite nanocubes morphology [130]. While these low-dimensional metal halide structures offer promising optoelectronic properties, their characteristics differ markedly from those of 3D ABX_3 PNCs [131], [132]. This morphological and structural variability complicates direct comparisons of charge transfer behaviours between systems capped with long-chain versus short-chain ligands, as well as among various metal halide nanostructures. Such comparative studies are vital for advancing the fundamental understanding of photophysical processes in donor–acceptor systems based on 3D ABX_3 PNCs and for optimizing their implementation in light-emitting and photovoltaic devices. Alternatively, post-synthetic ligand exchange provides a promising route to engineer the PNC surface for improved charge transfer, while retaining the desired 3D morphology and preserving key optoelectronic properties [104], [133].

Previous studies have shown various ligand binding modes on the surface of ABX_3 PNCs, indicating that organic acid and amine ligands are only weakly coordinated and exhibit highly dynamic, reversible interactions with the PNC surface [104], [134], [135], [136]. This dynamic nature enables facile post-

synthetic ligand exchange; wherein native surface ligands can be readily substituted with tailored alternatives to modify surface properties. Such ligand tuning, particularly in terms of chain length and conjugation, can significantly enhance interfacial charge transfer between PNCs and adjacent semiconductors or molecular acceptors/donors [115], [117], [137]. For instance, Biswas et al. demonstrated the successful replacement of oleic acid ligands on $CsPbBr_3$ PNCs with short-chain benzoic acid and ascorbic acid via post-synthesis exchange [115]. Both ligand-exchanged systems exhibited improved colloidal stability and optoelectronic performance; however, the benzoic acid-capped PNCs facilitated superior charge transfer rates to electron acceptors such as para-benzoquinone and hole acceptors like phenothiazine, owing to the conjugated and compact nature of the ligand. Similarly, Dey et al. reported enhanced electronic coupling and charge transfer efficiency across $CsPbBr_3$ PNC–CdSe nanoplatelet heterojunctions when cross-linked post-synthetically with para-aminobenzoic acid or glycine ligands, in contrast to systems retaining native long-chain oleic acid and oleylamine ligands[137].

3.1.2 Objectives of this study

In this study, we demonstrate improved interfacial interaction and charge transfer between $CsPbBr_3$ PNCs functioning as electron donors and TiO_2 nanostructures serving as electron acceptors, facilitated through post-synthetic ligand exchange wherein the long-chain oleylamine was replaced with a shorter-chain butylamine ligand. TiO_2 was selected as the electron acceptor due to its favourable type-II band alignment with metal halide perovskites, which supports efficient electron extraction [138]. Moreover, TiO_2 is a widely investigated material known for its thermal and chemical stability, cost-effectiveness, and suitable conduction band positioning, making it a prominent electron transport layer in perovskite solar cells [139], [140] and an effective photocatalyst for applications such as chemical transformations and water splitting [141], [142], [143]. We explore aspects such as

i. PL quenching based on PNC surface ligand
ii. Electron-transfer dynamics of PNCs/TiO_2 systems
iii. Trap-state modifications resulting from the donor-acceptor interaction.

This study provides critical insights into fine-tuning the $CsPbBr_3$ PNC–TiO_2 donor–acceptor interactions via post-synthetic ligand exchange. Continued investigation of this strategy offers significant potential for the rational design of metal halide perovskite-based heterojunctions with optimized charge transfer characteristics.

3.2 Experimental

3.2.1 Materials used

All the materials were ordered from Sigma Aldrich and used without any further purification, which include Lead (II) bromide ($PbBr_2$, 98+%), Cesium Acetate ($C_2H_3CSO_2$, >98%), Oleic acid (OA, 90%), Oleylamine (OAm, 80-90%), Butylamine (BAm, 99+%) Octadecene (ODE, 90%) and Toluene (99.5%). Titanium dioxide nanoparticles were ordered from Kemira Global, Finland.

3.2.2 Synthesis of Cesium Lead Bromide ($CsPbBr_3$) Nanocubes

The synthesis of $CsPbBr_3$ PNCs using OA and OAm as the main ligands was achieved using a modified hot injection technique, as reported by Kunnathodi et al [144].

3.2.2.1 Cesium Precursor

To start, 77 mg of $CsC_2H_3O_2$ (0.4 mmoles), 500 µL OA (1.58 mmoles) and 1 mL ODE were heated to 120◦C under argon, followed by drying at 120◦C under vacuum for 1 hour until the mixture turned transparent, indicating complete mixing of precursors.

3.2.2.2 Lead Bromide Precursor

146 mg of $PbBr_2$ (0.4 mmoles), 1.262 mL OA (4 mmoles), 1.316 mL OAm (4 mmoles) and 25 mL ODE were also heated to 120◦C in a separate three neck flask under argon and kept for drying under vacuum for 1 hour at 120◦C. The degasification process for both precursor solutions was done to remove oxygen and moisture.

3.2.2.3 Hot injection of precursors

After 1 hour of degasification, the precursors were switched back to argon atmosphere and the temperature of $PbBr_2$ precursor was increased to 155◦C and injected with 1 mL of Cs precursor; after 2 seconds of reaction time, the mixture was quenched to room temperature using an ice bath, followed by centrifuging at 10,000 rpm for 10 minutes to collect the precipitate. The collected precipitate was suspended in toluene and centrifuged again at 6000 rpm for 10 minutes to collect the precipitate which was suspended in 6 mL of toluene for further use.

3.2.3 Ligand exchange to Butylamine

The ligand exchange process was employed to exchange the OAm ligand with BAm. 6 µmoles of as synthesized $CsPbBr_3$ PNCs (50uL) and 20 µmoles of BAm (2µL) were added in 500 µL toluene and stirred at 500 rpm for 10 minutes, followed by washing of excess ligands at 5000 rpm for 5 minutes. The obtained precipitate was suspended in toluene. The volume of BAm was optimized for use, as higher concentration led to rapid degradation into a colourless suspension (Cs_4PbBr_6) within few tens of minutes, whereas lower concentrations led to incomplete ligand exchange.

3.2.4 Preparation of Titanium dioxide (TiO_2) nanoparticles suspension

1 g of TiO_2 nanopowder (nanoparticles) were initially suspended in 4 mL Toluene and sonicated for 9 hours at 100 Hz frequency. The suspension was diluted by adding 10 mL of toluene and sonicated for 3 hours to ensure fine colloidal suspension.

3.2.5 Growth of Titanium dioxide nanotube arrays

TiO_2 NT arrays were produced by anodic oxidation of commercial purity, Grade 2 ASTM, titanium sheets that were 0.5 mm thick. From the sheets, 1.5 x 1.5cm^2 size slabs were cut and polished with P600 Silicon carbide paper. The TiO_2 slabs were then subjected to sonication in ethanol to remove surface contaminations and anodized in an ethylene glycol solution containing 0.2 M of NH4F and 2M of distilled water. A cell voltage of 45V was reached by a linear sweep in 2min and maintained for 30min in the potentiostatic conditions, as reported in previous studies. At the end of the anodizing procedure, TiO_2 slabs were carefully rinsed with distilled water and subjected to annealing at 500°C for 2h to obtain oxide crystallization in the anatase phase.

3.2.6 Preparation of $CsPbBr_3/TiO_2$ nanocomposite

3.2.6.1 $CsPbBr_3/TiO_2$ thin films

Thin films of OAm capped $CsPbBr_3$ (without and with TNPs) and BAm capped $CsPbBr_3$ (without and with TNPs) were spin coated onto 18x15 mm Menzel-Glaser glass substrates (cover slips) at 1000 rpm for 2 seconds. Prior to deposition, the glass substrates were ultrasonically treated in isopropanol and acetone respectively, followed by drying using argon gun. To avoid and minimize the effect of aging and degradation, freshly synthesized PNCs were used, and all the readings were taken by using fresh samples immediately after the ligand exchange to ensure comparability.

Similarly, colloidal suspension of BAm capped $CsPbBr_3$ was also spin coated over the TNTAs at 1000 rpm for 2 s, followed by drying under argon atmosphere.

3.2.6.2 $CsPbBr_3$-$CsPbBr_3/TiO_2$ junction

Thin films of BAm capped $CsPbBr_3$ (without and with TNPs) were produced on a single piece of glass slide 15x54 mm substrates. The $CsPbBr_3$ (without and with TNPs) were drop casted on the two marked areas of glass slide, to ensure the formation of clearly distinct junction between them.

3.2.7 Characterization techniques

3.2.7.1 X-ray Diffraction

Powder XRD of the samples was measured using an Aeris X-ray diffractometer from Malvern Panalytical (Cu Kα1, 1.5406 Å). The samples were prepared by drop-casting the PNC colloidal solution on a low-background silicon disc.

3.2.7.2 Transmission Electron Microscopy (TEM), Scanning Tunnelling Electron Microscopy (STEM) and Scanning Electron Microscopy

STEM images of CsPbBr3 PNCs were acquired on a Jeol ARM20CF NeoARMelectron microscope at 200kV acceleration voltage. The samples were prepared by drop-casting the colloidal solution on the carbon-coated TEM grids. SEM images of anodically grown TiO_2 NTs with $CsPbBr_3$ PNC deposition were recorded on a Gemini Supra 25 field-emission SEM from Zeiss at an acceleration voltage of 10 kV. Similarly, the SEM images of bare anodically grown TiO_2 NTs were recorded on a Gemini SEM 300 FEG from Zeiss at an acceleration voltage of 5 kV.

3.2.7.3 UV-Visible absorption, Steady state and time resolved photoluminescence and Photoluminescence Quantum Yield

UV–vis absorption spectra of $CsPbBr_3$ PNCs and TiO_2 NPs were recorded in a quartz cuvette using a Lambda 1050+UV–vis–NIR spectrometer from Perkin Elmer. Steady-state and time-resolved PL were recorded on Spectrofluorometer FS5 from Edinburg Instrument. For the time-resolved PL measurements, a picosecond laser with 375nm excitation wavelength was used and the data acquisition was made using the technique of TCSPC. The decay profiles were tail fitted with a triexponential decay function

$$R(t)=A_1 \exp\left(-t/\tau_1\right)+A_2 \exp\left(-t/\tau_2\right)+A_3 \exp\left(-t/\tau_3\right) \quad 3\text{-}1$$

and the intensity-weighted average PL lifetime was calculated using the equation

$$\tau_{av}=\frac{A_1\tau_1^2+A_2\tau_2^2+A_3\tau_3^2}{A_1\tau_1+A_2\tau_2+A_3\tau_3}. \quad 3\text{-}2$$

Also, the fractional contribution of each decay time to the steady-state intensity was calculated using the formula

$$f_i=\frac{A_i\tau_i}{A_1\tau_1+A_2\tau_2+A_3\tau_3} \quad 3\text{-}3$$

PLQYs of the $CsPbBr_3$ PNCs were measured using an absolute method by directly exciting the PNC solution as the sample and the toluene as the reference in an SC-30 integrating sphere module fitted to a Spectrofluorometer FS5 from Edinburg Instrument. During the measurement, the excitation slit was set to 3nm, and the emission slit was adjusted to obtain a signal level of 1 106cps. A wavelength step size of 0.1nm and an integration time of 0.2s were used.

The electron transfer rate constants for thin films were calculated based on the formula

$$K_{ET} = \frac{1}{\tau_{(PNC.TiO2)}} - \frac{1}{\tau_{(PNC)}} \quad 3\text{-}4$$

Where K_{ET} is the rate transfer constant, τ_{PNC} and $\tau_{PNC.TiO_2}$ are the PL lifetime for sample deposited by spin coating on glass slides without and with TiO_2.

The calculation of absolute PL QY for liquid and thin film samples is based on the formula,

$$\text{PL QY} = \frac{E_{sample} - E_{ref.}}{S_{ref.} - S_{sample}} \quad 3\text{-}5$$

where E_{sample} and E_{ref} are the integrals at the emission region for the sample and the reference, respectively, and S_{sample} and S_{ref} are the integrals at the excitation scatter region for the sample and the reference, respectively. The selection and calculation of integrals from the emission and excitation scattering region and the calculation of absolute PL QY were performed using the FLUORACLE software from the Edinburg Instrument. For steady-state PL spectra and absolute PL QY measurements, the samples were excited at 450nm.

3.2.7.4 Fourier Transform Infrared Spectroscopy

FTIR scans were run by using Spectrum Two FT-IR Spectrometer from Perkin Elmer. The measurements were performed by drying the PNC colloidal solutions on a diamond-attenuated total reflection unit in a range from 500 to 4000cm^{-1}.

3.2.7.5 Fluorescence Lifetime Imaging Microscopy

FLIM measurements were performed in the confocal configuration in an ambient atmosphere on a MicroTime200 fluorescence microscope from PicoQuant equipped with 440nm picosecond laser, 60 objective, PMA Hybrid single photon detector, and PicoHarp 300 TCSPC module. The excitation spot size was estimated at 550nm (FWHM). The lifetime decay profiles were reconvolution fitted using the instrument response function (IRF) recorded during the measurement.

3.3 Results and discussion

This section of the work investigates the effect of altering chain length of aliphatic amine ligands on the donor-acceptor interaction of $CsPbBr_3/TiO_2$ in solution and thin film state. The $CsPbBr_3$ PNCs, with oleic acid and oleylamine as capping ligands, were synthesized (Figure 3.2) using slightly modified hot-injection method as reported in the literature.

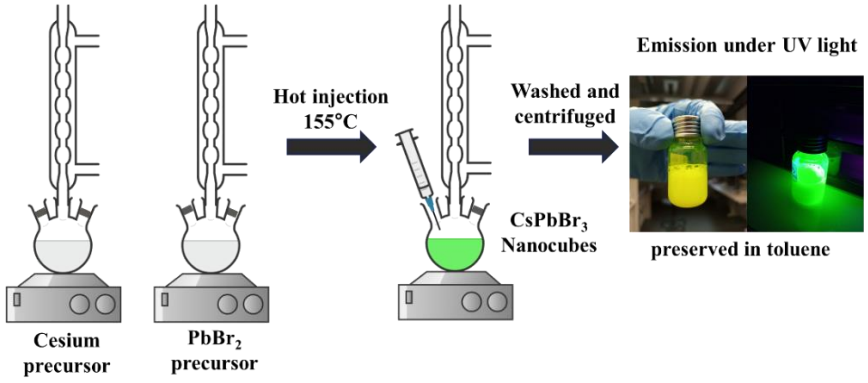

Figure 3.2) Schematic of hot injection process followed to produce $CsPbBr_3$ NCs

3.3.1 Optimization of ligand exchange

The as synthesized $CsPbBr_3$ PNCs suspension was subjected to post synthesis ligand exchange to ensure the co-relation between concentration of ligands. Figure 3.3A shows the scheme for post synthesis ligand exchange on as-synthesized $CsPbBr_3$ PNCs. 2µL (20 µmol) Butylamine was introduced to per 3 mL (µmol) of the PNCs suspension under ambient atmosphere while stirring at room temperature to prevent damage to the original OlAm-capped $CsPbBr_3$.

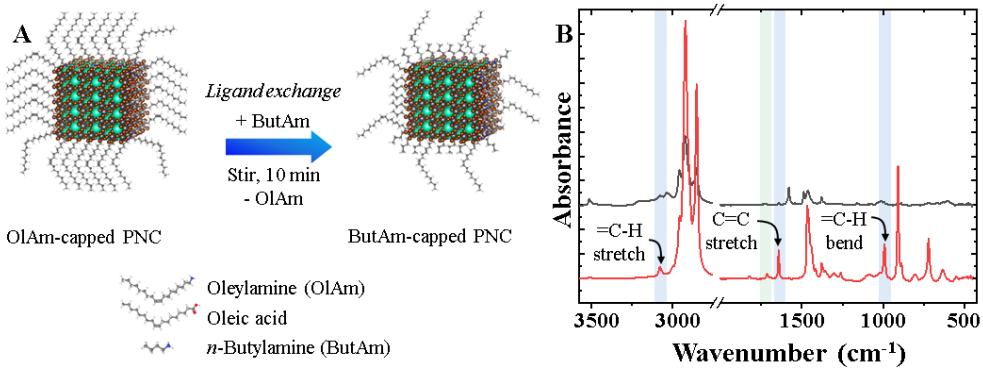

Figure 3.3) Scheme showing the exchange of long-chain oleylamine ligands on the surface of PNCs with short-chain butylamine ligands. (B) FTIR spectra of $CsPbBr_3$ PNCs before (red) and after (black) ligand exchange. The light blue regions correspond to the vibration frequencies of oleylamine, and the light green region corresponds to the vibration frequency of oleic acid.

Indeed, we observed that adding a significant amount of butylamine (≥10µL) to the same amount of OlAm-capped $CsPbBr_3$ PNCs causes a noticeable change in the colour of the colloidal solution, shifting from green to colourless and quenching of PL (Figure 3.4).

Previous investigations have demonstrated similar phenomena pertaining to ligand-assisted degradation and phase transitions in PNCs[105], [145]. The post-ligand exchange PNCs samples were subjected to purification by washing with acetonitrile to effectively eliminate unbound ligands. The purified ButAm-passivated PNCs were subsequently isolated by centrifugation and redispersed in anhydrous toluene for further characterization. The success of the ligand exchange process was verified using Fourier-transform infrared (FTIR) spectroscopy operated in attenuated total reflection (ATR) mode. Comparative FTIR spectral analysis of $CsPbBr_3$ PNCs functionalized with oleylamine (OlAm) and butylamine (ButAm) ligands revealed distinct vibrational features. Notably, absorption bands around ~3080 cm^{-1}, 1642 cm^{-1}, and 990 cm^{-1} were assigned to ═C─H stretching, C═C stretching, and ═C─H bending vibrational modes, respectively [146], corroborating the presence of alkene-related functionalities and confirming effective ligand substitution. The complete disappearance of the C═C stretching signal suggests that, from a qualitative perspective, all of the long chain ligands have been replaced by ButAm.

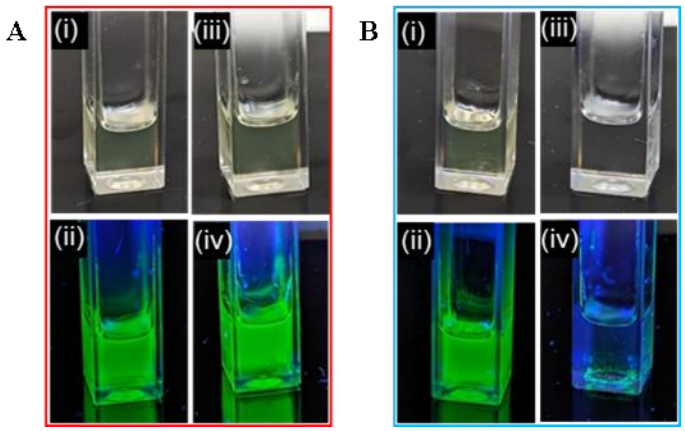

Figure 3.4) Stability of $CsPbBr_3$ PNCs after ligand-exchange with different amounts of butylamine. (A) Cuvette images of $CsPbBr_3$ PNC solution (i/ii) immediately, and (iii/iv) two hours after the treatment with 2 µL of butylamine. (B) Cuvette images of $CsPbBr_3$ PNC solution (i/ii) immediately and (iii/iv) two hours after the treatment with 10 µL of butylamine. (i/iii) and (ii/iv) in A and B are the images under room light and UV light, respectively.

These results suggest that, during the ligand exchange process, butylamine effectively displaces oleylamine from the surface of $CsPbBr_3$ PNCs. Simultaneously, a notable reduction in the surface concentration of oleic acid ligands is observed. This observation is consistent with the dynamic ligand binding mechanism, wherein oleate associates with the PNC surface predominantly as an ion pair in conjunction with oleylammonium .Consequently, substitution of oleylamine with butylamine disrupts this ion pair, facilitating the concurrent removal of oleic acid and leading to its diminished presence on the nanocrystal surface.

3.3.2 Morphological and Structural characterizations

The morphological and structural characteristics of $CsPbBr_3$ PNCs capped with oleylamine (OlAm) and butylamine (ButAm) were investigated using high-resolution scanning transmission electron microscopy (HR-STEM) and powder X-ray diffraction (XRD), as presented in figure 24. STEM imaging reveals that OlAm-capped PNCs exhibit a well-defined cubic morphology with an average edge length of approximately 12 nm, the shape and size retained following ligand exchange with butylamine (Figure 3.5A, B).

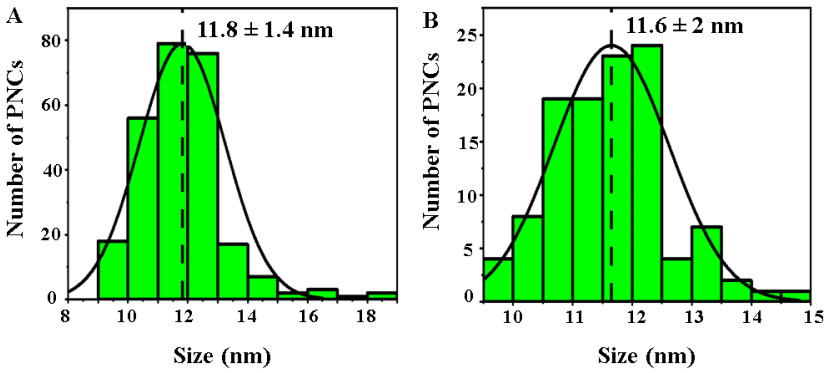

Figure 3.5) Size distribution on histograms for (A) oleylamine (OLAm)-capped and (B) butylamine (ButAm)-capped $CsPbBr_3$ PNCs

However, the ButAm-capped PNCs display notable aggregation on the TEM grid, attributed to a reduction in interparticle spacing due to the shorter alkyl chain length of the butylamine ligands. HR-STEM analysis of a representative ButAm-capped PNC (Figure 3.6D) shows a lattice fringe spacing of 5.81 Å, consistent with that observed for OlAm-capped counterparts (Figure 3.6C) and corresponding to the (101) crystallographic plane of orthorhombic $CsPbBr_3$ [147]. This assignment is further corroborated by the powder XRD patterns of both OlAm- and ButAm-passivated PNCs (Figure 3.6E).

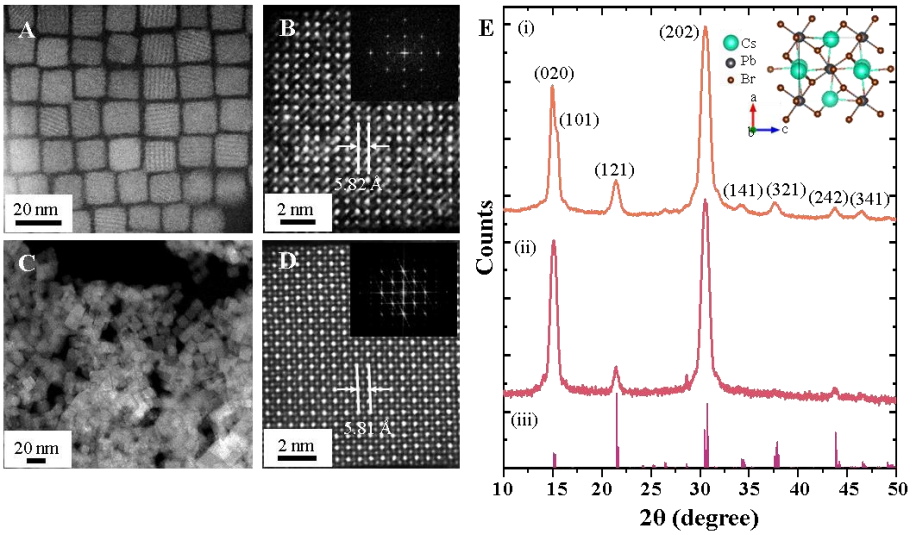

Figure 3.6) (A, C) STEM and (B, D) HR-STEM images of as-synthesized OlAm-capped (A, B), and ligand-exchanged ButAm-capped (C, D) $CsPbBr_3$ PNCs. The insets in B and D are the corresponding Fast-Fourier Transformed (FFT) images. (E) Powder XRD patterns of (i) ButAm-capped and (ii) OlAm-capped $CsPbBr_3$ PNCs which are compared with (iii) ref. 26. The inset shows the crystal structure of orthorhombic $CsPbBr_3$.

Specifically, the XRD pattern of the OlAm-capped sample (Figure 2E,i) exhibits a diffraction peak at $2\theta \approx 15°$, which splits into reflections indexed to the (020) and (101) planes, characteristic of the orthorhombic phase [148]. However, due to pronounced peak broadening—stemming from the nanocrystalline dimensions—the resolution of this peak splitting remains limited in both ligand systems compared to bulk $CsPbBr_3$ [149]. Nonetheless, all observable diffraction features are in good agreement with reference patterns for orthorhombic $CsPbBr_3$ reported in the literature[148].

3.3.3 Optical properties of PNCs

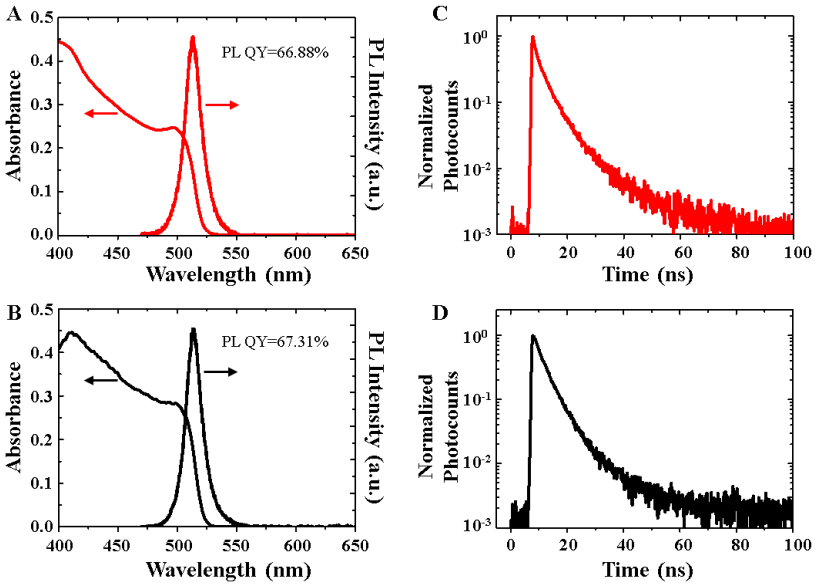

Figure 3.7) (A, B) Absorption and PL spectra of OlAm-capped (A) and ButAm-capped (B) $CsPbBr_3$ PNCs. (C, D) PL decay profiles of OlAm-capped (A) and ButAm-capped (B) $CsPbBr_3$ PNCs The standard deviation for steady state PL spectra is <1%.

The optical absorption and PL characteristics of $CsPbBr_3$ PNCs were systematically investigated before and after ligand exchange using UV–vis absorption spectroscopy, steady-state PL spectroscopy, and time-resolved PL measurements. As presented in Figure 3.7 A and Figure 3.7B, both oleylamine-

(OlAm) and butylamine- (ButAm) capped $CsPbBr_3$ PNCs exhibit nearly identical optical features. The absorption onset is observed at 528 nm, with a pronounced excitonic transition at approximately 500 nm, and a sharp PL emission peak centered at 510 nm, featuring a full width at half maximum (FWHM) of 18 nm. Both samples demonstrate intense green emission with absolute PL quantum yields (QY) of ~67%, as shown in Figure 3.8A and Figure 3.8B, indicating minimal alteration of emissive properties following ligand exchange.

To probe excitonic recombination dynamics, time-correlated single-photon counting (TCSPC) measurements were conducted on both OlAm- and ButAm-capped PNC dispersions, as shown in Figure 3.7C and Figure 3.7D, respectively. The decay profiles were analysed using a tri-exponential fitting model to derive intensity-weighted average lifetimes (τ_{AVG}), yielding values of 5.96 ns and 5.50 ns for OlAm- and ButAm-capped PNCs, respectively. These comparable lifetimes further corroborate that post-synthetic ligand exchange does not compromise the excitonic recombination behaviour or optical integrity of $CsPbBr_3$ PNCs.

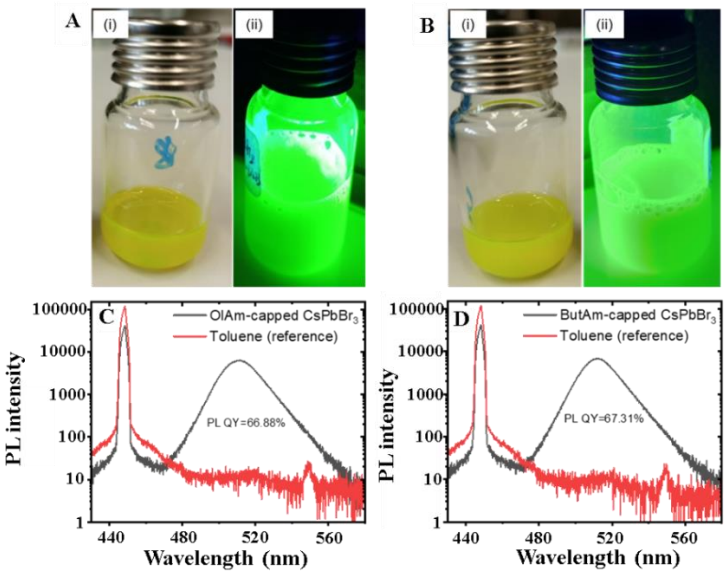

Figure 3.8) (A, B) Colloidal solutions of (A) OlAm-capped and (B) ButAm-capped $CsPbBr_3$ PNCs (i) at room light and (ii) under 365 nm UV lamp excitation. (B, C) PL spectra recorded with an integrating sphere in a PL spectrometer for the absolute PLQY measurements of (B) OlAm-capped and (D) ButAm-capped $CsPbBr_3$ PNC colloidal solutions. Toluene was used as the reference.

3.3.4 Optical and structural analysis of the quencher

The Figure 3.9 shows the optical and structural characterizations for TiO_2 nanoparticles.

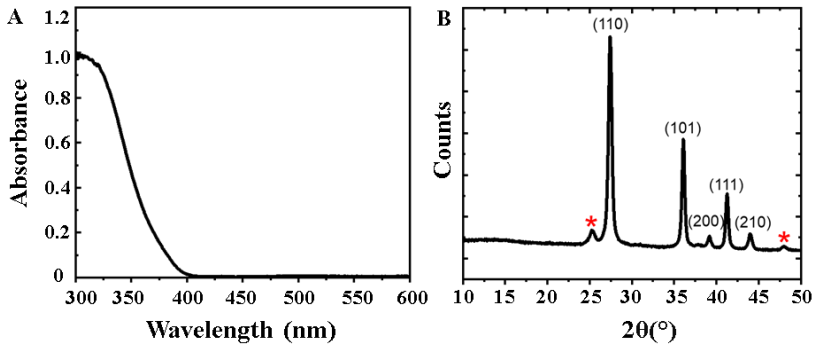

Figure 3.9) (A) UV-Visible absorption spectrum of TiO_2 nanoparticle suspension. (B) Powder X-ray diffraction (XRD) pattern of TNPs. The indexed XRD peaks are for Rutile phase, while the XRD peaks labelled with (*) are for the Anatase phase of TiO_2.

In colloidal dispersions, PL quenching exhibited a clear dependence on ligand chain length, indicative of donor–acceptor interactions that may facilitate interfacial charge transfer between $CsPbBr_3$ PNCs and TiO_2 nanoparticles (NPs). Notably, ButAm-capped $CsPbBr_3$ PNCs demonstrated significantly enhanced PL quenching compared to their OlAm-capped counterparts upon photoexcitation, suggesting more efficient electron transfer to TiO_2. However, the PL decay profiles remained unchanged with increasing TiO_2 concentration, precluding a direct assessment of exciton recombination dynamics and their modification by interfacial electron transfer in the solution phase.

3.3.5 Interaction of PNCs with TiO_2 in solution state

Having confirmed the retention of structural and optoelectronic properties post-ligand exchange, we next investigated how ligand chain length modifies donor–acceptor interactions between $CsPbBr_3$ PNCs and TiO_2 nanostructures, including nanoparticles (NPs) and nanotubes (NTs), in both solution and thin-film configurations. In the solution phase, PL quenching experiments were performed by incrementally introducing a TiO_2 NP suspension into toluene-dispersed PNC solutions. Prior to titration, the PNC dispersions were diluted to an optical density (OD) of 0.5 at the excitonic peak to standardize nanocrystal concentration and suppress inner filter effects.

3.3.5.1 Effect on the PL spectra

TiO_2 nanoparticles, with a size range of 50–150 nm, were dispersed in toluene at a concentration of 1 g/14 mL to prepare the stock suspension. Aliquots ranging from 0 to 240 µL were added to the PNC dispersions, corresponding to final TiO_2 concentrations between 0 and 120 mM. PL measurements (Figure 4A) revealed negligible intensity change in OlAm-capped PNCs upon TiO_2 addition, indicating limited electronic coupling. In contrast, ButAm-capped PNCs exhibited progressive PL quenching as TiO_2 concentration increased (Figure 3.10A and Figure 3.10B), suggesting enhanced interfacial interactions.

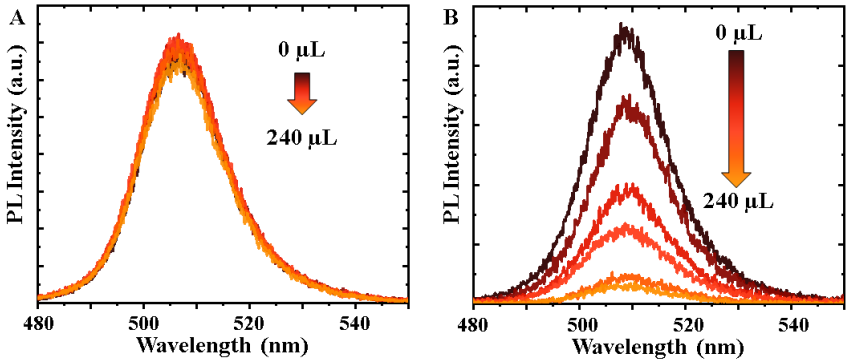

Figure 3.10) (A, B) PL spectra showing PL quenching of $CsPbBr_3$ PNCs by TiO_2 in solution before (A) and after (B) ligand exchange. The standard deviation for steady state PL spectra is <1% of intensity.

All PL spectra were corrected for dilution effects (Figure 3.11), and absorption spectra (Figure 3.12) confirmed colloidal stability across all concentrations, ruling out aggregation-induced artifacts. These observations suggest that the reduced steric hindrance and interparticle spacing associated with short-chain ButAm ligands facilitate closer PNC–TiO_2 proximity, enhancing donor–acceptor electronic interactions. Given the known type-II band alignment between $CsPbBr_3$ and TiO_2, [138] the observed PL quenching is attributed to interfacial electron transfer from the PNCs to TiO_2. Nevertheless, to understand this further, one must look closer into the dynamic aspects of the quenching interaction.

3.3.5.1.1 Dilution correction

The addition of toluene causes a decrease in PL intensity of PNC solution due to the dilution effect. Therefore, to separate out the effect of dilution from the effect of charge transfer interaction on the PL

intensity of PNC solution, two separate set of experiments were carried out. In the first experiment, TiO_2 suspended in toluene was added to PNC solution following a step wise manner as presented above and the corresponding PL spectra were recorded. In the second set of experiments, similar volume of only toluene (but without TiO_2) was added in a step wise manner to the PNC solution to obtain a set of corresponding PL spectra. The data from both experiments were compared to subtract out the effect of toluene dilution.

We divide the PNC solution into 2 cuvettes (cuvette1 and cuvette 2), each having equal volume. We take cuvette1, record the initial PL intensity (P1) and add 20 µL (TiO_2/toluene suspension) to it, which causes a decrease in the PL intensity to P1'. This decrease is ascribed to the combined effect of charge transfer and dilution.

Again, we take cuvette 2, record the initial PL intensity (P2) and add 20µL of pure toluene to it, causing decrease in PL intensity to P2'. This decrease in PL intensity is now ascribed to only the dilution effect.

For the dilution correction on PL spectra, we carry out a two-step calculation:

1. (P2 - P2' / P2) = Z (dilution factor)
2. P1' + (P1 × Z) = Final PL intensity without the dilution effect of solvent (toluene)

The same process was repeated for all the subsequent step wise addition of TiO_2 suspension to the PNC solution.

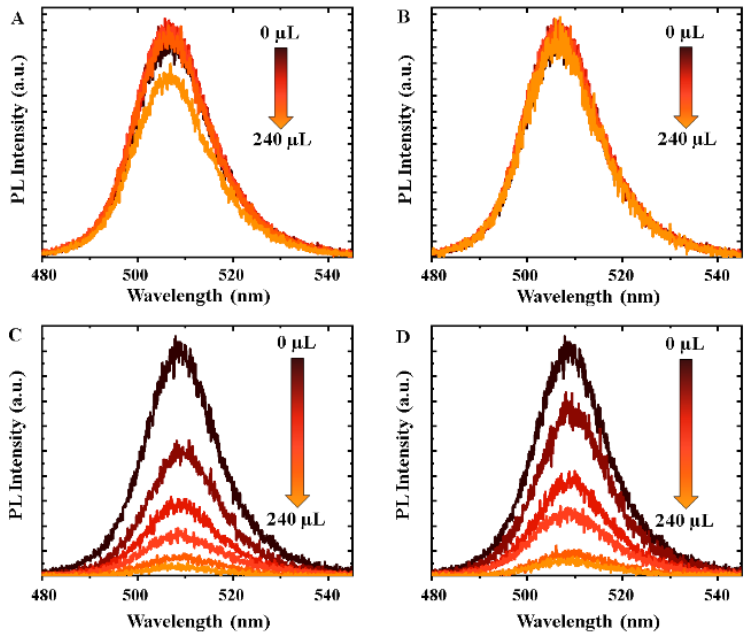

Figure 3.11) PL spectra of (A,B) oleylamine-capped and (C,D) butylamine-capped $CsPbBr_3$ PNCs showing the effect of dilution on adding different volumes of toluene/TiO_2 solution. (A,C) before dilution correction and (B,D) after dilution correction.

3.3.5.2 Inner filtering effects

Finally, we considered the potential influence of inner filter effects (IFE), which may arise at high quencher concentrations due to absorption or scattering of the excitation light by TiO_2, artificially diminishing PL intensity[150]. However, this contribution is deemed negligible in our system, as equivalent additions of TiO_2 to OlAm-capped PNC dispersions did not produce PL attenuation

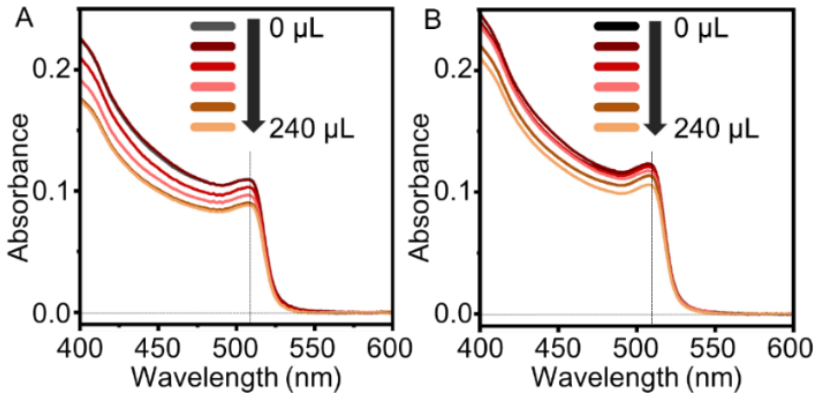

Figure 3.12) Absorption spectra of butylamine-capped $CsPbBr_3$ PNCs with the (A) addition of toluene and (B) TiO_2-suspended toluene at different volumes (indicated in the inset), indicating colloidal as well as material stability under dilution

Figure 3.12 confirming that the observed quenching in ButAm-capped PNCs is not an artifact of IFE but is instead attributable to interfacial electronic interactions.

3.3.5.3 Effect on charge carrier dynamics and Stern-Volmer plot

To investigate the mechanism of PL quenching in solution, Stern–Volmer (SV)[151] analyses were conducted for OlAm- and ButAm-capped $CsPbBr_3$ PNCs, using the PL intensity data from Figure 3.10.

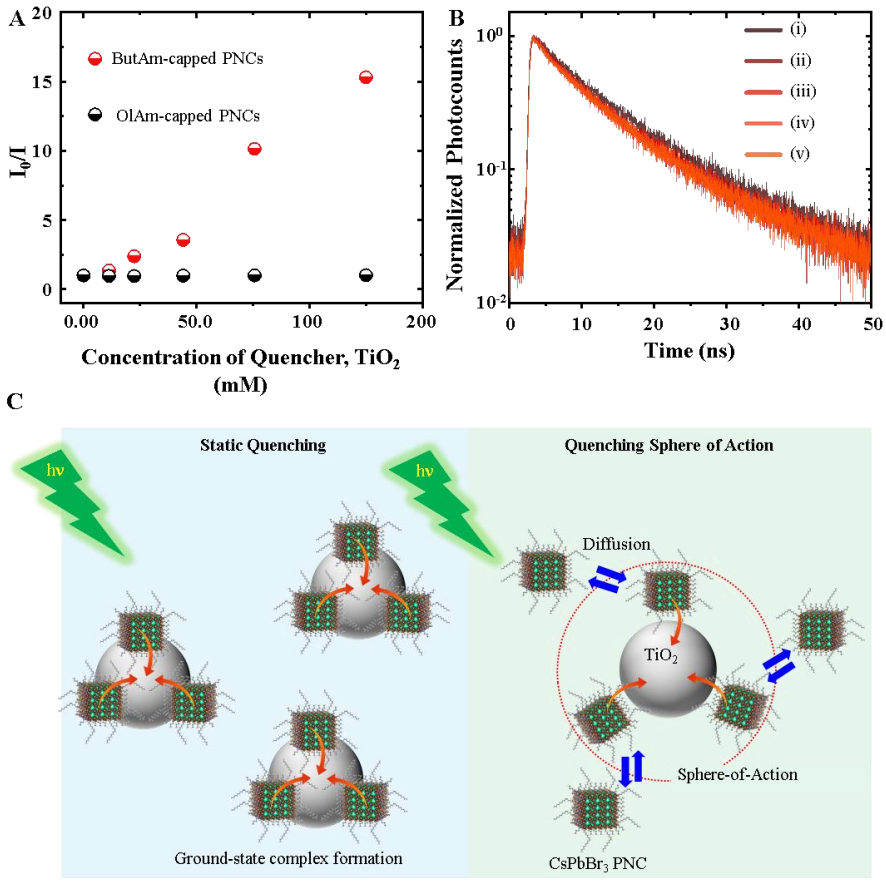

Figure 3.13) (A) Stern-Volmer plots for OlAm-capped and ButAm-capped $CsPbBr_3$ PNC colloidal solutions in the presence of TiO_2 as quencher. (B) PL decay profiles of ButAm-capped $CsPbBr_3$ PNC colloidal solution obtained after adding (i) 0 µL, (ii) 20 µL, (iii) 40 µL, (iv) 80 µL, and (vi) 240 µL of TiO_2 NP suspension in toluene. (C) Mechanism of PL quenching of $CsPbBr_3$ PNCs by TiO_2 NPs in solution (the image is for demonstration and not to scale)

The corresponding SV plots are presented in Figure 3.13A. For OlAm-capped PNCs, the SV plot shows a negligible slope, indicating an absence of PL quenching upon the addition of TiO_2 nanoparticles (NPs).

In contrast, the ButAm-capped PNCs exhibit a distinctly non-linear SV behaviour—initially linear at low TiO_2 concentrations, transitioning to an upward-curved profile at higher concentrations. This curvature suggests the coexistence of both static and dynamic quenching processes[152].

In static quenching, quenchers form ground-state, non-emissive complexes with the donor prior to excitation, whereas dynamic quenching involves collisional interactions between the quencher and excited-state donor, suppressing radiative recombination. Both mechanisms yield linear SV plots; however, they are distinguishable by time-resolved PL dynamics. Specifically, static quenching does not affect the PL lifetime, while dynamic quenching results in a concentration-dependent decrease in lifetime[152]. In the present study, the PL lifetime of ButAm-capped $CsPbBr_3$ PNCs remained unchanged across all TiO_2 concentrations (Figure 3.13B), thereby ruling out significant dynamic quenching and contradicting the non-linear trend in the SV plot if it is interpreted as a mixture of static and dynamic mechanisms.

To further understand this phenomenon, we extended our analysis beyond the conventional SV model by incorporating the sphere-of-action quenching mechanism, [151] [152], as illustrated in Figure 3.13C. Under this model, apparent static quenching arises from proximity-induced interactions without requiring a stable ground-state complex. Specifically, the short-chain butylamine ligands and reduced oleic acid surface coverage promote the adsorption of ButAm-capped PNCs onto TiO_2 surfaces, facilitating static quenching via surface complexation. At elevated TiO_2 concentrations, the increasing curvature of the SV plot is attributed to the sphere-of-action quenching, where PL quenching occurs within a defined spatial volume surrounding the donor due to the high local probability of donor–acceptor proximity at the moment of excitation. In this regime, quenching is efficient even without direct complex formation, driven by proximity rather than diffusion-limited encounters.

In contrast, OlAm-capped PNCs possess bulky oleylamine ligands and a higher oleic acid content, creating a steric and solvophobic barrier that prevents effective interaction with TiO_2 NPs. This results in no static or dynamic quenching, consistent with the flat SV profile and stable PL intensities.

Supporting this mechanistic interpretation, Vinçon et al [153] recently demonstrated PL quenching in lecithin-capped $CsPbBr_3$ quantum dots by $BiBr_3$ via a similar sphere-of-action framework, where significant PL quenching occurred without observable changes in PL lifetime. While their system involved defect-induced quenching via Bi^{3+} ion incorporation, our observations implicate electron transfer from ButAm-capped PNCs to TiO_2 NPs as the dominant quenching pathway mediated by donor–acceptor interactions.

3.3.6 Interaction of PNCs with TiO_2 in solution state

To overcome this limitation, we employed confocal fluorescence lifetime imaging microscopy (FLIM) and time-resolved PL spectroscopy to examine the $CsPbBr_3$–TiO_2 donor–acceptor interface in the solid state, where interparticle distances and morphological order are more controlled. To further elaborate the influence of TiO_2 microstructure on electron transfer kinetics, two configurations were investigated: (i) films prepared by spin-coating mixtures of TiO_2 NPs and either OlAm- or ButAm-capped $CsPbBr_3$ PNCs onto glass substrates, and (ii) layered heterostructures formed by spin-coating PNCs onto anodically grown TiO_2 nanotube (NT) arrays supported on Ti substrates. In both cases, deposition was followed by argon-assisted drying.

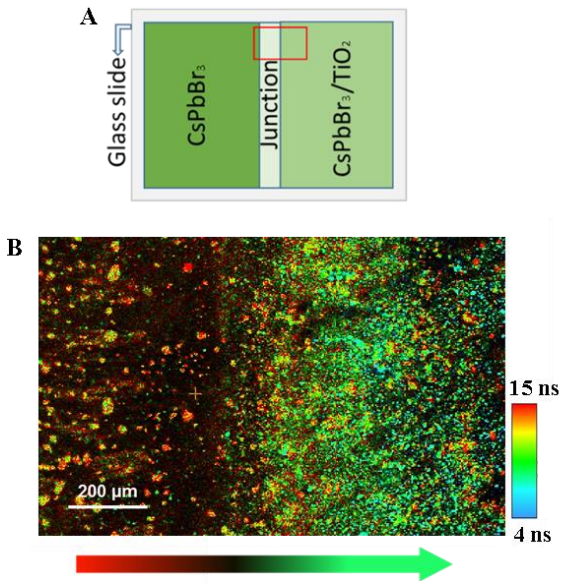

Figure 3.14) A schematic representation of heterostructure interface between $CsPbBr_3$ PNCs and $CsPbBr_3/TiO_2$ heterostructures supported by FLIM imaging

Figure 3.14 provides a general perspective on the interfacial interactions between $CsPbBr_3$ and TiO_2 within thin-film heterojunction architectures. Specifically, Figure 3.14A presents a schematic illustration of the heterostructure formed between a pristine $CsPbBr_3$ thin film and a composite $CsPbBr_3$–TiO_2 region. This schematic serves as a conceptual framework for assessing whether donor–acceptor interactions are established across the interface. To spatially resolve these interactions, fluorescence lifetime imaging microscopy (FLIM) was employed to capture lifetime variations across three distinct regions of the heterojunction: the pure $CsPbBr_3$ film, the interfacial junction, and the $CsPbBr_3$–TiO_2 composite area. The FLIM map (Figure 3.14B) reveals a clear gradient in PL lifetimes, with a systematic reduction in time-resolved PL (TRPL) lifetime as the probe moves from the $CsPbBr_3$ region toward the $CsPbBr_3$–TiO_2 region. This trend, visually represented in the FLIM colour scale and further corroborated by Figure 5c, strongly suggests effective exciton quenching and enhanced charge transfer at the $CsPbBr_3$–TiO_2 interface.

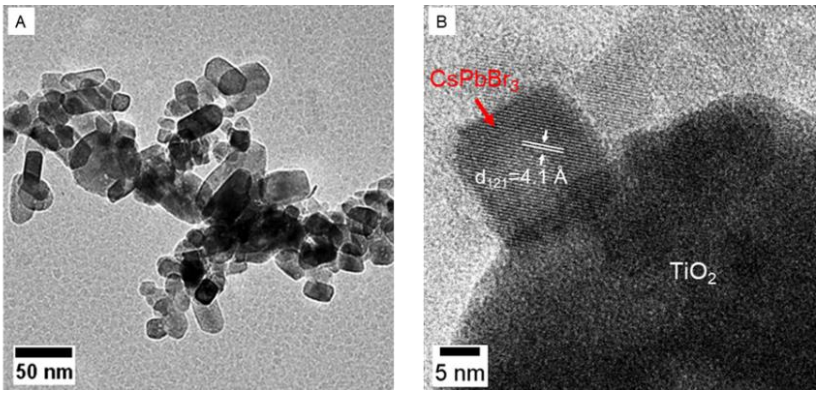

Figure 3.15) Transmission electron microscopy (TEM) images of (A) TNPs and (B) a $CsPbBr_3$ PNC on the TNPs showing a donor-acceptor interface. A lattice fringe of 4.1 Å in $CsPbBr_3$ PNC corresponds to the (121) plane of an orthorhombic crystal structure of the bulk $CsPbBr_3$

Therefore, for the initial study, we conclude that contrary to the solution-phase behaviour, all solid-state samples exhibited accelerated PL decay in the presence of TiO_2, regardless of ligand type, indicative of enhanced non-radiative exciton recombination due to increased donor–acceptor electronic coupling[116]. The formation of nanoscale donor–acceptor heterojunctions at the $CsPbBr_3$–TiO_2 interface in the solid-state was also confirmed by transmission electron microscopy (Figure 3.15). These

observations are consistent with reported work in the literature, wherein PL lifetime shortening across $FAPbBr_3$ or $CsPbBr_3$ PNC–TiO_2 heterojunctions was attributed to diffusion-limited electron transfer at the interface [154].However, that study did not resolve the role of surface ligand chemistry in governing the efficiency of electron transfer, either in solution or film.

3.3.6.1.1 Interaction with TiO_2 nanoparticles

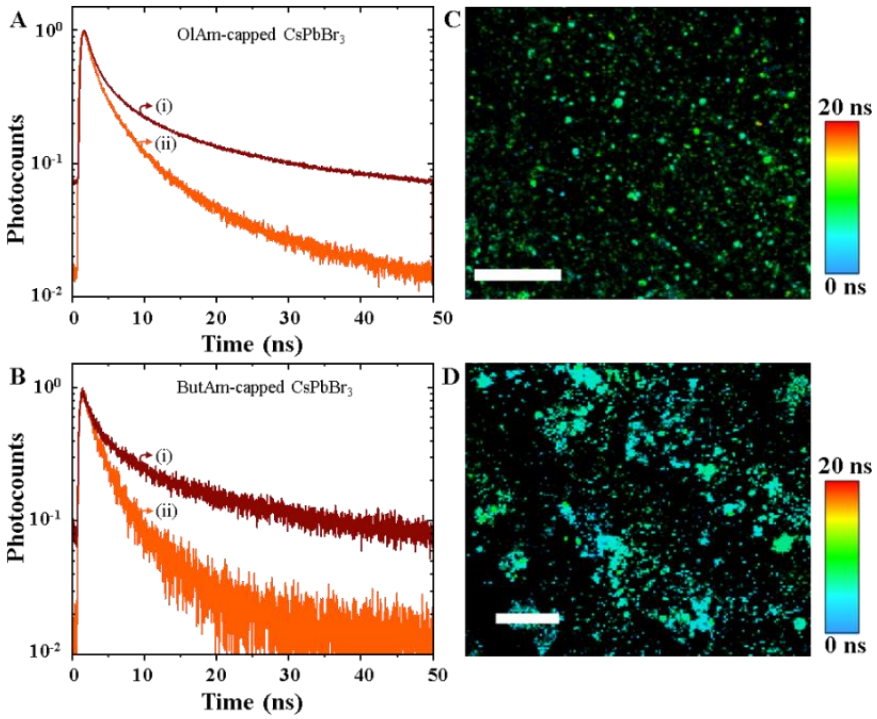

Figure 3.16) (A, B) PL decay profiles of OlAm-capped (A) and ButAm-capped (B) $CsPbBr_3$ PNC films before (i) and after (ii) mixing PNCs with TiO_2. (C, D) FLIM images of TiO_2 mixed OlAm-capped (C) and ButAm-capped (D) $CsPbBr_3$ films. The scale bars are 25 µm and 100 µm in C and D, respectively.

In contrast, the present work systematically investigates the role of ligand chain length in modifying donor–acceptor interactions and interfacial electron transfer in both phases. FLIM data for films incorporating TiO_2 NPs and $CsPbBr_3$ PNCs capped with either OlAm or ButAm are shown in Figure 3.16C and Figure 3.16D, with the corresponding PL decay profiles in Figure 3.16A and Figure 3.16B. Control films comprising only the PNCs (without TiO_2) exhibited similar average PL lifetimes (~14 ns) regardless of ligand type. However, the incorporation of TiO_2 led to a significant reduction in PL lifetimes, more pronounced for ButAm-capped PNCs (~6 ns) compared to OlAm-capped PNCs (~9 ns). These results indicate that electron transfer from PNCs to TiO_2 is operative in the solid state for both ligand systems but is more efficient in the case of short-chain butylamine ligands, likely due to reduced steric hindrance and improved interfacial contact.

3.3.6.2 Photoluminescence Quantum Yield of $CsPbBr_3$-TiO_2 nanocomposite thin films

To support the findings discussed above, a separate set of samples with high photoluminescence quantum yields (PLQYs) were synthesized and utilized to develop thin films composed of oleylamine (OlAm)- and butylamine (ButAm)-capped $CsPbBr_3$ PNCs, both in the absence and presence of TiO_2, and the results are presented in the Figure 3.17. These results are shown solely to demonstrate the qualitative aspect of interaction between the PNCs and TNPs. The OlAm-capped $CsPbBr_3$ PNC films exhibit a high PLQY of approximately 84%, which decreases to 74% upon incorporation of TiO_2, indicating a moderate degree of nonradiative charge transfer. In contrast, the PLQY of ButAm-capped

$CsPbBr_3$ PNCs significantly drops to 52% upon TiO_2 integration. This pronounced reduction in PLQY for the short-chain ligand system provides compelling evidence of efficient photoinduced electron transfer in the $CsPbBr_3$–TiO_2 heterostructures, with the extent of quenching strongly influenced by the ligand chain length.

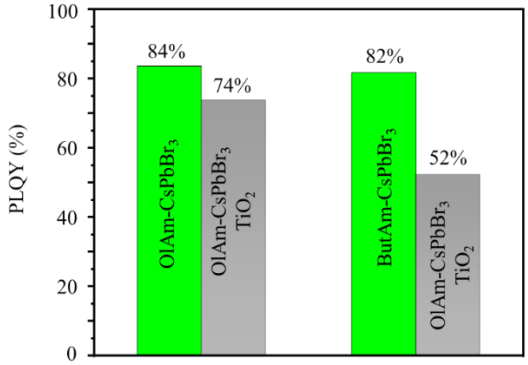

Figure 3.17) Photoluminescence quantum yield for OlAm-capped and ButAm-capped $CsPbBr_3$. The maximum value of deviation recorded for measurements of PLQY is <3%.

The apparent difference between the absence of PL quenching in solution and the pronounced quenching in solid films for OlAm-capped PNCs suggests that solvent-mediated effects, in addition to ligand chain length, play a critical role in suppressing donor–acceptor interactions in solution. Thus, our findings highlight the interplay between surface ligand composition, solvent environment, and interfacial morphology in governing charge transfer processes in perovskite–metal oxide hybrid systems.

3.3.6.2.1 Interaction with Titania Nanotubes Arrays

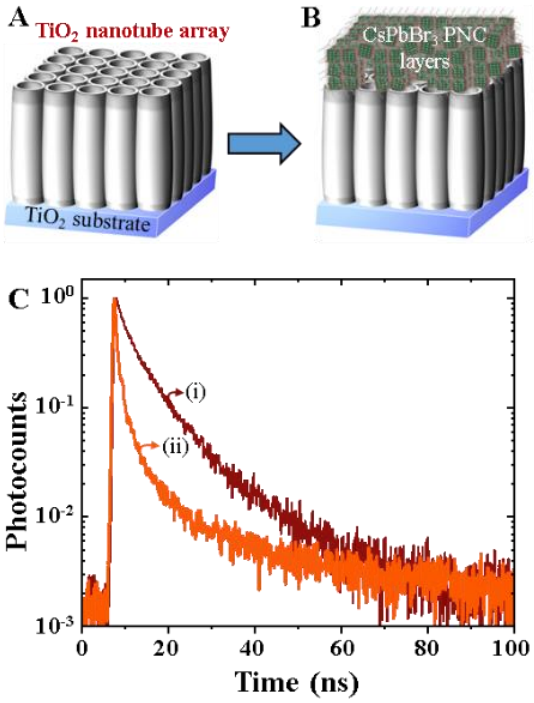

Figure 3.18) (A, B) Scheme showing anodically grown TiO_2 NT array on a TiO_2 substrate (A) without $CsPbBr_3$ PNCs and (B) with $CsPbBr_3$ PNCs deposited on the top (the image is not to scale). (C) PL decay profiles of ButAm-capped $CsPbBr_3$ PNCs deposited on (i) a glass coverslip and (ii) the top of the TiO_2 NT array.

Figure 3.18A and Figure 3.18B schematically depict the structural configuration of the TiO_2 nanotube (NT) array before and after the deposition of $CsPbBr_3$ PNCs(The image is not to scale). Corresponding SEM images, which provide morphological confirmation of the deposition process, are shown in Figure 3.19. Figure 7C presents time-resolved PL decay profiles for ButAm-capped $CsPbBr_3$ PNCs deposited onto glass substrates and TiO_2 NT arrays. A noticeably faster PL decay is observed for PNCs interfaced with the TiO_2 NT substrate compared to those on bare glass, consistent with enhanced non-radiative pathways arising from interfacial charge transfer, as discussed earlier. The following figure shows the $CsPbBr_3$–TiO_2 TNTA heterostructure under SEM.

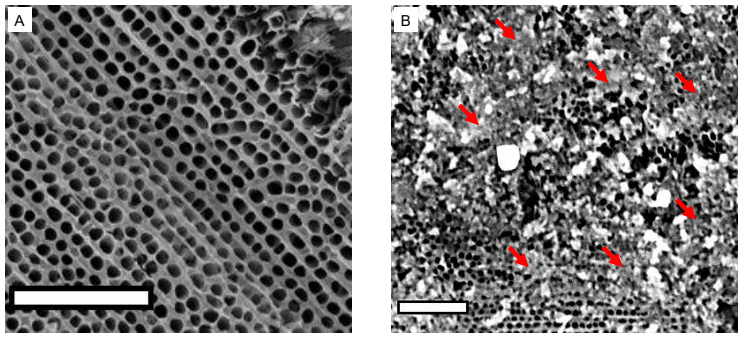

Figure 3.19) Scanning electron microscopy images of (A) anodically grown bare TNTAs and (B) TNTAs with $CsPbBr_3$ PNCs deposited on the top. Some patches of deposited PNCs are indicated by red arrows. Scale bars in both images are 1 µm.

To quantitatively assess this behaviour, PL decay curves were fitted using a tri-exponential decay model, yielding individual lifetime components (τ_i), their corresponding fractional intensities (f_i), and the average PL lifetime (τ_{avg}). This analysis was conducted for three configurations: $CsPbBr_3$ PNCs on glass (control), $CsPbBr_3$–TiO_2 NP composite films, and $CsPbBr_3$ PNCs on TiO_2 NT arrays. The comparative results are summarized in Table 3.1.

In PNC films lacking TiO_2, the PL emission is predominantly governed by the longest lifetime component, τ_3, with average values of 19 ns (66% contribution) for OlAm-capped PNCs and 18 ns (72% contribution) for ButAm-capped PNCs. The shortest decay component, τ_1 (1.18 ns for OlAm and 1.10 ns for ButAm), accounts for less than 10% of the overall emission, while the intermediate component, τ_2 (4.2 ns for OlAm and 3.8 ns for ButAm), contributes approximately 20–25%.

Previous studies attribute τ_1 to rapid non-radiative recombination facilitated by charge carrier trapping into deep or shallow defect states[155]. These trap-mediated processes lead to fast depletion of free carriers from the B.E, with minimal detrapping, thereby suppressing radiative recombination[156]. The τ_2 component is typically associated with a combination of band-edge recombination and trap-state dynamics. At this stage, shallow traps are partially populated, which modifies the balance between carrier trapping and detrapping. Although the trapping rate decreases, the inefficiency in detrapping limits the extension of carrier lifetime, rendering τ_2 only marginally longer than τ_1 [156]. In contrast, τ_3 is generally linked to radiative recombination occurring at or near the B.E, where a significant portion of shallow traps are saturated. This results in transient trapping followed by successful detrapping, ultimately extending the PL lifetime due to slowed recombination kinetics [155] [156]. The dominance of τ_3 in the PNC films without TiO_2 indicates that the recombination dynamics are primarily radiative, which is in agreement with the high absolute PLQY values reported for these pristine samples.

A clear modification in the relative contributions of radiative and nonradiative exciton recombination processes to the overall PL lifetime of $CsPbBr_3$ PNCs was observed upon incorporation of TiO_2, as summarized in Table 1.

Table 3.1) PL lifetime components (τi), corresponding fractional contribution (fi) of each decay time to the steady-state intensity, and intensity-weighted average PL lifetimes (τ) obtained from multiexponential fitting of PL decay profiles of Olm-capped and ButAm-capped $CsPbBr_3$ PNC film, $CsPbBr_3$-TiO_2 film and $CsPbBr_3$ PNCs deposited on the top of a TiO_2 NT array.

	τ_1 (ns)	f_1	τ_2 (ns)	f_2	τ_3 (ns)	f_3	χ^2	Average τ (ns)
OlAm-$CsPbBr_3$ PNC film	1.18 ± 0.01	0.099	4.20 ± 0.11	0.241	19.00 ± 0.16	0.660	0.999	13.67 ± 0.09
ButAm-$CsPbBr_3$ PNC film	1.10 ± 0.11	0.062	3.80 ± 0.52	0.215	18.00 ± 1.2	0.723	0.978	13.90 ± 0.81
OlAm-$CsPbBr_3$ PNC+TiO_2 NP film	1.50 ± 0.03	0.232	5.10 ± 0.13	0.435	19.00 ± 1	0.333	0.998	8.89 ± 0.29
ButAm-$CsPbBr_3$ PNC+TiO_2 NP film	1.40 ± 0.24	0.221	3.60 ± 0.51	0.454	12.00 ± 1.8	0.325	0.980	5.84 ± 0.37
ButAm-$CsPbBr_3$ PNCs on TiO_2 NT array	0.35 ± 0.3	0.230	1.83 ± 0.07	0.434	9.33 ± 0.01	0.332	0.995	3.97 ± 0.06

In the case of OlAm-capped $CsPbBr_3$ PNC–TiO_2 NP composite films, the individual lifetime components (τ_1, τ_2, τ_3) remained quantitatively similar to those of the pristine film (i.e., without TiO_2). However, the fractional contributions (f_i) of these components to the average PL lifetime underwent significant redistribution—from a dominant long-lived τ_3 contribution (66%) in the control film to a more balanced distribution with τ_3 reduced to 33%, τ_2 increased from 24% to 44%, and τ_1 rising from 10% to 23%. This shift indicates that the incorporation of TiO_2 NPs does not introduce additional nonradiative decay channels but instead modifies the recombination dynamics, possibly by influencing pre-existing trap states. The altered exciton dynamics suggest that TiO_2 acts as a passive electron acceptor, facilitating exciton deactivation via enhanced population of trap-assisted nonradiative pathways, rather than by introducing new defect states. Nonetheless, further investigation is required to fully investigate the interplay between charge transfer processes and the evolution of trap state energetics in ligand-stabilized metal halide perovskite systems.

In contrast, for ButAm-capped $CsPbBr_3$ PNC–TiO_2 NP films, a more pronounced shift in the PL decay dynamics was observed. The contribution of the longest-lived component τ_3 decreased from 72% to 33%, while the contributions of τ_1 and τ_2 increased from 6% to 22% and from 22% to 45%, respectively. Moreover, τ_3 itself decreased from 18 ns to 12 ns. These observations point to a dual impact of TiO_2 NPs: not only do they enhance nonradiative exciton recombination via interaction with shallow and deep trap states, but they also influence radiative recombination by accelerating electron transfer processes. Specifically, we propose that in ButAm-capped PNCs, TiO_2 competes with the intrinsic detrapping of electrons from shallow trap states to the B.E. Electron transfer to TiO_2 becomes a

dominant pathway, thereby diminishing the likelihood of delayed radiative recombination and resulting in an overall shortening of τ_3.

A similar trend is observed when ButAm-capped $CsPbBr_3$ PNCs are deposited onto a TiO_2 nanotube (NT) array. While the redistribution of lifetime component contributions mirrors that seen in the PNC–TiO_2 NP films, all three lifetime constants are significantly reduced: τ_1 drops to 0.35 ns, τ_2 to 1.83 ns, and τ_3 to 9 ns. Notably, the dramatic reduction in τ_1 suggests the emergence of additional fast nonradiative recombination channels that are absent in the NP-based systems. To evaluate the electron transfer rate constants (K_{ET}) from $CsPbBr_3$ PNCs to TiO_2 nanoparticles (TNPs), we used the average PL lifetimes and applied the following equation to obtain apparent rate of electron transfer:

$$K_{\mathrm{ET}} = \frac{1}{\tau_{\mathrm{PNC.TiO2}}} - \frac{1}{\tau_{\mathrm{PNC}}}$$

Where τ_{PNC} and $\tau_{PNC.TiO_2}$ represent the τ_{avg} PL lifetimes of the ButAm-capped $CsPbBr_3$ PNCs deposited on glass substrates and on TNTAs, respectively. The electron transfer rate constants were found to be 1.8×10^8 s^{-1} for ButAm-capped PNCs (BAmPNC/TNTAs)

These findings indicate that the one-dimensional architecture and higher contact area of the TiO_2 NTs (provided by the absence of ligands) promote more efficient charge extraction from the PNCs, thereby introducing new nonradiative deactivation pathways in addition to modifying existing exciton dynamics. This underscores the critical role of TiO_2 morphology and interfacial engineering in dictating charge transfer kinetics in perovskite–semiconductor hybrid systems.

3.4 Summary

In this study, we systematically investigated the influence of ligand chain length on the photophysical behaviour of $CsPbBr_3$ PNCs by employing a post-synthetic ligand exchange approach. This methodology facilitated the substitution of native long-chain ligands with shorter-chain analogs, thereby enabling the evaluation of distance-dependent donor–acceptor interactions and their implications for PL quenching and electron transfer phenomena. Our analysis primarily focused on investigating the interaction dynamics between $CsPbBr_3$ PNCs and TiO_2 nanostructures in both colloidal (solution-phase) and solid-state environments.

In solution, $CsPbBr_3$ PNCs functionalized with short chain butylamine ligands demonstrated enhanced electronic coupling with TiO_2 nanoparticles, as evidenced by PL quenching. The quenching behaviour exhibited characteristics of both static mechanisms and proximity-induced quenching via the sphere-of-action model. In contrast, PNCs capped with long-chain oleylamine ligands displayed negligible PL quenching upon TiO_2 addition, indicating inefficient donor–acceptor interactions likely due to steric and electronic passivation effects imparted by the bulky ligands. Upon transitioning to the solid-state, however, both ligand types, short-chain and long-chain, exhibited significantly accelerated PL decay in the presence of TiO_2, suggesting the formation of efficient charge-transfer interfaces and increased nonradiative recombination rates. Notably, this difference between solution and solid-state behaviour in the case of oleylamine-capped PNCs highlights the role of solvent-mediated effects in modifying interfacial charge transfer processes. Furthermore, comparative analysis between films incorporating TiO_2 nanoparticles and those employing highly structured TiO_2 nanotube (NT) arrays revealed that the latter facilitated more pronounced exciton quenching, particularly in systems with short-chain ligands. This observation highlights the critical impact of TiO_2 morphology on interfacial charge dynamics and the effectiveness of electron extraction. Collectively, these findings investigate the complex interplay between surface ligand architecture and TiO_2 structural characteristics in governing exciton recombination and charge transfer in $CsPbBr_3$ PNC-based systems. Such insights are essential for the rational design of perovskite-based optoelectronic devices, where precise control over interfacial chemistry and nanostructure is imperative for optimizing performance.

3.5 Future outlook

$CsPbBr_3$ nanostructures possess enormous potential for photocatalytic and optical applications. The stability for these materials is a concern, which could be resolved using different techniques such as developing type-II core-shell structures, depending on the application. The stable shell material could provide the needed protection as well as the ability to transfer the charges by providing the appropriate potential energy level. Furthermore, impact of variety of ligands on the charge carrier dynamics can also be investigated.

4 Manganese doped $CsPbBr_3$ Perovskite Nanosheets-understanding the charge carrier dynamics of surface and bulk Mn atoms

In the preceding chapter, we explored surface engineering as a strategy to tailor the charge carrier dynamics within a nano heterostructure system. In this context, an intriguing question arises: what would be the effect of introducing a dopant into both the surface and bulk of the perovskite nanostructure acting as a sensitizer? Specifically, how would charge carriers behave under such conditions if the dopant possesses a spin-forbidden electronic transition—resulting in excited charge carriers requiring tens of microseconds before undergoing radiative recombination back to the valence band?

This chapter presents an investigation into Cesium lead bromide nanosheets (NSs) doped with Manganese atoms (Mn-$CsPbBr_3$), evaluated as potential sensitizers for various TiO_2 morphologies. The influence of Mn^{2+} doping on charge carrier dynamics is explored by analyzing PL decay lifetimes of surface- and bulk-doped Mn sites in perovskite NSs, in the presence of TNPs, nanotubes (TNTs), and nanorods (TNRs), under both liquid and thin film conditions. The primary objective is to assess how different TiO_2 morphologies affect electron transfer interactions with perovskite NSs and to determine the most effective quencher morphology in the liquid phase. Furthermore, the chapter examines the lifetime decay behaviour of Mn^{2+} dopants, distinguished by their surface (S-Mn) or bulk localization (B-Mn), when interfaced with TNPs, TNTs, TNRs, and TNTAs in different thin film configurations. The capability of the Mn-doped perovskite NS system to convert ultraviolet (UV) light to visible light is demonstrated through thin film luminescent concentrators. Additionally, the chapter ends by briefly exploring the change of Mn steady-state PL response under an external magnetic field, highlighting a potential path for future studies.

4.1 Objectives

This objectives of this work are

- To demonstrate the effect of synthesis parameters on Mn PL
- The interaction of Mn doped $CsPbBr_3$ with TiO_2 morphologies in liquid and thin film state by analyzing the steady state and time resolved Mn PL
- Presenting Mn-$CsPbBr_3$ based thin film luminescent concentrators as potential UV to visible down converters under a solar simulator

4.2 Experimental

4.2.1 Materials

All the materials were used as received, unless stated otherwise; Cesium Carbonate ($CsCO_3$ >99%, Sigma Aldrich), Lead Bromide ($PbBr_2$, >98%, anhydrous, Sigma Aldrich), Manganese acetate ($C4H6MnO4$, >98%, anhydrous, Thermos Fisher Scientific), Hydrobromic acid (HBr, >99.99%, Sigma Aldrich), Oleic acid (90%, Sigma Aldrich), 1-Octadecene (90%, Sigma Aldrich), Titania nanoparticles

(<25 nm, 99.7%, Sigma Aldrich), Titania nanotubes (Outer diameter 10-15 nm, inner diameter 3-5 nm, length 1μm, 99.9%, Guangzhou Hongwu Material Technology Co., Ltd) and Titania nanorods (10 nm diameter, 4μm length, Sigma Aldrich). Isopropanol, Hexane (95%, Sigma Aldrich). The TNTAs were domestically grown.

4.2.2 Synthesis of Manganese doped $CsPbBr_3$ nanosheets

Mn-$CsPbBr_3$ nanosheets were synthesized using hot injection technique, as reported by Wang et al [157]. HBr is an essential ingredient to ensure the Mn doping, the volume of HBr was also varied to ensure that analysed samples should have high Mn PLQY.

4.2.2.1 Drying of oleic acid and oleylamine ligands

Oleic acid (15 mL) and oleylamine (15 mL) were added to two separate three neck flasks, having a volume capacity of 25 mL, each. Both flasks were purged with argon and evacuated using vacuum to remove oxygen, before heating to 120°C under inert atmosphere, followed by switching to vacuum for 60 minutes to remove unwanted moisture. The dried ligands were cooled down to room temperature and stored in argon atmosphere for further use.

4.2.2.2 Cesium precursor preparation

$CsCO_3$ (0.125 g, 0.383 mmoles, weighted under argon atmosphere), oleic acid (0.451 mL, 1.41mmoles, already dried) and 4.5 mL of 1-Octadecene were mixed in a three-neck flask, it was mounted on a Schlenk line and evacuated-purged with argon three times at room temperature to ensure complete removal of oxygen. The mixture was heated to 120°C under inert atmosphere and maintained under vacuum for 1 hour, followed by heating to 150°C until it turned slightly yellowish in colour indicating complete formation of Cesium oleate. The mixture was cooled to room temperature and kept under argon atmosphere for further use.

4.2.2.3 Lead and Manganese precursor preparation

$PbBr_2$ (0.058 g, 0.158 mmoles, weighted under argon atmosphere), C4H6MnO4 (0.180 g, 1.04 mmoles, weighted under argon atmosphere), HBr (0 μL - 200 μL - 500 μL), oleic acid (0.7 mL, 2.2 mmoles, already dried), oleylamine (0.7 mL, 2.12 mmoles, already dried) and 1-octadecene (5 mL) were mixed in a 50 mL three neck flask and mounted on the Schlenk line system. The system was purged with argon and followed by evacuation. This cycle was repeated three times to make sure that oxygen is removed. The mixture was heated to 120°C under argon and maintained at this temperature for 60 minutes to remove all the moisture, and form $L_2[Pb_{1-x}Mn_x]Br_4$ complex, which would serve as an intermediate structure for Mn doped $CsPbBr_3$.

4.2.2.4 Hot Injection

The lead bromide precursor with Mn (either bromide or acetate) was switched back to argon purging, heated to 200°C and oleic acid (0.7 mL, already dried) and oleylamine (0.7 mL, already dried) were injected and allowed to mix for 10 minutes. Cesium oleate was heated to 100°C and 0.4 mL of it was taken out and injected into the lead precursor which led to instant formation of yellowish product. After 5 seconds, the reaction mixture was quenched to room temperature using an ice bath.

4.2.2.5 Cleaning process for Mn-$CsPbBr_3$ nanosheets

The as synthesized product was mixed with isopropanol in 1:5 (v: v), centrifuged at 3500 rpm for 2 minutes. The supernatant was discarded, and precipitate was dispersed in hexane for further use.

4.2.3 Preparation of Titanium dioxide (TiO_2) suspension

0.4 mg of titanium dioxide (nanoparticles, nanotubes, nanorods) was suspended in 1 mL hexane and subjected to ultrasonication for 3 hours. Later, the suspension was diluted by adding 3 mL of hexane.

4.2.4 Mn-$CsPbBr_3$ /TiO_2 nanocomposite preparation

4.2.4.1 Nanoparticles, Nanotubes and Nanorods

0.1 mL of as prepared TiO_2, nanoparticles or nanotubes, was mixed with 0.5 mL hexane and 50 µL of perovskite suspension was added to it. The suspension was kept under stirring at 500 rpm for 60 minutes. Then, 50 µL of this mixture was spin coated on a glass substrate at 2000 rpm for 15 seconds. Finally, the nanocomposite was dried using argon.

4.2.4.2 Titanium dioxide nanotube arrays

50 µL of perovskite suspension was diluted with 0.6 mL hexane. Out of this suspension, 50 µL was spin coated on the TNTAs substrate at 2000 rpm for 15 seconds, followed by drying using argon.

4.2.5 Mn-$CsPbBr_3$ /Polymethyl methacrylate (PMMA) luminescent concentrator preparation

The nanocomposites were prepared by mixing PMMA in chloroform (Trichloromethane-TCM) and stirring the mixture at 45°C for 30 minutes. The result clear solution was mixed with certain amount of perovskite nanosheets, sonicated for 30 seconds to ensure dispersion of PNCs. The nanocomposite material was spin coated on a glass substrate under 2000 rpm for 15 seconds and dried under argon.

4.2.6 Characterization techniques

4.2.6.1 Transmission Electron Microscopy (TEM) and Scanning Electron Microscopy (SEM)

TEM images of $CsPbBr_3$ PNSs were acquired on a Jeol ARM20CF NeoARMelectron microscope at 200kV acceleration voltage. The samples were prepared by drop-casting the colloidal solution on the carbon-coated TEM grids. TEM images of TiO_2 morphologies were acquired using Transmission electron microscope (CM 200, Philips) equipped with Quemesa camera (Olympus Soft Imaging Solutions). Image acquisition was done with RADIUS software. The TEM for TNTs was provided by the manufacturer. The SEM images of Mn-$CsPbBr_3$/TiO_2 systems were recorded on a Gemini SEM 300 FEG from Zeiss at an acceleration voltage of 10 kV.

4.2.6.2 UV-Visible absorption, Photoluminescent excitation, Steady state and time resolved photoluminescence and Photoluminescence Quantum Yield

UV–vis absorption spectra of $CsPbBr_3$ PNCs and TiO_2 NPs were recorded in a quartz cuvette using a Lambda 1050+UV–vis–NIR spectrometer from Perkin Elmer. Steady-state and time-resolved PL were recorded on Spectrofluorometer FS5 from Edinburg Instrument. For the steady state spectra and photoluminescence excitation scans, excitation and emission wavelengths were set at 420 nm and 615 nm, respectively. The corresponding slit sizes were 0.9 nm and 0.5 nm, respectively. For the time-resolved PL measurements, a nanosecond laser with 375 nm excitation wavelength (to analyse the perovskite B.E emission) with a slit size of 0.5 nm was used. To analyse the doped Mn emission a microsecond flashlamp with excitation wavelength set to 420 nm and emission wavelengths set to

desired wavelengths with a slit sizes of 2 nm and 1.5 nm, respectively. For each TRPL measurement, the data was recorded for a period of 90 seconds and the data acquisition was made using the technique of TCSPC. The decay profiles of $CsPbBr_3$ emission were fitted using triexponential decay function

The decay profiles of Mn emission were tail fitted using a biexponential function

$$R(t)=A_1 \exp\left(-t/\tau_1\right)+A_2 \exp\left(-t/\tau_2\right) \quad 4\text{-}1$$

and the amplitude-weighted average PL lifetime was calculated using the equation:

$$\tau_{avg}=\frac{A_1\tau_1+A_2\tau_2}{A_1+A_2} \quad 4\text{-}2$$

Also, the fractional contribution of each decay time to the steady-state intensity was calculated using the formula

$$f_i=\frac{A_i\tau_i}{A_1\tau_1+A_2\tau_2}$$

PLQYs of the $CsPbBr_3$ PNCs were measured using an absolute method by directly exciting the PNC solution as the sample and the toluene as the reference in an SC-30 integrating sphere module fitted to a Spectrofluorometer FS5 from Edinburg Instrument. During the measurement, the excitation slit was set to 3nm, and the emission slit was adjusted to obtain a signal level of 1 106cps. A wavelength step size of 0.1nm and an integration time of 0.2s were used. The calculation of absolute PL QY for the samples is based equation 3.5

For steady-state PL spectra and absolute PL QY measurements, the samples were excited at 420 nm and hexane was used as a reference.

4.3 Results and discussion

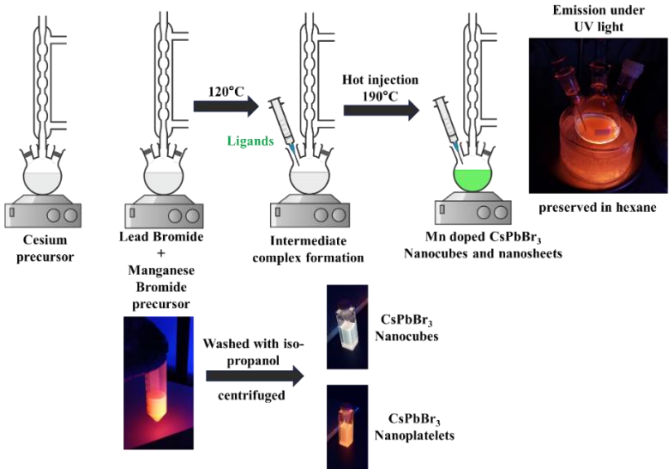

Figure 4.1) A schematic representation for Mn doped $CsPbBr_3$ synthesis using hot injection technique

We investigate the behaviour of charge carriers in manganese doped $CsPbBr_3$ nanosheets and analyse if the morphology of a quencher (TiO_2) has any impact on the rate of electron transfer from the perovskite. We employed Manganese Acetate as Mn source for the hot injection technique to synthesize the $CsPbBr_3$ nanosheets with doped Mn and washed them using isopropanol. It has been mentioned repeatedly in the literature that acetone could be used to clean the unreacted material out, however, for our work, it was more compromising for Mn PLQY as compared to the isopropanol. Figure 4.1 shows the schematic of the synthesis and washing process. All the analysis were done in hexane, as it was

observed that the Mn emission was quenched if preserved in toluene, possibly due to relatively higher polarity (0.099 as compared to 0.009 for hexane [158]).

During the synthesis process, as the lead and manganese precursors are heated to 120°C and kept under vacuum for 1 hour, along with OA, OLAm and HBr, an intermediate complex forms. This intermediate complex is $L_2[Pb_{1-x}Mn_x]Br_4$ and serves as the seed for the formation of Mn doped CsPbBr3 nanosheets. This complex also luminescence under UV light with orange emission which is typical of Mn. The literature shows the absorption of this luminescence to be around 395 nm, while the emission is reported to be at 610 nm [159] Figure 4.6. Furthermore, the TRPL lifetime of this complex is around 110-120 ms. After the hot injection, this complex serves as a seed for the Mn doped $CsPbBr_3$ nanosheets. However, the issues lie with the incomplete reaction, therefore, some of this complex remains unconsumed. As discussed in the experimental section, the perovskite material is washed with isopropanol, instead of conventional centrifugation in toluene because of the reason that toluene is unable to remove this complex, and it comes out in the precipitate along with the material. Different centrifuge speeds do not play any role in separation of desired material from the unreacted complex. Nevertheless, a limited quantity of unreacted complex survives the washing process with iso-propanol.

4.3.1 Morphology of Mn doped $CsPbBr_3$ perovskite

The post washed reaction mixture was centrifuged twice to separate out the nanocubes and nanosheets. The nanocubes remain suspended in the supernatant and nanosheets precipitate. The analysis was carried by drop casting the suspension of different morphologies on a carbon coated girds. Figure 4.2 shows TEM images of Mn doped $CsPbBr_3$ nanocubes and nanosheets.

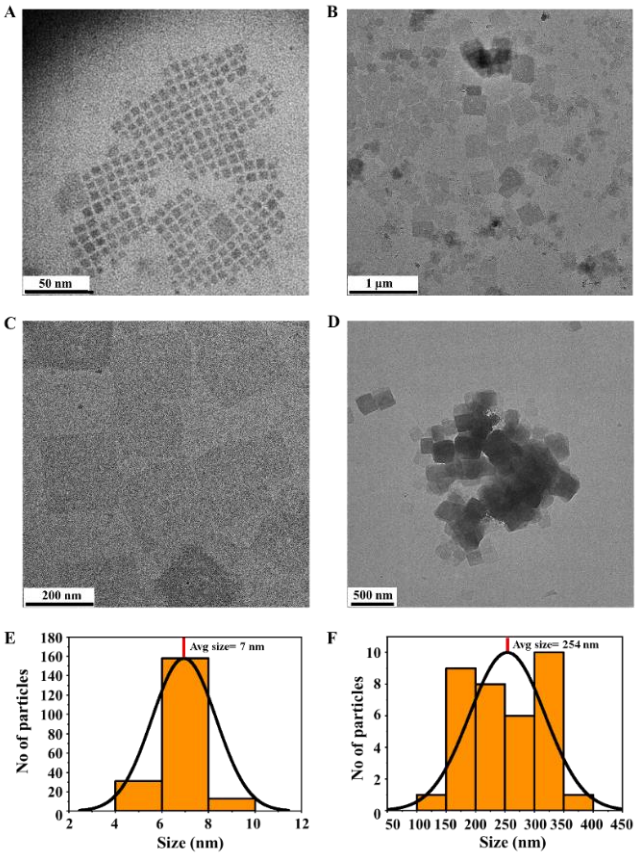

Figure 4.2) TEM images of Mn doped (A) $CsPbBr_3$ PNCs, (B-D) nanosheets, (E) Average size of nanocubes and (F) nanosheets

The nanocubes have an average size of 6.9 nm, whereas the square shaped nanosheets have an average side estimated to be around 254 nm. The size of all the nanostructures was calculated using ImageJ

software and average was based on gaussian distribution plotted using origin software. Thickness of the sheets will be discussed in the next section.

4.3.2 Optical properties of Mn doped $CsPbBr_3$ nanosheets

The parameters for analysis of Mn doped $CsPbBr_3$ are set such that the unreacted complex should not get excited energetically, hence, the obtained results should only demonstrate the effect of desired excited material. Manganese is well known for its orange emission centered around 610-620 nm[160], this peak position can vary depending upon the position of the Mn energy states in the bandgap of the perovskite material. Here, it is crucial to mention that amount of HBr has been reported as the main driving force behind the doping of Mn in the lattice of $CsPbBr_3$[157], [159]. Figure 4.3 below shows the effect of using different amounts of HBr for the synthesis

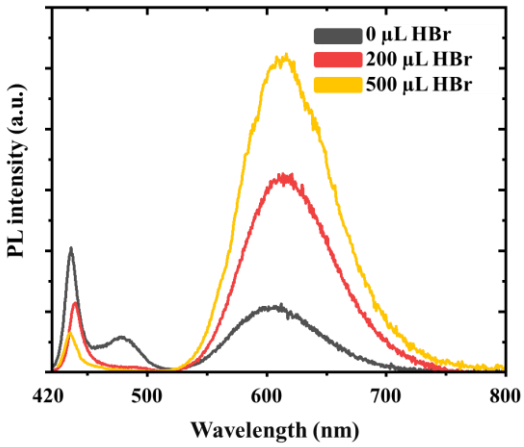

Figure 4.3) Mn doped $CsPbBr_3$ nanosheets synthesized using different amounts of HBr

By increasing the amount of HBr, more amount of Mn is doped in the lattice of $CsPbBr_3$. This comes at the cost of B.E recombination, because the excited carrier in the lattice of the host undergoes energy transfer to the Mn atoms. Hence an inverse relationship is established between the B.E and Mn PL intensity. The Mn PL increases with amount of HBr used during the synthesis, we limit our analysis to 500 µL because the reaction becomes unstable at 600 µL HBr and onwards due to its volatile behaviour at high temperature.

The EDS analysis shows a manganese presence of 3.5 % ± 0.3% (Figure 4.4).

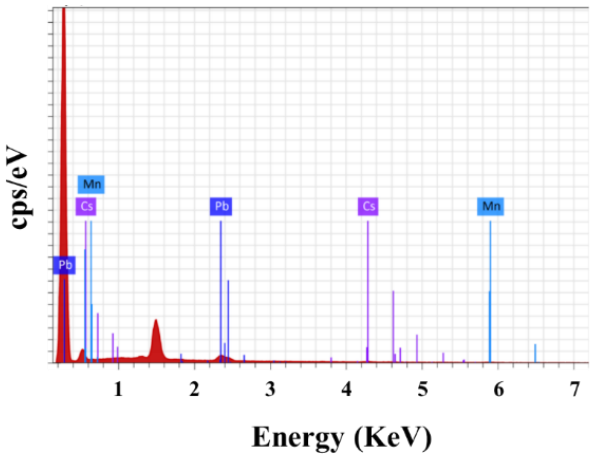

Figure 4.4) EDS spectra for Mn-$CsPbBr_3$ perovskite nanosheets

The Figure 4.5 shows the UV-visible absorption and PL spectra of the Mn doped perovskites.

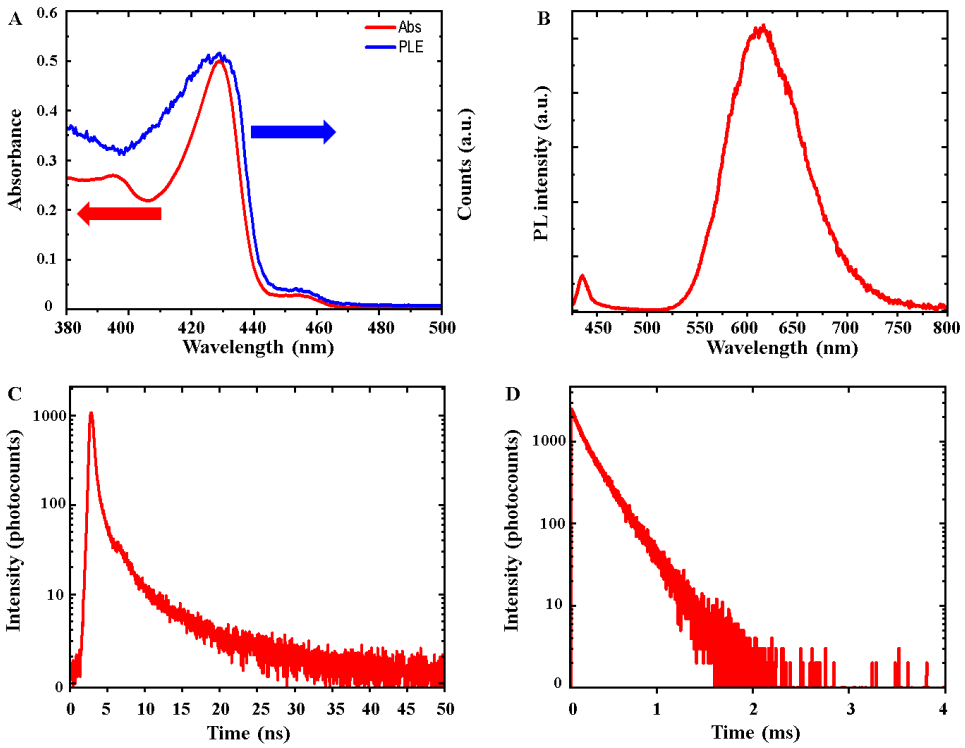

Figure 4.5) Optical analysis of Mn doped $CsPbBr_3$ A) UV-Visible absorption and PLE spectra for 615 nm PL emission, B) PL emission spectra-excited at 420 nm, C) TRPL of 435.5 nm PL peak corresponding to $CsPbBr_3$ B.E recombination and D) TRPL for Mn emission at 615 nm

The Mn-doped $CsPbBr_3$ nanosheets exhibit an absorption peak centered at 429-430 nm. PL emission spectra reveal two distinct peaks at 435.5 nm and 615 nm. Based on literature correlations with absorption peak positions, the nanosheet thickness is estimated to be approximately 2 nm [161].

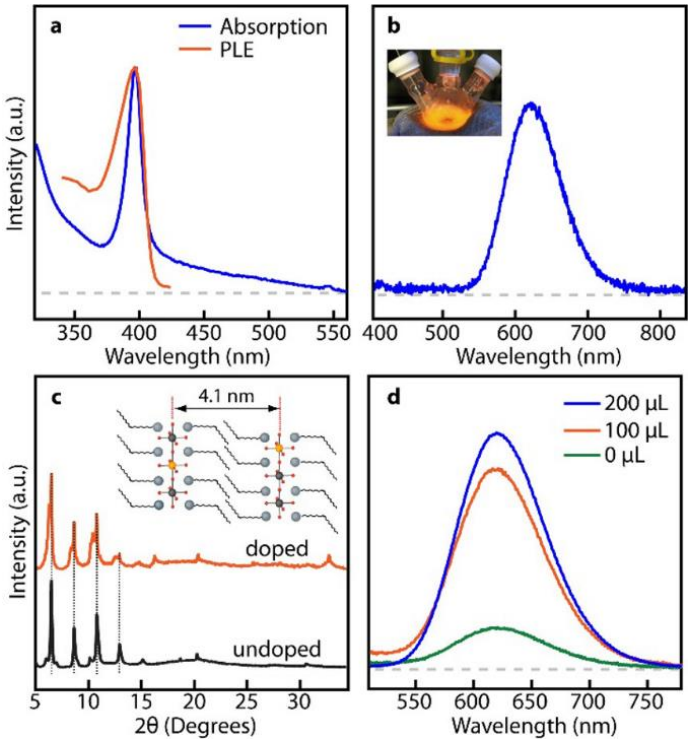

Figure 4.6) Optical and structural characterizations of intermediate complex, copied from [162]

The emission peak at 435.5 nm is attributed to the band-edge recombination of the $CsPbBr_3$ nanosheets. According to literature, the position of this peak is influenced by the choice of Mn precursor. When manganese bromide is used, the peak typically appears at 434 nm [150], , whereas with manganese acetate, it is generally observed at 436 nm [152] . In our study, the use of manganese acetate as the Mn precursor resulted in a peak at 435.5 nm. However, varying the volume of HBr acid to 100µL led to a shift of the band-edge emission to 436-437 nm. Notably, the position of Mn^{2+} emission at 615 nm remains unaffected by changes in HBr concentration. The slight shift in the band-edge emission peak of $CsPbBr_3$ is likely associated with variations in the nanosheet thickness. Figure 4.6 presents the optical and structural characterization of the intermediate complex, as reported by Parobek et al [159]

As discussed above, the 'intermediate complex' formed during the synthesis also gives PL emission at 610 nm, which could be confused with the Mn doped $CsPbBr_3$ emission at 615 nm. Therefore, to verify that the emission peak in the PL spectra at 615 nm is a consequence of the Mn doping in the $CsPbBr_3$, we employed the photoluminescence excitation scan (PLE). For this purpose, excitation wavelength was set to 615 nm, and the sample was scanned from 380 nm to 630 nm. This was done to investigate the excitation wavelength of the charge carriers which give PL at 615 nm. The figure shows PLE spectra with the peak centered at 429-430 nm, and least contribution from 396 nm, confirming that the charge carriers recombining through the Mn energy state at 615 nm are originating from 429-430 nm, which is the same as the absorption peak position of $CsPbBr_3$ nanosheets. Figure 4.7 gives an overview of possible internal dynamics related to charge or energy transfer mechanism, and Mn PL emission.

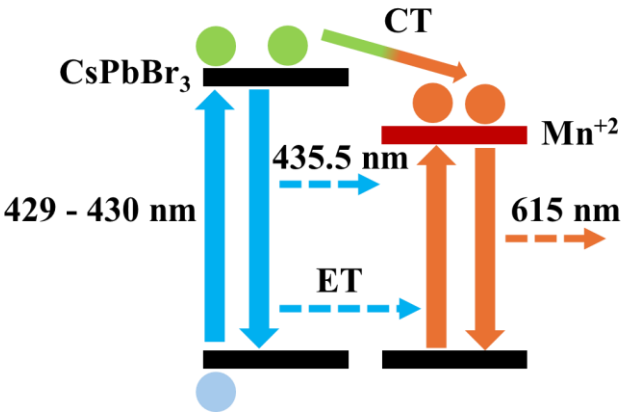

Figure 4.7) Internal mechanism of Mn doped $CsPbBr_3$ nanosheets.

Once the doping of Mn was confirmed, the PL QY of radiative emissions of $CsPbBr_3$ B.E (B.E) recombination and manganese relaxation were calculated. The Mn-$CsPbBr_3$ was excited at 420 nm, and PL QY of 1% and 29% were recorded for B.E recombination and Mn relaxation, respectively, as shown in the Figure 4.8

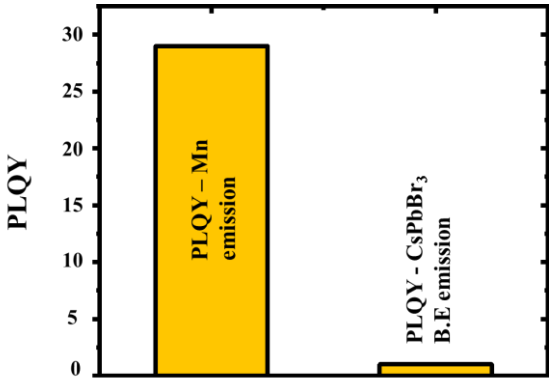

Figure 4.8) PLQY of Mn emission and $CsPbBr_3$ B.E recombination. The maximum deviation for the system is < 2%.

The lifetime of the charge carriers for the PL emission at 435.5 nm and 615 nm were analysed using a nanosecond laser (B.E recombination) and a microsecond flashlamp (for Mn relaxation). The lifetime of $CsPbBr_3$ was fitted using convolution fit, whereas for Mn emission, tail fitting was utilized. The results are summarized in Table 4.1

Table 4.1) Lifetime components and their relative contributions

	τ_1	f_1	τ_2	f_2	τ_3	f_3	χ^2	τ Avg
$CsPbBr_3$ B.E (435.5 nm)	0.29 ns ± 0.001	0.6	1.68 ns ± 0.06	0.20	6.2 ± 0.3	0.19	0.999	0.44 ns
Mn-$CsPbBr_3$ (615 nm)	96 µs ± 1.3	0.39	257 µs ± 2.0	0.61	-	-	0.998	156 µs

The Mn lifetime shows two components, τ_1 = 96 µs and τ_1 = 257 µs, and the τ_{avg} comes out to be 156 µs. It has been shown in the literature that the surface manganese has a shorter lifetime as compared to the Mn atoms residing in the lattice[163]. Nevertheless, the surface Mn still shows longer radiative lifetime compared to the pristine perovskite material. As evident from the PL emission, Mn trap states exist at lower energy level compared to the CBE of $CsPbBr_3$. Also, the Mn doped on the surface exists at lower energy compared to the bulk doped Mn atoms [163], [164]. Based on these conditions, the charge carriers should be available on the surface of Mn-$CsPbBr_3$ for photocatalytic applications. However, due to unstable nature of perovskites and intrinsically favourable nature TiO_2 towards photo catalytic activity, the logically consistent decision is to retain TiO_2 as charge acceptor from the perovskite systems. To the best of our literature review, the interaction of Mn doped $CsPbBr_3$ with TiO_2 is not widely investigated and until present, only single study reported by Du et al [165] has emerged, it focuses on studying the transient dynamic processes in $CsPbBr_3/TiO_2$ as a function of post synthesis Mn^{+2} doping content in $CsPbBr_3$ nanocubes. The $CsPbBr_3$ nanocubes showed no d-d transition assisted Mn emission, possibly due to the adopted doping technique. In this case, we base our analysis on the steady state and time resolved response of Mn emission.

4.3.3 Interaction of Mn doped $CsPbBr_3$ perovskite with TiO_2

To understand the charge carrier dynamics of Mn-$CsPbBr_3/TiO_2$ and its dependency on the morphology of the quencher, we first need to understand the possible under lying mechanisms. Therefore, we start by employ the steady state and time resolved PL. The morphologies of TiO_2 used for this analysis are shown in Figure 4.9

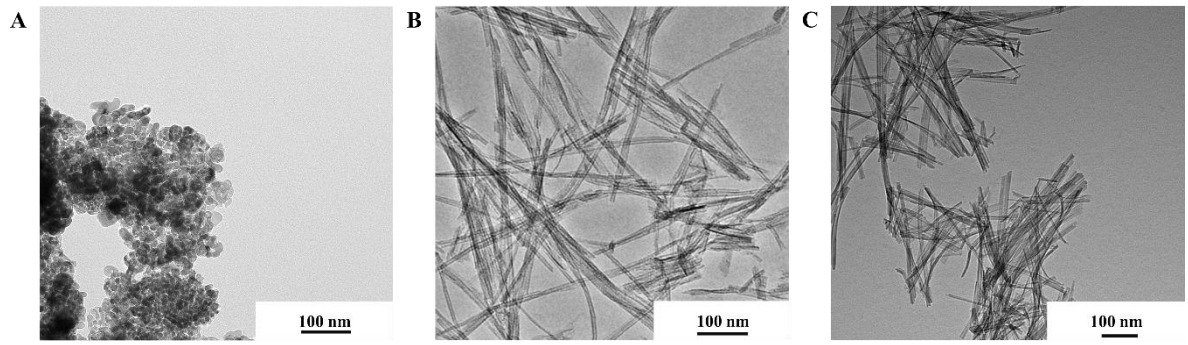

Figure 4.9) (A) TNPs (size <25 nm), (B) TNTs (outer diameter 10-15 nm, inner diameter 3-5 nm, length 1µm) and (C) TiO_2 nanorods (TNRs, diameter 10 nm, length < 4µm)

4.3.3.1 Steady state PL spectra in liquid phase and Stern-Volmer analysis

First, the interaction in liquid phase was analysed by suspending Mn-$CsPbBr_3$ nanosheets in 2mL hexane, in quartz glass vial. To this, already prepared TiO_2 suspensions (of nanoparticles and nanotubes) were added in a stepwise manner. The corresponding steady state spectra were recorded, for the increasing concentration of TiO_2, from 0µM to 417 µM, as shown in the Figure 4.10 . The dilution correction was applied using the procedure described in section 3.3.5.1.1 and is demonstrated in Figure 4.11

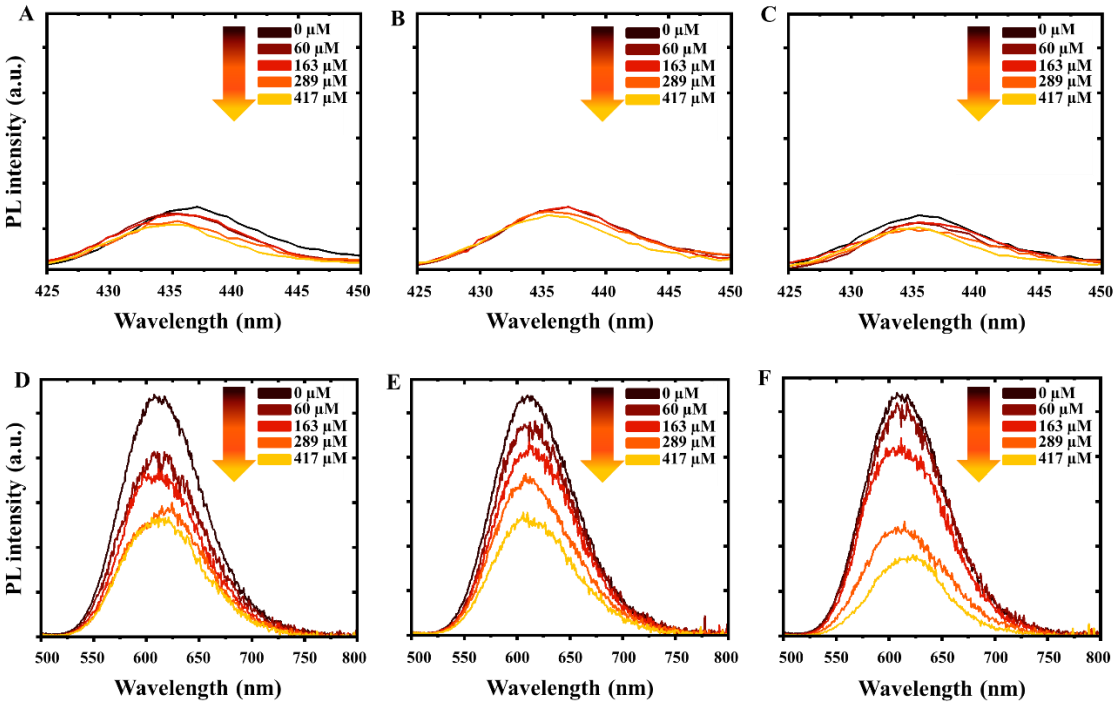

Figure 4.10) (A-C) PL spectra of $CsPbBr_3$ B.E recombination and (D-F) PL spectra of Mn emission after exposure to (A,D) TNPs (B,E) TNTs and (C,F) TNR

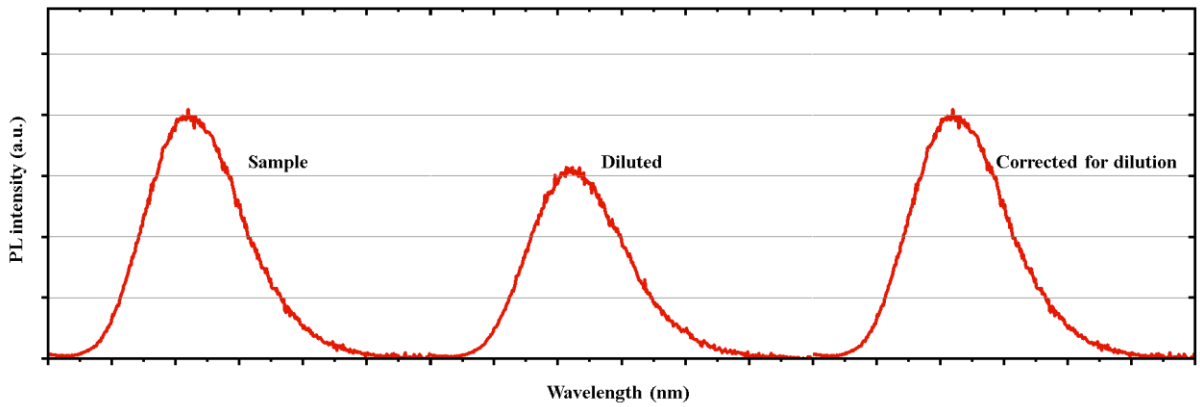

Figure 4.11) Demonstration of dilution correction for Mn-$CsPbBr_3$ perovskite

As evident from the Figure 4.10, TNPs show higher quenching of PL for the initial lower concentrations of the quencher. This could be due to higher surface area of TNPs, allowing for a better contact to the surface of quencher. As the concentration increases, the decrease in PL intensity is not significant. On the other hand, TNTs appear to cause a steady decrease in PL spectra as the concentration is increased. Finally, TNRs show least decrease in PL spectra at low concentration, however, upon introducing the system to higher concentration of quencher, the PL is drastically quenched. The distinct behaviours of Mn emission under the influence of different concentration of TiO_2 morphologies depicts a morphology

driven PL quenching phenomenon. To develop in depth understanding of these results, we start by analyzing the Stern-Volmer (S-V) plot, shown in Figure 4.12

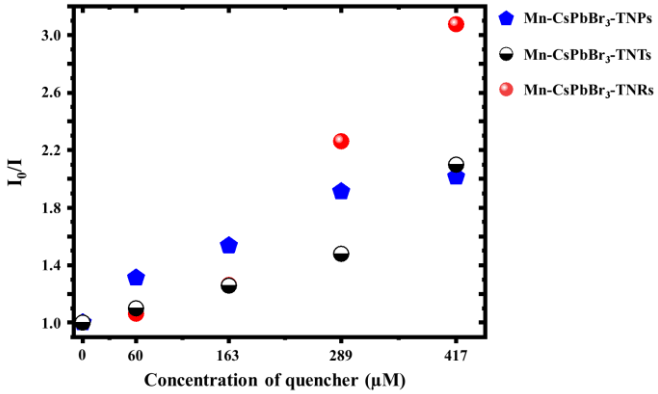

Figure 4.12) Stern-Volmer plots for Mn-CsPbBr3 PNC colloidal solutions in the presence of different morphologies of TiO_2 as quencher.

We can observe in the S-V plot that TNPs, TNTs and TNRs show similar trend at a lower concentration, with TNPs showing higher magnitude of quenching. This is followed by identical trend and quenching intensity of TNTs and TNRs. Since the morphological nature of TNTs and TNRs is more identical as compared to the TNPs, we can expect similar performance. All the three morphologies show linear behaviour at lower concentrations. This is well expected and widely reported in the literature that low concentrations regimes are dominated by static quenching and upon increasing the concentration of the quencher, dynamic quenching comes into play. Here, we can observe the dynamic quenching starting to appear at for TNRs at 289 µM. Whereas the TNPs and TNTs seems to show static quenching even at higher concentrations. This gives us first indication of how morphologies of TiO_2 can have an impact on the quenching mechanism, even at similar concentrations. The proposed mechanism is shown in Figure 4.13

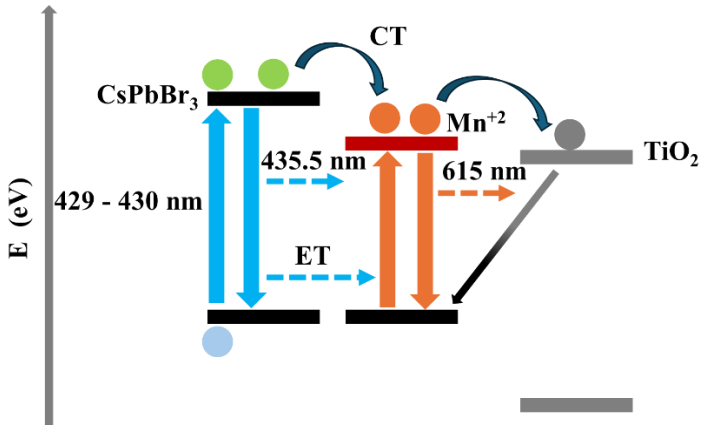

Figure 4.13) Proposed mechanism in perovskite/TiO_2 system

4.3.3.2 Deconvolution of steady state PL spectra

As discussed earlier, the Mn dopants existing on the surface of nanostructures exhibit shorter lifetimes and broadened PL spectrum, in contrast to Mn atoms doped in the bulk of the lattice. Therefore, by using gaussian function to deconvolute the PL peak appearing at 615 nm, we can obtain the component peaks. The wavelength position of these component peaks can set a reference point for further analysis. Furthermore, by observing the behaviour of the component peaks after exposure to varying concentrations of TiO_2, we can determine the effect of different morphologies. Figure 4.14 shows the deconvoluted spectra, corresponding to the 289 µM concentration of TiO_2.

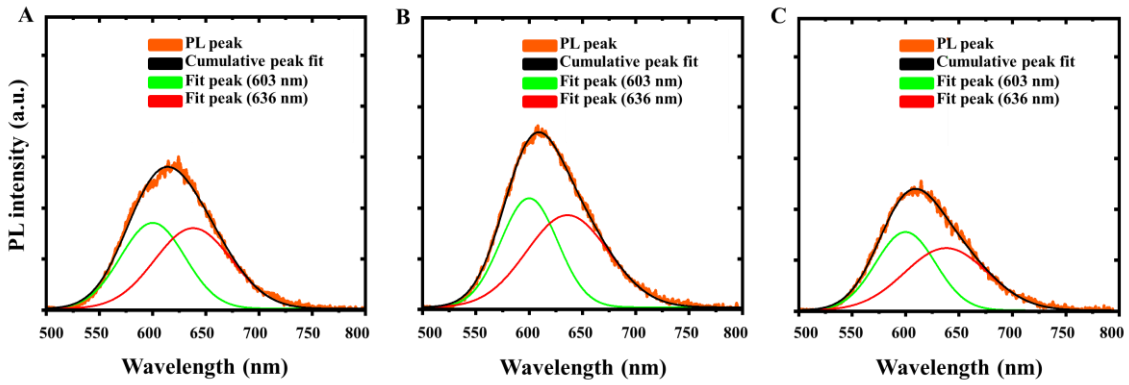

Figure 4.14) (A, B, C) Deconvolution of Mn PL emission peak (615 nm) after exposure to 289 µM of (A) TNPs, (B)TNTs and (C) TNRs

The PL peak at 615 nm splits into two peaks, one at 600 nm and the second one is centered at 636 nm. As evident from the figures, the PL peak at 636 nm for all the cases exhibits broadened nature as compared to the 600 nm peak. Therefore, we can confirm that the Mn doped on the surface of $CsPbBr_3$ nanosheets emits at higher wavelength as compared to the Mn atoms doped in the bulk of the lattice.

In reference to the Figure 4.13, the charge carrier trapped in the bulk lattice Mn only recombine by either radiative or non-radiative recombination, therefore, the possibility of charge transfer from Mn states to the TiO_2 can only be attributed to the surface Mn atoms. Therefore, introduction of TiO_2 to the perovskite suspension should have a direct impact on the PL contribution coming from S-Mn. This impact can be quantified by integrating the area under the PL peak and analyzing the variation with respect to change in concentration of the TiO_2. The Figure 4.14 shows the change in area under the peaks against concentration of TiO_2.

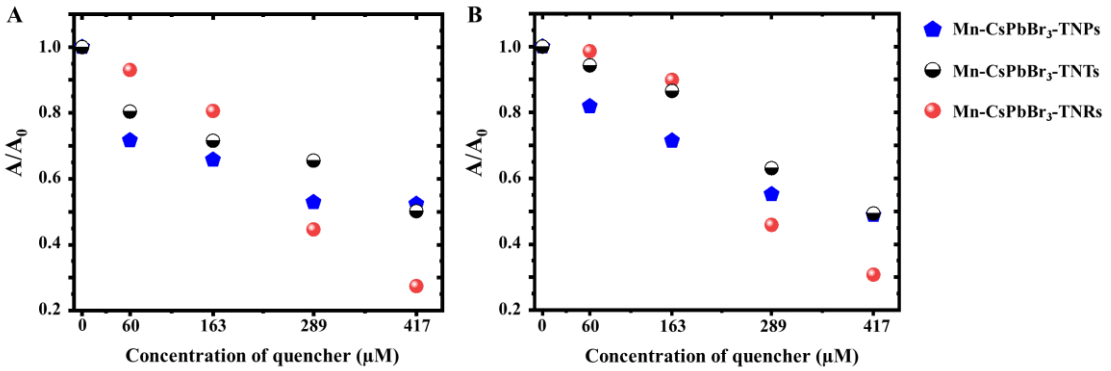

Figure 4.15) The relative contribution of area under the deconvoluted peaks (A) 600 nm and (B) 636 nm, plotted as a function of TiO_2 concentration

Interestingly, it can be observed that B-Mn, as well as S-Mn show decrease in contribution towards radiative emission, with increasing TiO_2 concentration. The decreasing trend is also the same for all the morphologies indicating that the difference lies mainly in the magnitude of quenching in comparison to the mechanism of quenching. As shown in Figure 4.13, the B-Mn charge carriers are trapped in low energy states and hence cannot be transferred to the quencher by any possible mechanism. Therefore, this decrease in B-Mn emission could only be explained by in depth analysis of the charge/energy transfer from $CsPbBr_3$ lattice to the Mn atoms.

4.3.3.3 Internal dynamics of Mn doped $CsPbBr_3$-TiO_2 heterostructures and their PLQY

As shown in the Figure 4.7 , at 0µM concentration of quencher, the absorption at 429-430 nm leads to excitation of carriers, resulting in formation of excitons. These charge carriers initially undergo

thermalization with the lattice until they attain the energy level of conduction band minima of the $CsPbBr_3$. At this energy level, the charge carriers have three possible routes to follow, which are as following

i. To under radiative recombination (K_r), resulting in a B.E recombination and PL emission at 435.5 nm
ii. To undergo non-radiative recombination (K_{nr}) through the trap states and produce no PL emission
iii. To undergo energy/electron transfer from $CsPbBr_3$ to Mn doped atoms (K_{ET})

Here, the efficiency of energy transfer ($\boldsymbol{\Phi}_{ET}$) from perovskite lattice to Mn atoms is given by the formula

$$\boldsymbol{\Phi}_{ET} = \frac{K_{ET}}{K_{ET} + K_r + K_{nr}} \quad 4\text{-}3$$

Here K_{ET} is picosecond process and hence occurs at a scale much faster than the nanosecond process of K_r or K_{nr}. As evident from table 1, fast lifetime component of 130 ps dominates average lifetime of Mn-$CsPbBr_3$ nanosheets with a relative contribution calculated to be 81%. The other two lifetime components of 790 ps and 11.8 ns also appear, showing a relative contribution of 14% and 5 percent, respectively. The latter two components correspond to non-radiative and radiative recombination of charge carriers, respectively. The 130 ps lifetime aligns with the reported values for energy transfer from $CsPbBr_3$ to Mn atoms, demonstrating high relative contribution reveals high magnitude of energy transfer.

Once the energy transfer process occurs, the carriers are found to be residing in the excited states of the doped Mn atoms. At this point, charge carriers have further two possible routes

i. To undergo radiative recombination from Mn excited state to $CsPbBr_3$ ground state and give Mn emission (K_r^{Mn})
ii. To undergo non radiative recombination and no emission is produced (K_{nr}^{Mn})

The sum of K_r^{Mn} and K_{nr}^{Mn} constitute the internal PLQY of Mn atom ($PLQY_{int}^{Mn}$), according to equation

$$PLQY_{int}^{Mn} = \frac{K_r^{Mn}}{K_r^{Mn} + K_{nr}^{Mn}} \quad 4\text{-}4$$

And finally, the total $PLQY_{Mn}$ is defined as

$$PLQY_{Mn} = \boldsymbol{\Phi}_{ET}.PLQY_{Int}^{Mn} \quad 4\text{-}5$$

Here, it should be noted that we take the $PLQY_{int}^{Mn}$ as an overall sum of B-Mn and S-Mn. In view of above equations 4-3, 4-4 and 4-5, it can be concluded that PLQY of Mn doped in $CsPbBr_3$ is driven by efficient energy transfer from perovskite lattice to Mn atoms and the internal PLQY of Mn atoms. Since, we have a 2D nanostructured perovskite, the charge carrier recombination at B.E is a fast process. We demonstrated in the previous chapter that the charge transfer from perovskite nanocubes lattice to a quencher in liquid phase is efficient with short chain ligands. In this case, the nanosheets can offer better planar contact, which might or might not lead to charge transfer from $CsPbBr_3$ lattice to TiO_2. Based on the PL spectra shown in Figure 4.10 (A-C), the addition of TiO_2 has insignificant effect on the B.E recombination of $CsPbBr_3$. Consequently, we can anticipate that $\boldsymbol{\Phi}_{ET}$ remains significantly unaffected by the addition of a quencher. Furthermore, it has been reported by Dai et al [164] that $\boldsymbol{\Phi}_{ET}$ is affected by the percentage of doping content, and which in our case remains constant. Hence, the change $PLQY_{Mn}$ is a direct consequence of variation in either K_r^{Mn}, K_{nr}^{Mn} or both.

Here, we must consider two scenarios upon addition of TiO_2, (i) if the K_r^{Mn} decrease with addition of the quencher, then $PLQY_{Mn}$ should decrease and subsequently, the $PLQY_{Int}^{Mn}$ diminishes, (ii) if the K_{nr}^{Mn} decreases, then $PLQY_{Mn}$ should increase according to equation 2, and the $PLQY_{int}^{Mn}$ value should surge. As evident from Figure 4.16, the recorded values of $PLQY_{Mn}$ decrease with increasing concentration of TiO_2.

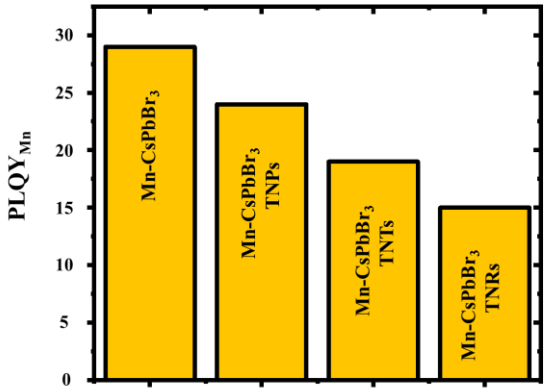

Figure 4.16) The Mn-PLQY after exposure to 417 µM of different morphologies of TiO_2. The maximum deviation for the system is < 2%.

This indicates that the rate of radiative recombination of excited charge carriers trapped in the Mn states have reduced. We associate this decrease in $PLQY_{int}^{Mn}$ to the charge transfer from surface Mn energy states to TiO_2, as evident from decrease in surface contribution in figure 48. On the other hand, the decrease in the B-Mn emission could be explained by opening of new quenching channels for charge carriers by TiO_2. At 0µM TiO_2 concentration, the charge carriers in Mn states recombine slowly, hence the channel of recombination is 'choked' and intrinsic trap states other than Mn are also saturated. Now as the concentration of TiO_2 increases, the charge transfer process starts to buildup, and it starts to compete with the existing channels of Mn recombination. Due to fast nature of charge transfer and recombination in TiO_2, the surface Mn states are 'unclogged', hence increasing number of carriers should start moving through these decay channels. As $\mathbf{\Phi_{ET}}$ remains unchanged, relative rate of energy transfer to S-Mn increases and to B-Mn decreases. The charge carriers in S-Mn have less K_r^{Mn}, hence the S-Mn PL contribution decreases as and the overall relative contribution of B-Mn should also decrease. Following this assumption, at 615 nm, the lifetime of both the surface and bulk states of Mn should decrease considerably, in addition to decrease in the relative contribution of PL for S-Mn and, on the contrary, increase for B-Mn. This is because of the reason that B-Mn energy states still prefer to retain the radiative recombination of charge carriers and using a microsecond flash lamp, we can only observe the radiative recombination of charge carriers. In view of this discussion, the average lifetime of the Mn-$CsPbBr_3$ should decrease upon exposure to TiO_2. This is discussed in the upcoming section.

4.3.3.4 Time resolved PL spectra in liquid phase

To further confirm these assumptions, TRPL lifetimes were recorded at 600 nm, 615 nm and 636 nm for the 417µM concentration, as shown Figure 4.17 below. The choice of wavelengths is based on the position of the peaks appearing after the deconvolution of Mn emission at 615 nm.

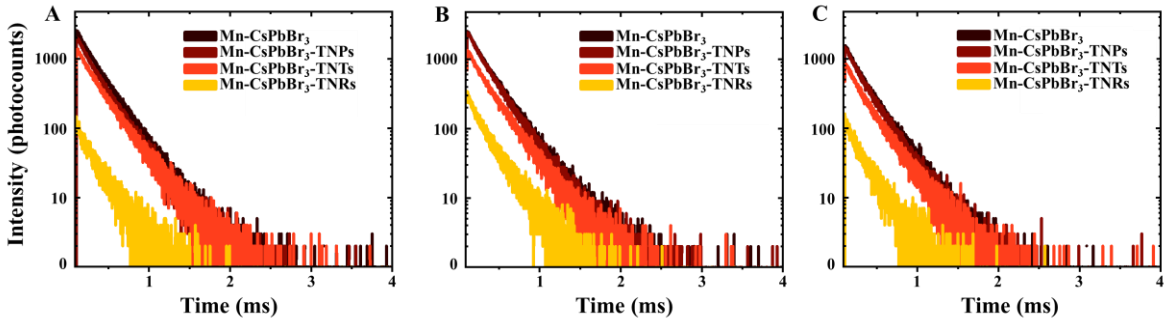

Figure 4.17) (A, B,C) The TRPL of Mn PL emission after exposure to 417 µM concentration of different morphologies of TiO_2 at (A) 600 nm, (B) 615 nm and (C) 636 nm

Figure 4.17B (615 nm) serves as an average of overall lifetime of the Mn-$CsPbBr_3$-TiO_2 heterostructures. A strong contrast can be observed between the lifetimes of samples having TNPs,

TNTs and TNRs as the quencher. Initially, we tried to fit the curves with mono-exponential decay function, which produced a fit with considerably high values for the residual, as shown in Figure 4.18.

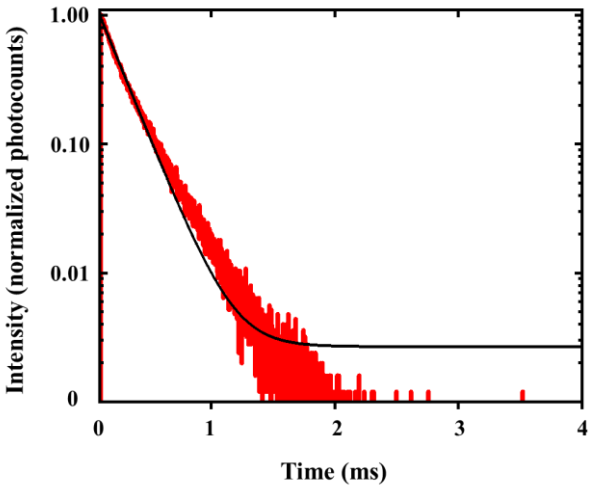

Figure 4.18) Fitting of Mn PL emission peak (615 nm) of Mn-$CsPbBr_3$. The spectra cannot be fitted with monoexponential decay fitting

This in a sense confirms that there exist more than one decay channels, in the range of microseconds. As the non-radiative recombination of charge carriers occurs in the range of picoseconds and nanoseconds, two different decay channels in microsecond range can only be attributed to the different position of Mn doping. This is further confirmed by Dei et al [163], where they showed that Mn atoms under different environment (surface or bulk) show different lifetimes. The B-Mn atoms are isolated and hence show longer lifetime compared to the surface atoms which might suffer from symmetry break and dangling bonds.

To study the distinct behaviour of the samples, the lifetimes were fitted with bi-exponential decay functions, and the corresponding components and their relative contributions shown in Table 4.2 and plotted in the Figure 4.19

Table 4.2) Lifetime components and their relative contributions, corresponding to Figure 4.17

600 nm						
	τ_1 (µs)	**f_1**	**τ_2 (µs)**	**f_2**	**χ^2**	**τ_{Avg} (µs)**
Mn-$CsPbBr_3$	208 ± 5	0.73	392 ± 35	0.27	0.996	238
Mn-$CsPbBr_3$ /TNPs	161 ± 4.8	0.49	292 ± 9	0.51	0.998	208
Mn-$CsPbBr_3$ /TNTs	192 ± 5	0.65	349 ± 19	0.35	0.997	228
Mn-$CsPbBr_3$ /TNRs	71 ± 6	0.24	248 ± 5	0.76	0.974	156

615 nm						
	τ_1 (µs)	**f_1**	**τ_2 (µs)**	**f_2**	**χ^2**	**τ_{Avg} (µs)**
Mn-$CsPbBr_3$	186 ± 8	0.56	337 ±21	0.44	0.995	231
Mn-$CsPbBr_3$ /TNPs	157 ± 4.7	0.46	286 ± 7.4	0.54	0.998	209

$Mn\text{-}CsPbBr_3$ /TNTs	172 ± 6	0.51	314 ± 12	0.49	0.997	221
$Mn\text{-}CsPbBr_3$ /TNRs	91 ± 3	0.34	262 ± 4	0.66	0.991	160

636 nm

	τ_1 (µs)	f_1	τ_2 (µs)	f_2	χ^2	τ_{Avg} (µs)
$Mn\text{-}CsPbBr_3$	152 ± 8	0.39	303 ± 11	0.61	0.994	219
$Mn\text{-}CsPbBr_3$ /TNPs	142 ± 4.4	0.41	274 ± 6	0.59	0.998	198
$Mn\text{-}CsPbBr_3$ /TNTs	172 ± 5	0.59	331 ± 16	0.41	0.996	214
$Mn\text{-}CsPbBr_3$ /TNRs	68 ± 4	0.33	239 ± 4	0.67	0.98	132

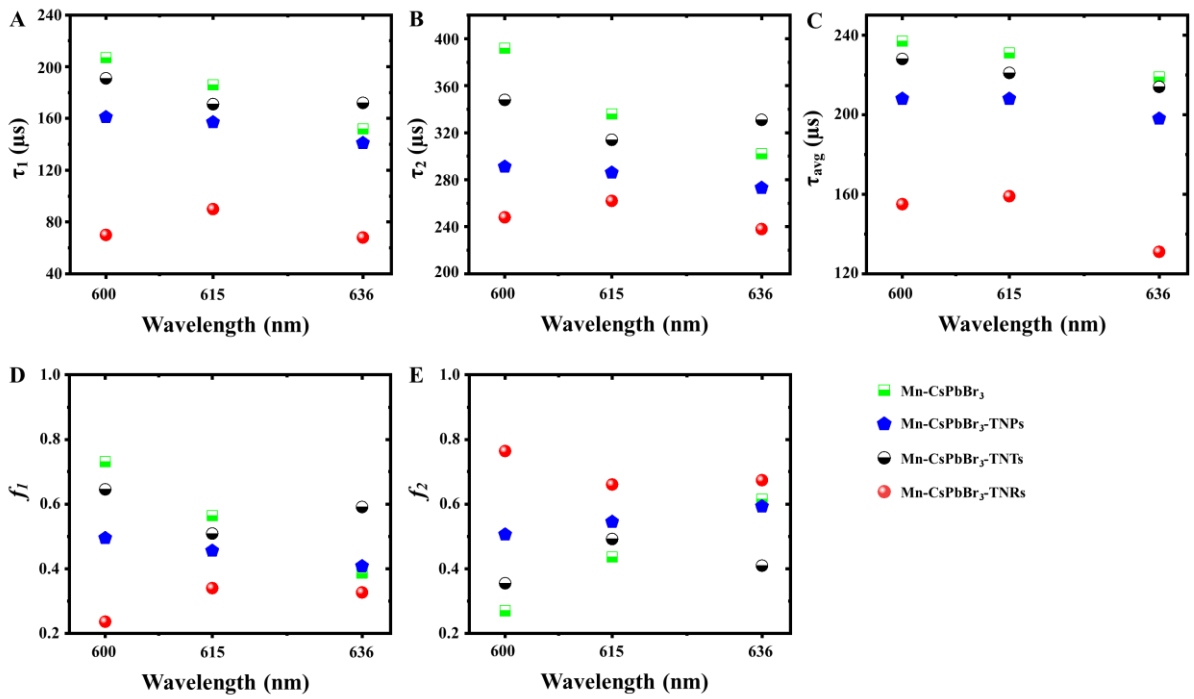

Figure 4.19) (A-E) TRPL analysis for Mn PL emission peak of $Mn\text{-}CsPbBr_3$ after exposure to 417 µM TiO_2 and the obtained lifetime components (A) τ_1 , (B) τ_2 , their corresponding relative contributions (D and E), respectively. The average lifetime is shown in (C) τ_{avg}. The TRPL readings were taken at 600 nm, 615 nm and 600 nm.

Figure 4.19A and Figure 4.19B show the values for τ_1 and τ_2 and Figure 4.19C, D show their corresponding values for relative contribution towards the PL. As we move from lower to higher wavelength region, the lifetime components of $Mn\text{-}CsPbBr_3$ show a decrease in value. This is in line with our assumption that shorter lifetimes are shown by surface Mn at higher wavelengths. Both the lifetime components show change in magnitude as the TiO_2 is introduced to the system, depicting an interaction between the Mn states and the quencher. The surface and bulk lifetime components, τ_1 and τ_2, respectively, both appear across all three set of wavelengths. This could also be verified from overlapping of the two deconvoluted peaks. To resolve this issue, we based our analysis on the

wavelength corresponding to the average lifetime of the Mn-$CsPbBr_3$/TiO_2 systems, i.e. 615 nm. Both, τ_1 and τ_2 show decrease in value upon interacting with TiO_2 at 615 nm. In parallel, the relative contribution for τ_1 decreases and for τ_2 increases. These results are exactly in line with our pervious explanation related charge carrier dynamics for Mn doped $CsPbBr_3$. Figure 4.19 C shows that average lifetime of Mn-$CsPbBr_3$ nanostructures decreases as TiO_2 is added to the system. Furthermore, it is also evident that TNRs show the best dynamic quenching efficiency as compared to the other two morphologies. TNPs and TNT show a slight decrease in average lifetime, which interestingly gives an idea of very slight dynamic quenching not strongly evident from the SV plot.

4.3.3.5 Time resolved PL spectra in thin film phase

To understand the charge carrier dynamics in Mn doped $CsPbBr_3$, it is also essential to understand the type of type of medium the nanostructures are experiencing. In liquid phase, the charge transport is limited due to isolated nature of nanostructures, the carriers are strongly confined and have preferably radiative recombination decay due to passivated surface and less trap states. In addition, the interparticle coupling is significantly low, and hence the charge carrier separation is not efficient. On the other hand, thin film phase allows for close packing of nanostructures, which enables relatively better carrier mobility (charge carrier hopping), reduced confinement and more delocalized excitons (possibility to dissociate into free carriers), ligand desorption leading to preferably non-radiative recombination and stronger interparticle interaction and hence better charge carrier separation and transport. Therefore, investigation of thin film phase can unveil new phenomena.

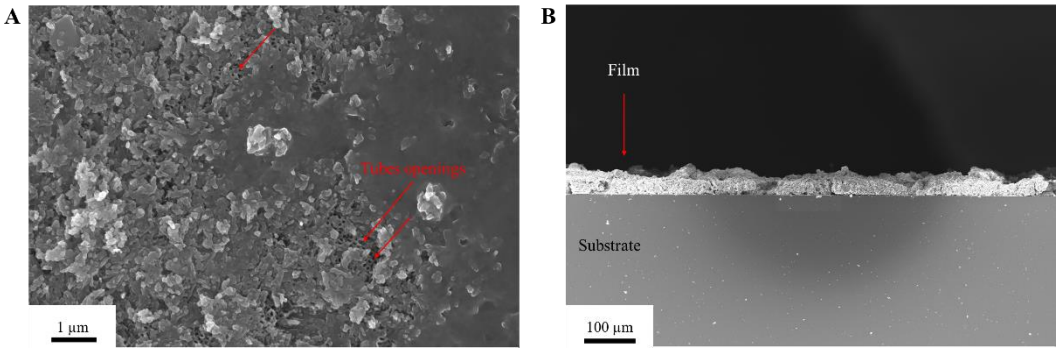

Figure 4.20) (A) Mn-$CsPbBr_3$/TNTAs (tubes openings can be seen among the covered surface) and (B) Mn-$CsPbBr_3$/TNPs (cross section), in layered and mixed configurations, respectively

To this purpose, we develop thin films of Mn-$CsPbBr_3$ and study their interaction with different morphologies of with TiO_2 under two different configurations, which are

i. Layered configuration (Layer by layer): A Mn-$CsPbBr_3$ nanosheets suspension was used to spin coat thin film on the substrate, followed by spin coating a TiO_2 thin film on top of it (Figure 4.20A). This architecture can efficiently enhance charge transport, charge separation (electron extraction/transport layer) and stability. it is useful for photodetectors, perovskite solar cells and photocatalytic applications.
ii. Mixed configuration : TiO_2 nanostructures were dispersed into the Mn-$CsPbBr_3$ nanosheets suspension, and the resulting mixture was spin-coated to form a nanocomposite thin film (Figure 4.20B). This hybrid structure aims to enhance charge separation and transport within the active layer. It is particularly useful for photocatalysis.

4.3.3.5.1 Layered configuration

In this configuration, the nanostructures of Mn-$CsPbBr_3$ and TiO_2 were spin coated, one after the other, to develop a configuration where a thin film of Mn-$CsPbBr_3$ is covered by a thin film of TiO_2. Except for the case of TNTAs, in which the limitations set by structural configuration only allow is to deposit a layer of Mn-$CsPbBr_3$ on the top. The schematic for this system is show in the Figure 4.21 below

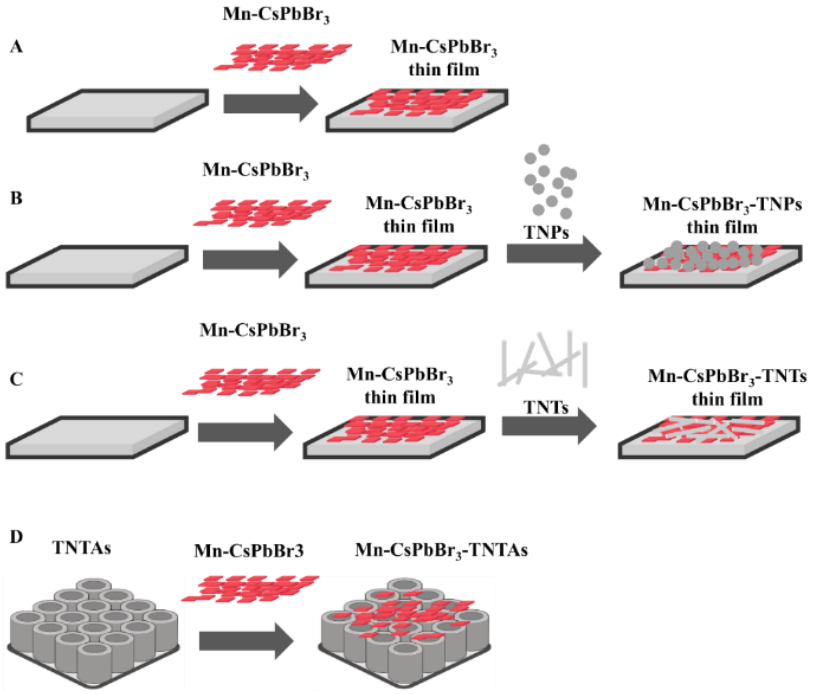

Figure 4.21) Schematic representation of sample preparation in layer-by-layer configuration. The representation is not according to the scale

The as developed samples were analysed using for their Mn PL lifetime at 600 nm, 615 nm and 636 nm, and the corresponding results are shown in the Figure 4.22 below

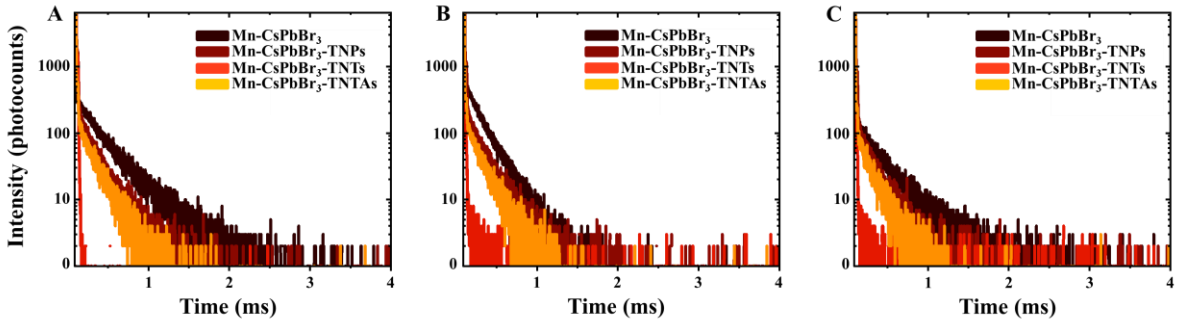

Figure 4.22) TRPL analysis of Mn-CsPbBr3 PL emission after exposure to different morphologies of TiO_2 in layer-by-layer configuration, measured at (A) 600 nm, (B) 615 nm and (C) 636 nm

Due to higher standard deviation in the values obtained after fitting the spectra for Mn-CsPbBr3/TNTs systems, the corresponding spectra in Figure 4.22 are shown for qualitative comparison. The lifetime curves for Mn-CsPbBr3 thin films show a small and steep initial drop in photocounts for all three wavelengths. As different morphologies of TiO_2 are introduced to the perovskite thin film, this drop in intensity becomes more intense, showing direct evidence of interaction. Furthermore, the decrease in intensity shows a relationship with the morphology of quencher. To understand this behaviour, we fit all the Mn PL lifetime results for Mn-CsPbBr3 and Mn- Mn-CsPbBr3/TiO_2 thin films with bi-exponential decay and the results are shown in Table 4.3 plotted in the Figure 4.23

Table 4.3) Lifetime components and their relative contributions, corresponding to Figure 4.22

	600 nm					
	τ_1 (µs)	f_1	τ_2 (µs)	f_2	χ^2	τ_{Avg} (µs)
Mn-CsPbBr3	130 ± 5.1	0.33	357 ± 7.5	0.67	0.991	226

Mn-$CsPbBr_3$ /TNPs	19 ± 1.0	0.97	183 ± 1.0	0.03	0.987	20
Mn-$CsPbBr_3$ /TNTAs	44 ± 2.9	0.56	199 ± 2.8	0.44	0.977	67

615 nm

	τ_1 (µs)	f_1	τ_2 (µs)	f_2	χ^2	τ_{Avg} (µs)
Mn-$CsPbBr_3$	119 ± 6.3	0.411	230 ± 8.0	0.59	0.995	166
Mn-$CsPbBr_3$ /TNPs	42 ± 2.0	0.60	199 ± 2.0	0.40	0.987	62
Mn-$CsPbBr_3$ /TNTAs	64 ± 4.0	0.46	205 ± 4.2	0.54	0.981	102

636 nm

	τ_1 (µs)	f_1	τ_2 (µs)	f_2	χ^2	τ_{Avg} (µs)
Mn-$CsPbBr_3$	114 ± 7.2	0.28	339 ± 8.6	0.72	0.981	217
Mn-$CsPbBr_3$ /TNPs	74 ± 4.2	0.52	229 ± 6.6	0.48	0.975	110
Mn-$CsPbBr_3$ /TNTAs	55 ± 7.8	0.42	194 ± 5.7	0.58	0.949	94

.

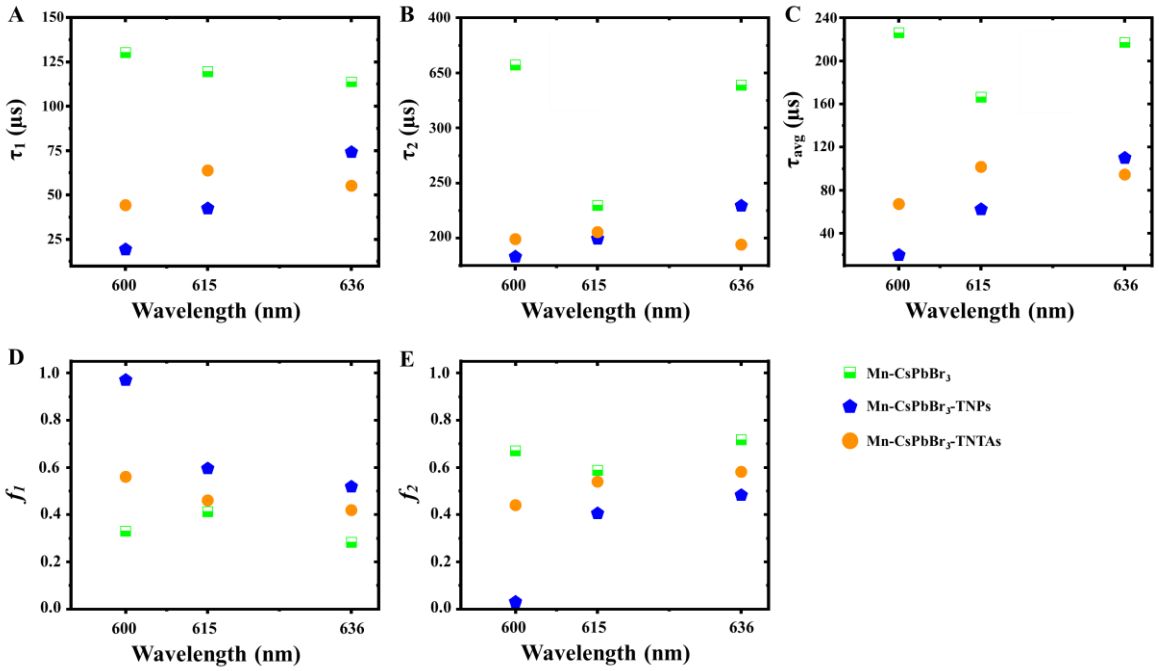

Figure 4.23) (A-E) TRPL analysis for Mn PL emission peak of Mn-$CsPbBr_3$ after exposure to different morphologies of TiO_2 in layer-by-layer configuration and the obtained lifetime components (A) τ_1 , (B) τ_2 , their corresponding relative contributions (D and E), respectively. The average lifetime is shown in (C) τ avg. The TRPL readings were taken at 600 nm, 615 nm and 636 nm

The Figure 4.23 show that τ_1 and τ_2 decrease upon interaction with both the morphologies of TiO_2, across all three wavelengths. Furthermore, τ_1 shows higher relative contribution (f_1) for both the morphologies of TiO_2 as compared to Mn-$CsPbBr_3$, whereas the relative contrition for τ_2 (f_1) shows the inverse trend. Considering the τ_{avg} for all the three wavelengths, we can conclude that all the morphologies show decrease in lifetime at all three wavelengths.

The results further reveal that considering the τ_{avg} for 600 nm B-Mn emission, TNPs show the least quenching, TNTs show the better quenching as compared to TNRs. Similar analysis of 636 nm wavelength shows a different trend with TNPs having the longer lifetime and TNRs show relatively shorter lifetime. Finally, the 615 nm, which can be considered as the average of both components shows that TNPs are best possible morphology for quenching of charge carriers residing in Mn states. This is followed by matching performance of TNPs and TNRs. Furthermore, it can be established TNPs and TNRs, are efficient at quenching the B-Mn as compared to S-Mn.

4.3.3.5.2 Mixed configuration

For this analysis, the Mn-$CsPbBr_3$ nanostructures were mixed with TiO_2 and spin coated on the glass substrates. This configuration would allow the nanostructures to mix well with the quencher and develop more efficient contact. Furthermore, since perovskites are also buried underneath the surface, it also adds to the protection of these sensitive materials. Figure 4.24 shows the preparation process for the thin films

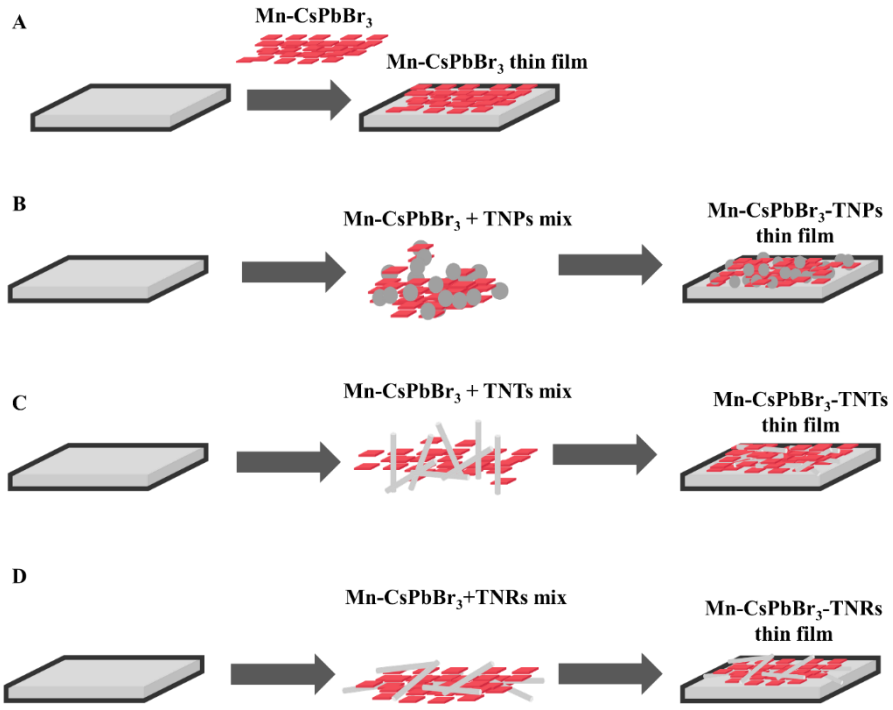

Figure 4.24) Schematic representation of sample preparation in mixed configuration. The representation is not according to the scale.

In this case, the use of TNTAs was limited due to the nature of substrates. The as developed thin films were tested for lifetime of PL Mn emission and results are show in Figure 4.25

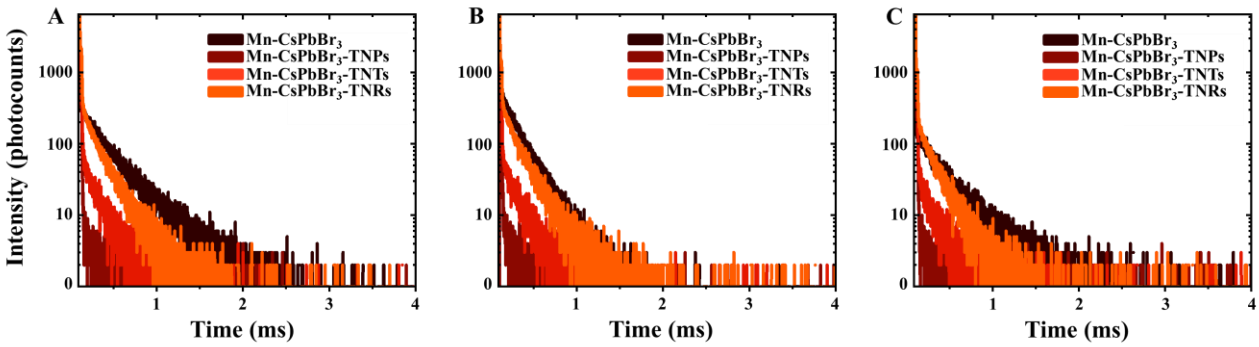

Figure 4.25) TRPL analysis of Mn-$CsPbBr_3$ PL emission after exposure to different morphologies of TiO_2 in mixed configuration, measured at (A) 600 nm, (B) 615 nm and (C) 636 nm

As expected, the results show decrease in lifetime of Mn PL emission. The fitted data and its components are shown in Table 4.4 and plotted in the Figure 4.26.

Table 4.4) Lifetime components and their relative contributions, corresponding to Figure 4.25

600 nm						
	τ_1 (µs)	**f_1**	**τ_2 (µs)**	**f_2**	**χ^2**	**τ_{Avg} (µs)**
Mn-$CsPbBr_3$	130 ± 5.1	0.33	357 ± 7.5	0.67	0.991	226
Mn-$CsPbBr_3$ /TNPs	57 ± 7.8	0.69	303 ± 28.3	0.31	0.586	77
Mn-$CsPbBr_3$ /TNTs	25 ± 1.6	0.93	192 ± 2.6	0.07	0.954	27
Mn-$CsPbBr_3$ /TNRs	40 ± 1.4	0.63	197 ± 1.5	0.37	0.991	57

615 nm						
	τ_1 (µs)	**f_1**	**τ_2 (µs)**	**f_2**	**χ^2**	**τ_{Avg} (µs)**
Mn-$CsPbBr_3$	119 ± 6.3	0.411	230 ± 8.0	0.59	0.995	166
Mn-$CsPbBr_3$ /TNPs	24 ± 2.2	0.98	242 ± 12.6	0.02	0.663	25
Mn-$CsPbBr_3$ /TNTs	47 ± 4.7	0.52	207 ± 4.4	0.48	0.953	75
Mn-$CsPbBr_3$ /TNRs	66 ± 2.5	0.48	213 ± 3.0	0.52	0.991	103

636 nm						
	τ_1 (µs)	**f_1**	**τ_2 (µs)**	**f_2**	**χ^2**	**τ_{Avg} (µs)**
Mn-$CsPbBr_3$	114 ± 7.2	0.28	339 ± 8.6	0.72	0.981	217
Mn-$CsPbBr_3$ /TNPs	41 ± 4.6	0.84	378 ± 33.0	0.16	0.460	48
Mn-$CsPbBr_3$ /TNTs	40 ± 4.1	0.67	205 ± 5.3	0.33	0.916	54

Mn-$CsPbBr_3$ /TNRs	46 ± 2.3	0.55	198 ± 2.2	0.45	0.986	70

The TNPs show lowest τ_{avg} value among all the morphologies at 615 nm. The Figure 4.26 demonstrates that all three TiO_2 morphologies show shorter lifetime for the S-Mn emission. Among the morphologies, TiO_2 nanoparticles (TNPs) exhibit the most pronounced effect on the S-Mn emission. In contrast, the other two morphologies are more effective in suppressing the B-Mn emission compared to TNPs. Notably, the relative contribution of S-Mn emission increases in the presence of TiO_2. This behaviour can be attributed to the structural arrangement of Mn-doped $CsPbBr_3$ thin films, where closely packed nanostructures facilitate direct contact between neighbouring domains. In such configurations, S-Mn centres may behave similarly to B-Mn centres due to proximity-induced interactions, thereby reducing the relative contribution of S-Mn emission. The introduction of TiO_2 morphologies, acting as large-sized quenchers, promotes spatial separation among the nanostructures.

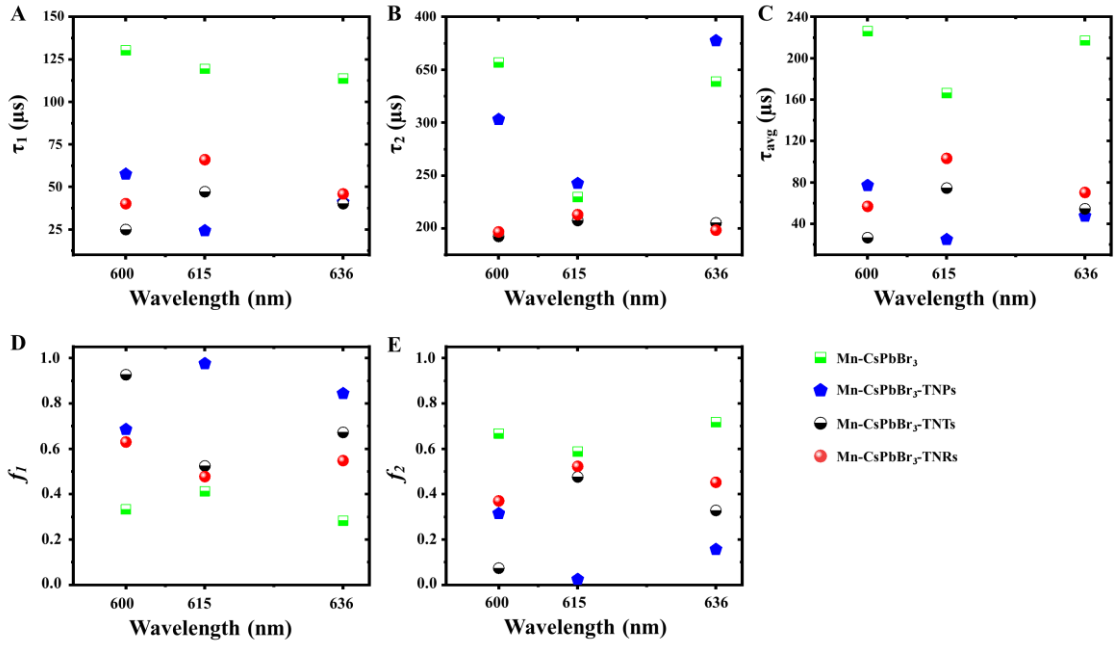

Figure 4.26) (A-E) TRPL analysis for Mn PL emission peak of Mn-$CsPbBr_3$ after exposure to different morphologies of TiO_2 in mixed configuration and the obtained lifetime components (A) τ_1, (B) τ_2, their corresponding relative contributions (D and E), respectively. The average lifetime is shown in (C) τ_{avg}. The TRPL readings were taken at 600 nm, 615 nm and 600 nm

This separation inhibits inter-nanostructure coupling, allowing the S-Mn sites to retain their radiative recombination characteristics, which accounts for the apparent revival in their relative contribution in the presence of TiO_2. Nevertheless, the lifetime of S-Mn decreases, showing the interaction with TiO_2. Overall, based on the average lifetime results obtained at 615 nm, the TNPs shows the shortest lifetime, followed by TNTs and TNRs.

4.3.4 Mn-$CsPbBr_3$/PMMA based thin film luminescent concentrators

Since the Mn trap states inhibit charge carriers from returning to the $CsPbBr_3$ lattice, recombination occurs exclusively through Mn states. This behaviour is particularly advantageous for ultraviolet (UV) to visible light down-conversion because conventional silicon-based photovoltaic (PV) cells exhibit peak efficiency in the near-infrared (NIR) to visible spectral range but are relatively inefficient at directly utilizing high-energy UV photons. When UV light is absorbed by luminescent materials and re-

emitted as lower-energy visible photons, it better matches the absorption profile of crystalline silicon solar cells, thereby enhancing overall spectral utilization.

In addition, direct exposure to UV radiation can accelerate material degradation in encapsulants, coatings, and active layers, as well as increase thermal loading. The absorption of UV photons generates excess heat rather than usable electrical energy, which elevates the operating temperature of the device. Since the efficiency of Si-based solar cells decreases with increasing temperature (typically ~0.4–0.5% per °C above standard test conditions), this thermal burden leads to notable performance losses.

By down-converting UV photons into visible light, luminescent solar concentrators not only expand the usable spectral range but also mitigate UV-induced heating and photodegradation. This dual effect contributes to both improved device stability and higher net energy conversion efficiency. Moreover, since the re-emitted photons are waveguided toward the cell edges, the approach enables more efficient use of smaller, high-quality solar cells while protecting large-area surfaces from direct UV exposure. Moreover, the significant spectral separation between absorption and PL emission effectively eliminates the re-absorption of emitted photons, promoting lateral light propagation via the waveguide effect. When combined with the high PLQY of Mn emission, these materials emerge as promising candidates for use in luminescent solar concentrator (LSC) devices.

The problem perovskite material lies with the stability towards ambient conditions such as humidity and high temperature. A number of techniques have been reported in the literature to tackle these issues, and among them, one is encapsulating these materials. The encapsulation can be done in the form of core-shell structure development or in transparent polymers. Some particular polymers such as PMMA have been widely used to develop luminescent concentrators. By protecting the perovskites in PMMA and spin coating them on a transparent substrate leads to formation of thin film luminescent concentrators. This resolves the stability issue as well provides a functional aspect. Mn-CsPbBr3/PMMA based luminescent concentrators shown in the Figure 4.27

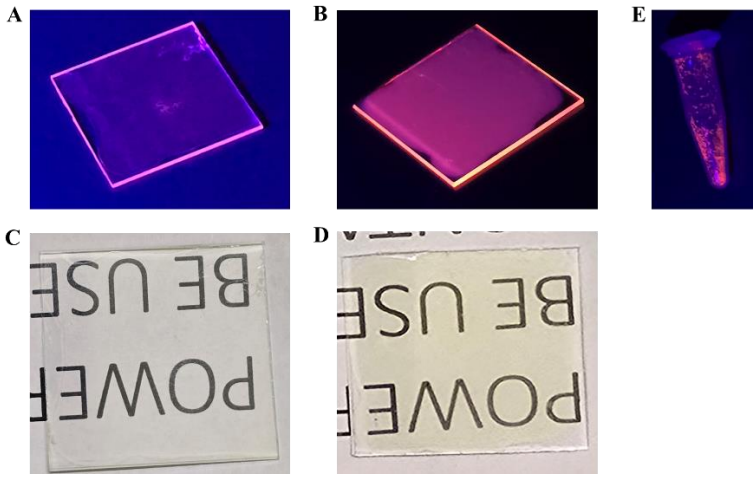

Figure 4.27) Mn-$CsPbBr_3$ embedded in thin film of PMMA as luminescent concentrators (A-B) under UV light and the transparency of the corresponding samples (C,D). The shards of Mn-$CsPbBr_3$ embedded in PMMA under UV light (E)

The as prepared luminescent concentrators were exposed to solar simulator (AM 1.5) and the response was recorded using a PL detector. The results are shown in Figure 4.28

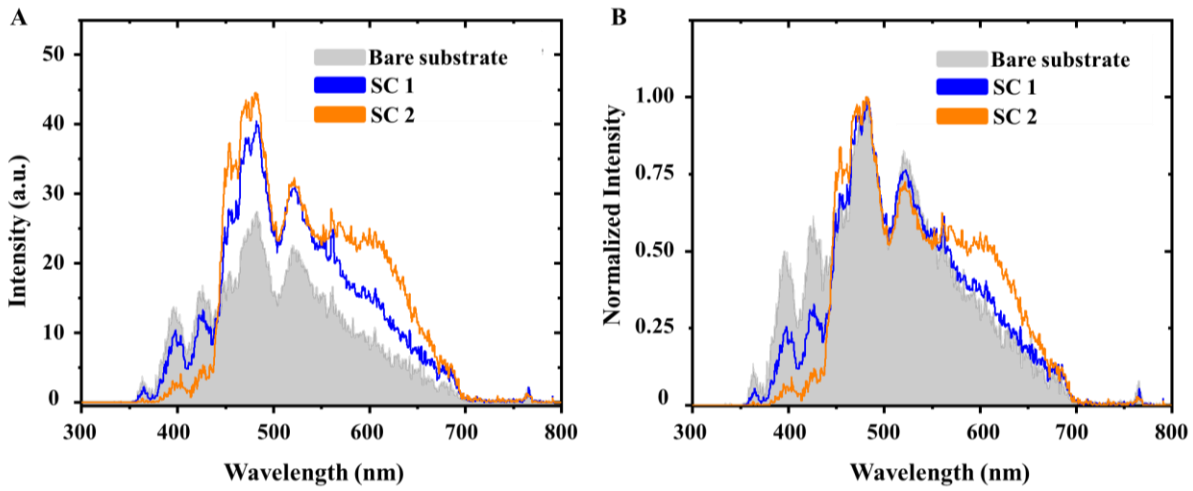

Figure 4.28) (A) As recorded and (B) Normalized response of thin film luminescent concentrators SC1 (low concentration) and SC2 high concentration

The results indicate that Mn-$CsPbBr_3$ effectively down shift the UV section of solar spectra to higher wavelengths.

4.4 Summary

The chapter focuses on the charge carrier dynamics of Mn states in Mn-doped $CsPbBr_3$ perovskite nanosheets and their interaction with different TiO_2 morphologies. The doping of perovskites with Mn aims to exploit their dual emission features (surface and bulk Mn^{+2} emission) to study exciton behaviour and charge transfer mechanisms. The synthesis is carried out via hot injection, followed by TEM, EDS, and optical characterizations. The chapter then investigates the PL behaviour and time-resolved PL (TRPL) under different experimental setups:

- Mn-doped PNCs are interfaced with TNPs, nanotubes (TNTs), and nanorods (TNRs) in solution.
- Charge transfer is quantified using PL quenching, Stern-Volmer analysis, and TRPL deconvolution.
- Three sample configurations are tested: solution phase, layer-by-layer films, and mixed-phase composites, revealing morphology-dependent charge dynamics.
- A prototype PMMA-based luminescent concentrator incorporating Mn-doped nanosheets demonstrates UV-to-visible down conversion capability.
- The magnetic response of Mn PL emission is briefly explored, showing magneto-optical potential.

4.4.1 Challenges and limitations

Advanced spectroscopic techniques are needed to have an in depth understanding of charge carrier dynamics in Mn-$CsPbBr_3$/TiO_2 systems. Particularly, a femtosecond laser can reveal the intricate details of carrier dynamics in the perovskite, and its relationship with Mn emission. Furthermore, a 420 nm femto/picosecond laser can help in obtaining the charge transfer component, representing the quenching of carriers by TiO_2. Finally, photocatalytic activity of these samples needs to be studied, to understand if Mn-$CsPbBr_3$/TiO_2 systems can outperform the pristine Mn-$CsPbBr_3$ or not.

4.5 Future outlook

$CsPbBr_3$ perovskite is non-magnetic material, on the other hand, Manganese is strongly paramagnetic.

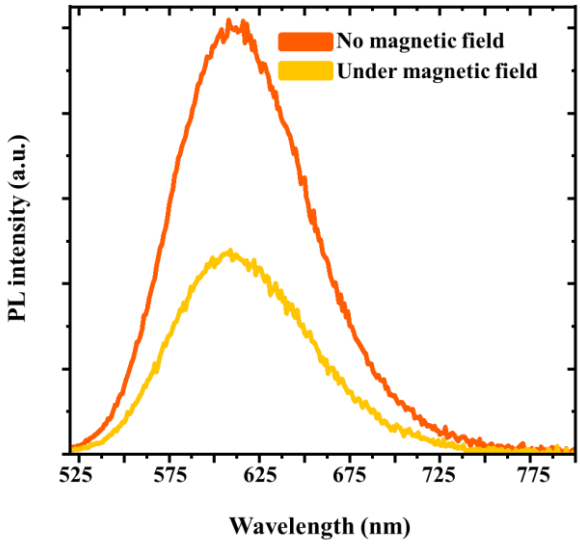

Figure 4.29) Mn PL emission of CsPbBr3 at 615 nm influenced by the magnetic field

Upon doping of Mn in $CsPbBr_3$, the perovskite adopts the paramagnetic nature as well. It has been reported in the literature that Mn-$CsPbBr_3$ materials show even longer lifetime for Mn emission under magnetic field as compared to normal conditions. In effect, the charge carriers are held in conduction band for a longer time due to the interaction of two unbound electron in d-orbital of Mn with the magnetic field. As an initial proof of concept for our work, we performed an experiment in which we observed the PL intensity of Mn in the presence and absence of magnetic field (spinning electromagnet ≈100 mT) and the results are shown in the Figure 4.29A systematic study of influence of intensity of magnetic field on the charge carrier dynamics of Mn-$CsPbBr_3$ and the corresponding effect on the photocatalytic activity could be performed. Further analysis may also include an attempt to increase the internal and overall PLQY of Mn emission, which would enable these materials to be used as efficient UV to visible light converters for solar application as well as for photocatalytic activity.

5 Wavefunction engineering for tailoring of charge carrier dynamics in CdTe/CdSe (core-shell)/TiO_2 nanocomposites

In the pervious chapters, perovskite nanomaterials were demonstrated as sensitizers for TiO_2. Although perovskites have greener chemistry, excellent optical properties and high efficiency in various applications, their long-term stability, particularly under moisture, heat, and light exposure remains a significant challenge. For a more robust and reliable photocatalytic and optoelectronic systems, II–VI semiconductor quantum dots such as Cadmium Sulfide (CdS), Cadmium Selenide (CdSe), Cadmium Telluride (CdTe) and their Zinc based counterparts can offer superior stability. The stable nature of Cadmium (Cd) based II-VI semiconductors allows for their long-term application and minimizes the leeching of Cd. Furthermore, these materials are well investigated, established and reported in literature. Their optoelectronic properties can be precisely tuned, this in addition to convenient handling qualifies them as ideal candidates to serve as trail platforms for proof-of-concept studies to gain in depth understanding of device functionality in environments which could be considered harsh for recently introduced greener nanomaterials.

This chapter presents an investigation into type-II core-shell quantum dot structures (CSQDs) of Cadmium Telluride (core) and Cadmium Selenide (shell) to develop CdTe-CdSe CSQDs capable of initiating spatial charge separation in CSQDs. The capability of TiO_2 morphologies to accept these separated charge carriers is monitored using steady state and time resolved PL. Similar to previous sections, these investigations extend from liquid phase to thin film phase, for the purpose of developing an overview of how effectively a quencher morphology can interact with II-VI semiconductor based CSQDs.

5.1 II-VI semiconductor quantum dots

II–VI semiconductor quantum dots are nanocrystalline materials consisting of elements from group II (e.g., Zn, Cd, Hg) and group VI (e.g., O, S, Se, Te) of the periodic table. Owing to their direct bandgap nature, these compounds demonstrate high efficiency in both optical absorption and radiative emission processes. These materials have been studied extensively for their applications in light emitting diodes [166], [167], [168], lasers [169], [170], [171] , solar cells [172], [173], [174] and photocatalysis [168], [175], [176], [177] due to ease of tailoring of their optical and electronic properties by altering the size of the QDs.

For the purpose of photocatalysis, the II-VI QDs can either be utilized directly as a photocatalyst [178], [179], [180] or can be paired as a sensitizer with a more efficient photocatalyst such as TiO_2 [181], [182], [183], [184]. Different morphologies of TiO_2 sensitized with II-VI semiconductor quantum dots (QDs/TiO_2 heterostructure nanocomposites) have been used for photocatalytic activity, such as nanoparticles [185], [186], [187] and nanotubes [188], [189], [190], [191], [192]. In both scenarios, stability and efficient charge transfer are the key priority. In case of QDs acting as sensitizers, there is an additional advantage of charge carrier separation, which can be achieved by developing a type-II alignment, as discussed in section 1.5.

5.1.1 Cadmium Telluride (CdTe) quantum dots

Cadmium Telluride (CdTe) quantum dots have been explored for their ability to harvest solar energy [193], [194]. The CdTe QDs possess high absorption coefficient and allow for efficient absorption in

higher wavelength region of visible spectrum due to small bandgap energy, this is particularly useful for solar energy conversion. Furthermore, the conduction band position of CdTe lies at more negative potential as compared to CdSe, CdS and the traditional photocatalysts such as TiO_2. This allows for smooth injection of excited charges to TiO_2 and hence charge separation. However, they have the drawback of relatively lower intrinsic long-term stability in comparison to Cadmium selenide (CdSe) and Cadmium Sulfide (CdS). Nonetheless, CdTe QDs have been used as sensitizers for TiO_2 for improved photocatalytic activity [77], [195], [196], [197], [198].

5.1.2 Cadmium Telluride-Cadmium Selenide core-shell quantum dots (CdTe-CdSe CSQDs)

A shell of Cadmium Sulfide (CdS) around the CdTe core can tackle the stability, passivate the defects and create new radiative recombination pathways for the charge carriers and provide necessary charge carrier separation. However, the lattice mismatch between CdTe and CdS zinc-blende structures is high (=0.73 Å)[199], hence the higher value for interfacial strain emerges. As an alternative, Cadmium Selenide (CdSe) shell around CdTe core results in only 0.40 Å lattice mismatch[200], hence lower strain exists at the core-shell interface and CSQDs witness enhanced mobility of carriers. Furthermore, CdSe has higher value for conduction band-offset as compared to CdS [201], therefore, thinner shell can lead to localization of electron wave-function in CdSe shell. This is crucial because over-coating through thick shells can lead to creation of misfit dislocations, hence opening new channels of non-radiative recombination[202]. In addition, since any absorption from CdSe lies in visible range, it can increase the harvesting capacity of quantum dots, as compared to the near UV absorbing CdS shell.

5.1.3 Photocatalytic degradation of Rhodamine B dye

Photocatalytic degradation of Rhodamine B (RhB) dye is widely used as a model reaction to assess the photocatalytic performance of TiO_2-based materials. Under UV or visible light irradiation, TiO_2 generates electron–hole pairs (e^-/h^+), where photo-excited electrons migrate to the conduction band, and holes remain in the valence band. These charge carriers interact with surface-adsorbed oxygen and water molecules, producing reactive oxygen species (ROS), such as hydroxyl radicals (•OH) and superoxide anions ($O_2^{\bullet-}$), which drive the oxidative degradation of RhB molecules. The degradation process converts RhB into smaller organic intermediates and ultimately to CO_2, H_2O, and inorganic ions.

Typically, the reaction kinetics are monitored by measuring the decline in the characteristic absorption peak of RhB at 553 nm using UV-Vis spectroscopy, often following a pseudo-first-order kinetic model. The reaction scheme [203] is summarized below

$$TiO_2 + h\nu \rightarrow e^- CB + h^+ VB$$

$$h^+ VB + \ + H_2O \rightarrow \cdot OH + H^+$$

$$h^+ VB + \ + OH^- \rightarrow \cdot OH$$

$$e^- CB + O_2 \rightarrow O_2 \cdot$$

$$\cdot OH / O_2 \cdot - + \text{RhB dye} \rightarrow \text{intermediates} \rightarrow CO_2 + H_2O + \text{inorganic ions}$$

5.1.4 CdTe-CdSe CSQDs / TiO_2 nanoheterostructures

The CSQDs when combined with a photocatalyst to develop a type-II nanoheterostructures can lead to improved efficiency [204], [205], [206]. Such arrangements improve the carrier separation by injecting the electrons in the conduction band of the photocatalyst, this combined with larger number of photo-catalytically active sites on TiO_2 yields efficient solar energy conversion. As discussed earlier, CdTe-CdSe CSQDs exhibit a smaller lattice mismatch, and a more favourable band offset for charge carrier injection into the conduction band of the CdSe shell compared to the CdS shell. The improved lattice compatibility reduces interfacial defects and minimizes non-radiative recombination at the core–shell interface. Additionally, the band alignment in CdTe-CdSe structures promotes efficient spatial separation of electrons and holes, enabling optimal carrier dynamics. These properties make CdTe-CdSe CSQDs more suitable for facilitating effective charge transfer to TiO_2, thereby enhancing their potential as sensitizers in photocatalytic systems. To this end, a systematic analysis of interaction between CSQDs/TiO_2 heterostructures is essential. The CSQDs/TiO_2 heterostructure nanocomposites may vary in performance depending on the morphology of TiO_2, which tailors the charge carrier dynamics of the system. Hence, it is crucial to evaluate the morphology-charge carrier dynamics relationship for CSQDs/TiO_2 heterostructure nanocomposite. The media facilitating the interaction of these heterostructures also dominates the carrier dynamics.

We produce CdTe/CdSe CSQDs using hot injection (for CdTe core) and SILAR (for CdSe shell) and study the interaction of these CSQDs with different morphologies of TiO_2 (nanoparticles and nanotubes) under varying configurations (solution state and thin films). Since CdTe/CdSe CSQDs show enhanced carrier separation, the lifetime of charges becomes longer, and additional carriers are available for 'collection' and transfer. The CSQDs/TiO_2 heterostructure nanocomposites could lead to increase in number of available charge carriers, hence enhanced photocatalytic activity.

5.1.5 Objectives

The main objectives of this chapter are

- To introduce spatial separation of charge carriers and enhance the PL decay lifetime
- Study the effect of TiO_2 morphologies in liquid and thin film state
- To evaluate the photocatalytic activity of CdTe-CdSe/TiO_2 nanocomposites

5.2 Experimental

5.2.1 Materials used

All the materials were ordered from Sigma Aldrich unless otherwise stated and used without any further purification. For the synthesis, the materials used were Cadmium acetate dihydrate (>98.0%), Selenium powder (99.5+%), Tellurium powder (99.8%), Octadecylphosphonic acid (97%), Oleic acid (90%), 1-Octadecene (90%) and Trioctylphosphine (90%). Titania nanoparticles (<25 nm, 99.7%) and Titania nanotubes (<500 nm). The TNTAs were domestically grown.

5.2.2 Synthesis of quantum dots

The CdTe QDs were synthesized using a modified hot-injection method, as reported in the literature [207]. In our approach, Se was replaced with Te, TOPO was used to prepare the Te precursor, ODE served as the non-coordinating solvent, and the amounts of reactants were adjusted to ensure the formation of spherical nanocrystals rather than tetrapods.

5.2.2.1 Synthesis of CdTe QDs

5.2.2.1.1 Tellurium precursor preparation

The tellurium precursor solution was prepared by dissolving elemental tellurium (26 mg, 0.2 mmol) in tri-n-octylphosphine (0.2 mL, 0.8 mmol) with 2 mL of 1-octadecene, which was heated to 50 °C under similar conditions. Upon complete dissolution, the tellurium precursor was colourless. The precursor was stored under inert atmosphere.

5.2.2.1.2 Cadmium precursor preparation

Cadmium acetate (54 mg, 0.2 mmol), oleic acid (0.3 mL, 1 mmol), and octadecylphosphonic acid (19 mg, 0.05 mmol) were combined with 20 mL of 1-octadecene in a three-neck flask. This mixture was heated to 295 °C under continuous stirring and an inert atmosphere until a it became transparent.

5.2.2.1.3 Hot injection

The tellurium precursor solution was rapidly injected into the hot cadmium precursor solution, initiating the formation of CdTe QDs, evident by the appearance of a dark-coloured colloidal suspension. Following the injection, the reaction temperature was reduced to 265 °C and maintained for 20 minutes to facilitate nanocrystal growth, after which the mixture was allowed to cool gradually to room temperature.

5.2.2.1.4 Cleaning process for CdTe QDs

The resulting colloidal product was purified by washing with methanol and precipitating the QDs from 1-octadecene using acetone. The black precipitate was collected by centrifugation and subsequently redispersed in 1-octadecene for storage and further applications.

5.2.3 Growth of CdSe shell

The SILAR technique was performed as reported by Slejko et al [208] with slight modifications.

5.2.3.1 Cadmium precursor preparation

Cadmium precursor solution was prepared by dissolving cadmium acetate dihydrate (108 mg, 0.4 mmol) and oleic acid (0.6 mL, 2.0 mmol) in 9.4 mL of 1-octadecene. The mixture was heated to 250 °C under continuous stirring in an inert atmosphere and maintained at this temperature for 20 minutes to ensure complete complexation and homogenization.

5.2.3.2 Selenium precursor preparation

Selenium precursor solution was prepared by combining selenium powder (31.5 mg, 0.4 mmol) with tri-n-octylphosphine (0.2 mL, 0.8 mmol) in 8 mL of 1-octadecene. This mixture was gently heated to 50 °C under inert conditions until a clear and homogeneous solution was obtained, indicating complete dissolution of selenium. Following synthesis, both cadmium and selenium precursor solutions were allowed to cool to ambient temperature and subsequently stored under inert atmosphere for future use in shell growth procedures.

5.2.3.3 Successive Ionic Layer Adsorption and Reaction for growth of CdSe shell

A total of 12 mL of 1-octadecene was heated to 260 °C in a three-neck flask under an inert atmosphere. Subsequently, pre-synthesized CdTe core quantum dots (0.04 mmol), dispersed in 3 mL of 1-octadecene, were swiftly injected into the hot solvent. Upon injection, the reaction temperature was adjusted and stabilized at 240 °C. At this stage, calculated quantities (1 mL, 1.4 mL and 1.8 mL) of cadmium and selenium precursors were introduced sequentially into the CdTe core suspension via controlled dropwise addition. The precursor addition rate was carefully regulated to ensure that the

precursor concentration within the reaction vessel remained below the threshold required for homogeneous nucleation, thereby promoting exclusive heterogeneous shell growth on the CdTe cores. One complete injection cycle of cadmium followed by selenium precursors constituted the deposition of a single monolayer (ML) of CdSe. This shell growth process was repeated iteratively to deposit three monolayers in total.

5.2.3.4 Cleaning process of CdTe-CdSe CSQDs QDs

The final product was washed with methanol twice and suspended in hexane.

5.2.4 CdTe-CdSe/TiO_2 nanocomposite preparation

5.2.4.1 Nanoparticles and Nanotubes

A total of 60 mg of TiO_2 nanostructures were dispersed in 7 mL of hexane, followed by the addition of 1.2 mg of CdTe/CdSe core–shell quantum dots, pre-dispersed in 2 mL of hexane. The resulting mixture was subjected to continuous magnetic stirring at 900 rpm for 4 hours at ambient temperature to facilitate quantum dot sensitization of the TiO_2 surface. After stirring, the suspension was centrifuged at 3600 rpm to recover the nanocomposite material, which was subsequently dried in an oven at 120 °C for 25 minutes to ensure the removal of residual solvents and promote effective quantum dot attachment.

5.2.4.2 Titanium dioxide nanotube arrays

A 1.8 mg aliquot of CdTe/CdSe core–shell quantum dots, dispersed in 2 mL of hexane, was deposited onto a 2 cm × 1 cm TiO_2 nanotube array (TNTA) substrate via spin coating at 1000 rpm for 4 seconds. Following deposition, the film was dried under an argon stream and subsequently annealed at 120 °C for 25 minutes to facilitate efficient quantum dot sensitization, ensure robust adherence to the TNTA surface and convenient evaporation of solvent.

5.2.5 Characterization techniques

5.2.5.1 X-ray diffraction

Powder X-ray diffraction (XRD) analysis was carried out using an Aeris diffractometer (Malvern PANalytical) equipped with a Cu $K\alpha_1$ radiation source (λ = 1.5406 Å). The samples were prepared by drop-casting the colloidal QD solution onto low-background silicon substrates to ensure optimal signal quality.

5.2.5.2 Uv-visible absorption

Ultraviolet-visible (UV-Vis) absorption spectra of core-shell quantum dots and TiO_2 NPs were recorded in a quartz cuvette using a Lambda 1050+ UV-Vis-NIR spectrometer from Perkin Elmer.

5.2.5.3 Steady state and time resolved photoluminescence

Steady-state and time-resolved PL measurements were conducted using an FS5 spectrofluorometer (Edinburgh Instruments). For time-resolved PL characterization, excitation was provided by a picosecond pulsed laser operating at 510 nm, and the emission decay profiles were recorded using the time-correlated single photon counting (TCSPC) technique to ensure high temporal resolution. The decay profiles were tail-fitted with a tri-exponential decay function (equation 3-1) and the amplitude-weighted average PL lifetime was calculated using the equation,

$$\tau_{avg} = \frac{A_1\tau_1 + A_2\tau_2 + A_3\tau_3}{A_1 + A_2 + A_3}$$

Also, the fractional contribution of each decay time to the steady-state amplitude was calculated using the formula,

$$f_i = \frac{A_i \tau_i}{A_1\tau_1 + A_2\tau_2 + A_3\tau_3}$$

The electron transfer rate constants for thin films were calculated based on the equation 3-4

5.2.5.4 Transmission electron microscopy

TEM images of CdTe QDs were acquired on a Jeol ARM20CF NeoARMelectron microscope at 200kV acceleration voltage. The samples were prepared by drop-casting the colloidal solution on the carbon-coated TEM grids. TEM images of CdTe-CdSe CSQDs, and their heterostructures with TNPs and TNTs, were acquired using Transmission electron microscope (CM 200, Philips) equipped with Quemesa camera (Olympus Soft Imaging Solutions). Image acquisition was done with RADIUS software.

5.2.5.5 Scanning Electron Microscopy

SEM characterization of anodically fabricated TiO_2 nanotube arrays sensitized with core–shell quantum dots was conducted using a Zeiss Gemini Supra 25 field-emission SEM operated at an accelerating voltage of 10 kV. For comparison, SEM imaging of bare TiO_2 nanotubes (without quantum dot deposition) was performed using a Zeiss Gemini SEM under an accelerating voltage of 5 kV.

5.2.5.6 Fluorescence Lifetime Imaging Microscopy

Fluorescence lifetime imaging microscopy (FLIM) was carried out under ambient conditions using a MicroTime 200 confocal fluorescence microscope (PicoQuant), equipped with a 440 nm picosecond pulsed laser, a 60× objective lens, a PMA Hybrid single-photon detector, and a PicoHarp 300 time-correlated single photon counting (TCSPC) module. The excitation beam produced a focal spot with a full width at half maximum (FWHM) of approximately 550 nm. For all FLIM acquisitions, the instrument response function (IRF) was recorded and incorporated into a reconvolution-based tri-exponential fitting model for accurate extraction of lifetime components and their relative contributions.

5.2.5.7 Photocatalytic degradation of Rhodamine B dye

A 40mL 10^{-5} M aqueous RdB solution was prepared in a beaker, and the sample was immersed into it using a mesh (to hold the sample in place and avoid direct contact with the stirrer). The setup was exposed to UV light under constant stirring to ensure a homogeneous reaction environment.

5.3 Results and discussion

This study examines the influence of varying titanium dioxide (TiO_2) morphologies on the charge carrier dynamics in CdTe/CdSe core–shell quantum dot (QD) systems. The synthesis begins with the preparation of CdTe QD cores, approximately 3.8 nm in diameter, utilizing a modified hot-injection method based on established protocols. These purified CdTe cores serve as nucleation centres for the growth of CdSe shells via the successive ionic layer adsorption and reaction (SILAR) technique. Following shell growth, the resulting CdTe/CdSe core–shell QDs were thoroughly washed with methanol twice and redispersed in hexane. A schematic illustration of the core and core–shell growth process is presented in Figure 5.1.

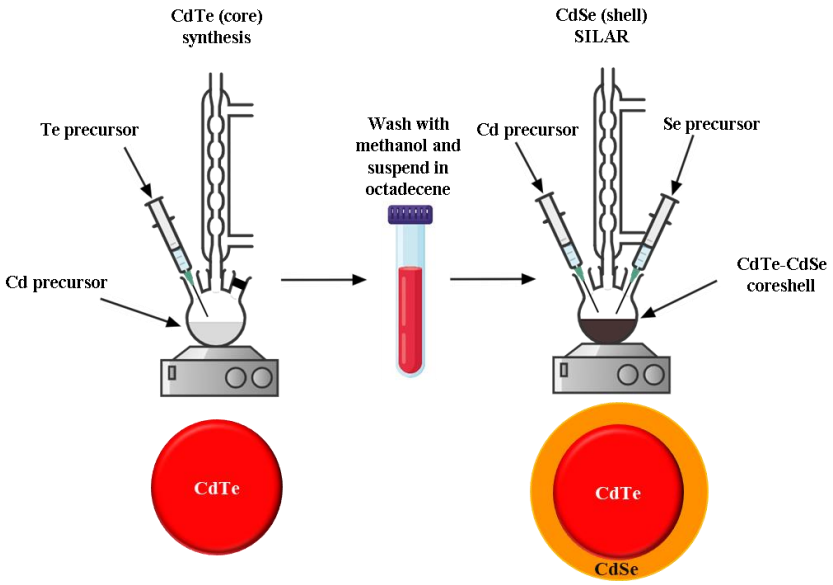

Figure 5.1) Schematic for the hot injection synthesis of CdTe QDs (core) and SILAR for developing CdSe (shell). The cross-section views of core and core-shell quantum dot structures are also shown

5.3.1 Morphological and structural analysis

The SILAR (Successive Ionic Layer Adsorption and Reaction) method is essential for achieving precise control over the thickness of each shell layer grown around the quantum dot core. In contrast, an alternative approach—the one-pot synthesis—involves the simultaneous addition of both shell precursors to the reaction mixture at room temperature, followed by gradual heating to the target shell growth temperature. Although this method simplifies the synthesis procedure, it compromises the accuracy of shell thickness control, leading to less uniform core–shell structures.

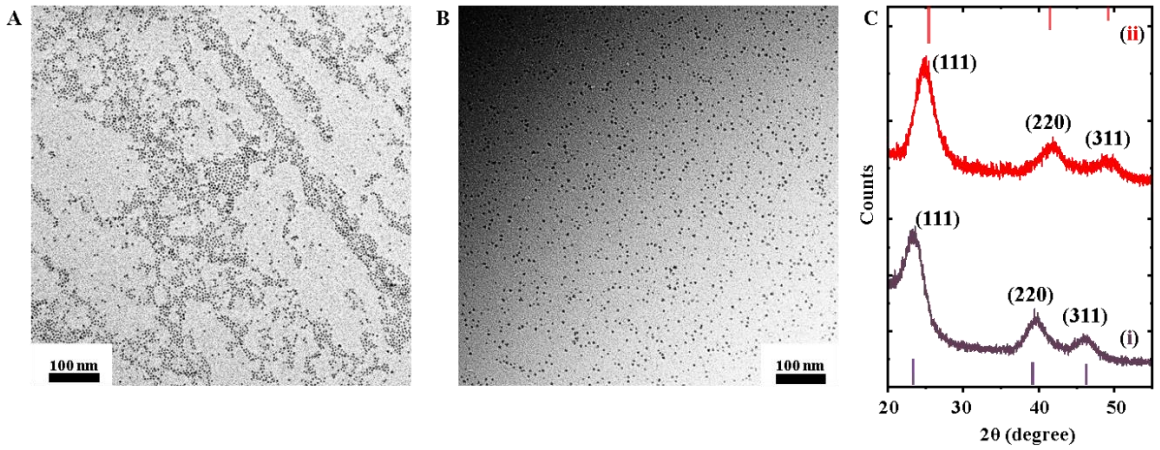

Figure 5.2) TEM images of (A) CdTe and (B) CdTe-CdSe core-shell quantum dot structures . (C) XRD patterns of (i) CdTe and (ii) CdTe-CdSe

The growth of a CdSe shell not only enhances the chemical and structural stability of CdTe [209] but also promotes more efficient electron–hole separation [210], while simultaneously red shifting the absorption onset toward the near-infrared (NIR) region. Transmission electron microscopy (TEM) images presented in Figure 5.2 A and Figure 5.2 B illustrate the morphology of the CdTe cores before and after CdSe shell growth, respectively. The average diameter of the CdTe cores is approximately 3.8 nm, which increases to 5.30 nm following shell formation, as confirmed by particle size analysis (Figure 5.3).

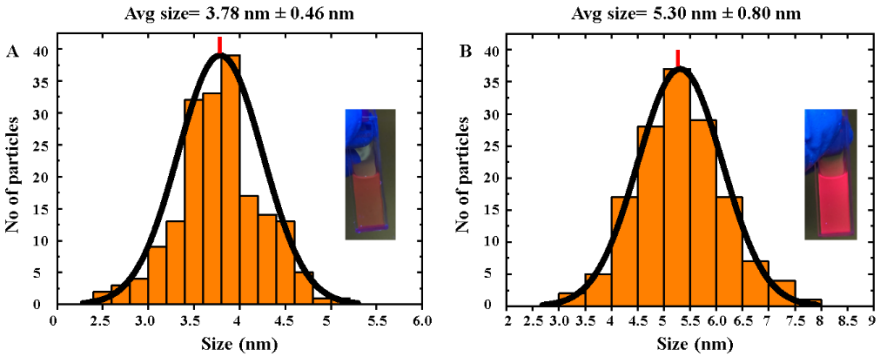

Figure 5.3) (A,B) Size histograms for (A) CdTe and (B) CdTe-CdSe core-shell quantum dot structures

X-ray diffraction (XRD) analysis (Figure 5.2C) reveals diffraction peaks corresponding to the (111), (220), and (311) planes of the face-centered cubic (FCC) zinc-blende structure of CdTe, located at 2θ values of 23.4°, 38.9°, and 46.0°, respectively (JCPDS No. 01-077-7297). Upon shelling with CdSe, a slight shift of these peaks to higher angles is observed. This shift is attributed to the compressive lattice strain imposed by the CdSe shell on the CdTe core, which reduces interplanar spacing and leads to peak displacement toward higher diffraction angles (JCPDS No. 00-066-1632) [211], [212].

5.3.2 Optoelectronic properties

Figure 5.4 shows the UV–Vis absorption and PL spectra of the as-synthesized CdTe quantum dots. The absorption spectrum displays the first excitonic peak at 612 nm, corresponding to a core diameter of ~3.77 nm, as estimated using Peng et al [213] empirical model. Subsequent excitonic transitions appear at 568 nm and 526 nm. The PL emission peak is centered at 624 nm, with a full width at half maximum (FWHM) of 36 nm. These characteristics are consistent with CdTe quantum dots, which are known to exhibit surface-related trap states and associated optical defects [214], [215].

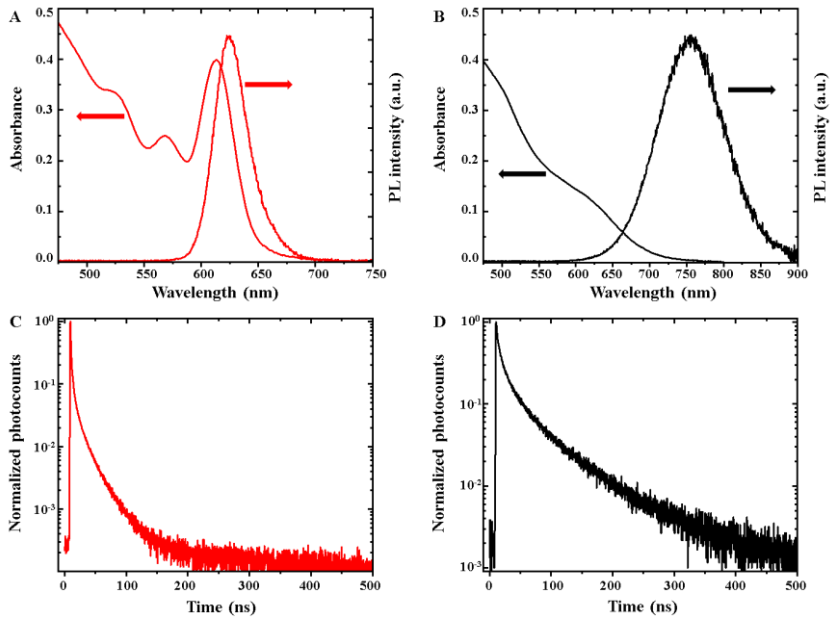

Figure 5.4) (A,B) Absorption and PL spectra of (A) CdTe and (B) CdTe-CdSe core-shell quantum dot structures. C,D) PL decay profiles for (C) CdTe and (D) CdTe-CdSe

The growth of CdSe shells on CdTe cores induces a redshift in the band-edge excitonic absorption to approximately in the region 735 - 743 nm (the peak gets nearly diminished due to the nature of type-II coreshell system), indicative of a reduced effective bandgap consistent with type-II band alignment in CdTe/CdSe core–shell quantum dots. The second excitonic peak (prominent than the first excitonic

peak) moves to 628 nm. The PL emission undergoes a similar redshift, as shown in Figure 5.4 B, with the emission peak appearing at 754 nm and exhibiting a full width half maximum (FWHM) of 108 nm. This broadening of PL spectra is attributed to potential inhomogeneity in shell thickness, as type-II heterostructures are highly sensitive to shell dimensions, a phenomenon previously reported by Aghoutane et al [216] .

To gain insight into the carrier dynamics and validate the impact of type-II band alignment, time-resolved PL measurements were performed using time-correlated single-photon counting (TCSPC). The decay profiles for CdTe and CdTe/CdSe QDs are shown in Figure 5.4 C and D, respectively. Each PL decay curve was analysed using a tri-exponential fitting model, from which amplitude-weighted average lifetimes (τavg) were derived and summarized in Table 5.1.

Table 5.1) PL lifetime components (τi) , corresponding fractional contribution(fi) of each decay time to the steady-state intensity, and amplitude-weighted average PL lifetimes (τ) obtained from multiexponential fitting of PL decay profiles of CdTe and CdTe-CdSe CSQDs.

	τ_1 (ns)	f_1	τ_2 (ns)	f_2	τ_3 (ns)	f_3	χ^2	τ_{Avg} (ns)
CdTe	2.5 ± 0.05	0.936	10.3 ± 0.6	0.048	29.8 ± 2.3	0.016	0.996	2.6
CdTe-CdSe	5.4 ± 0.13	0.334	22.7 ± 0.6	0.272	80.2 ± 1.4	0.394	0.999	12.8

The CdTe QDs exhibited a relatively fast τ_{avg} of 2.6 ns, whereas the core–shell CdTe/CdSe QDs demonstrated a significantly prolonged τ_{avg} of 12.8 ns. This nearly fourfold increase is a direct consequence of enhanced spatial separation of electrons and holes, driven by type-II band alignment, which reduces wavefunction overlap and slows radiative recombination. Such prolonged excited-state lifetimes are advantageous for charge transfer processes, as carriers remain delocalized for extended durations, improving their interaction with external quenchers.

5.3.3 Interaction with TiO_2

5.3.3.1 Liquid phase interactions and Stern-Volmer plot

To examine how quencher morphology influences this charge transfer efficiency, we studied the interaction of CdTe/CdSe core–shell QDs with two distinct TiO_2 morphologies—nanoparticles and nanotubes—under both colloidal (solution-phase) and thin-film conditions.

In the colloidal phase, we investigated the influence of varying concentrations of titanium dioxide (TiO_2) nanoparticles on the steady-state and time-resolved PL behaviour of CdTe/CdSe core–shell quantum dots (CSQDs). The QDs were dispersed in hexane (with appropriate optical density) and combined with TiO_2 suspensions, prepared across a concentration range from 0 to 30.7 mM.

Figure 5.5A and Figure 5.5B illustrate the steady-state PL spectra of CSQDs in response to increasing concentrations of TiO_2 nanoparticles and nanotubes, respectively. A consistent decrease in PL intensity was observed for both morphologies, with nanoparticles exhibiting more pronounced quenching efficiency than nanotubes. Importantly, the absorption spectra of these samples did not display significant scattering at longer wavelengths, as confirmed in Figure 5.6. Therefore, the decrease in PL intensity can be attributed to the interactions between CSQDs and TiO_2.

Time-resolved PL decay profiles (Figure 5.5C and Figure 5.5D) were recorded to further probe the interaction of CSQDs with nanoparticles and nanotubes, respectively. The PL decays profiles remain unchanged in the presence of quencher.

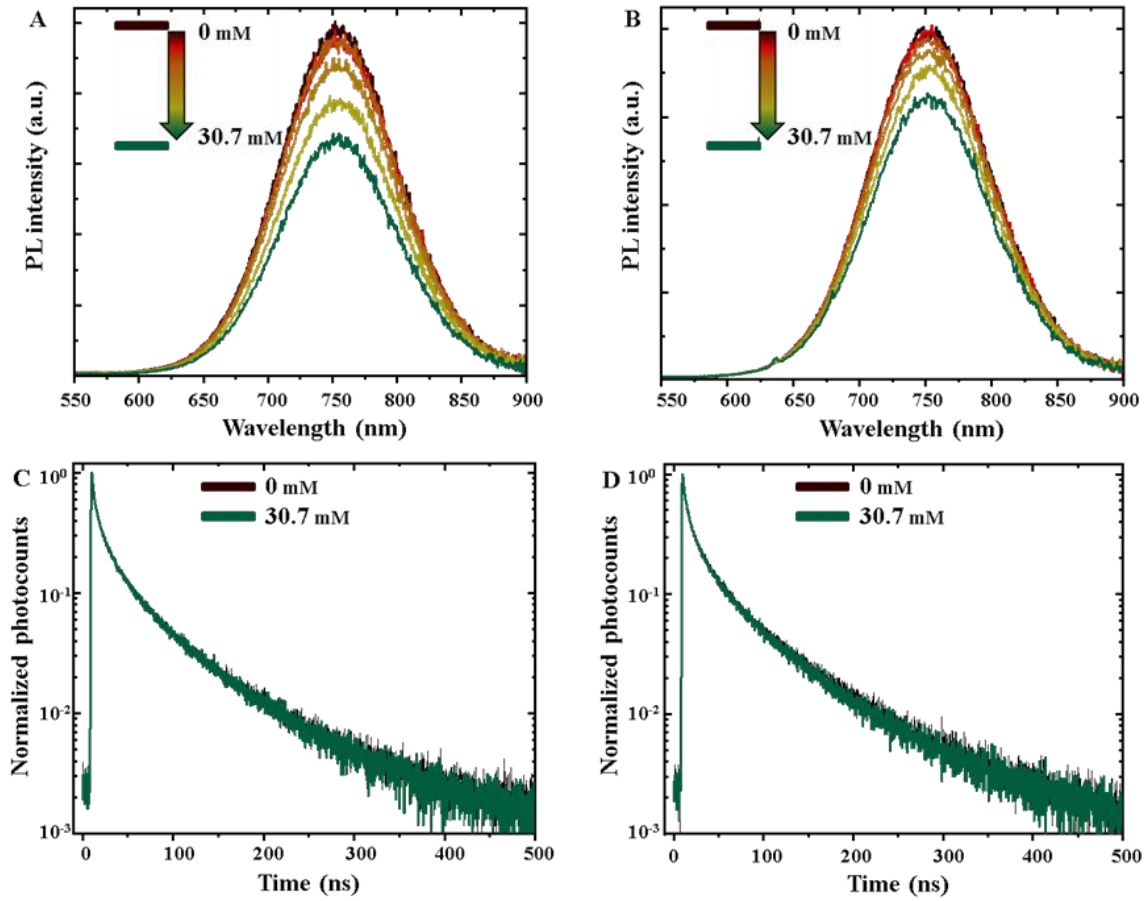

Figure 5.5) (A,B) PL spectra of CdTe-CdSe core-shell quantum dot structures upon increase in concentration of (A) nanoparticles and (B) nanotubes. And their corresponding PL decay lifetime

We attribute the quenching observed in steady-state PL primarily to interfacial charge transfer from the QDs to the TiO_2 nanostructures, enabled by type-II band alignment within the QDs and a cascade-like alignment between the QDs and TiO_2 (illustrated in the schematic, Figure 5.7A).

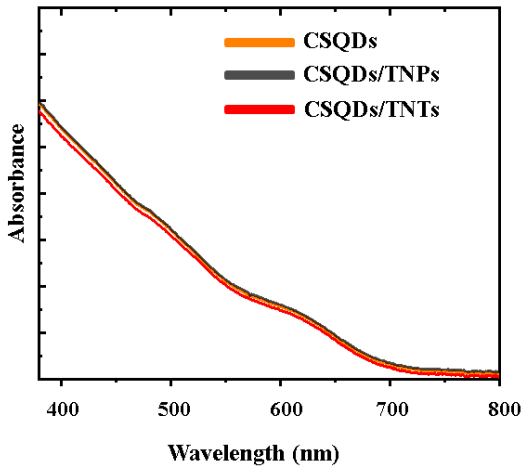

Figure 5.6) UV-Vis absorption spectra for CdTe-CdSe CSQDS before and after the addition of TNPs and TNTs

Figure 5.6 shows the absorption spectra before and after the addition of TiO_2 nanostructures to CdTe-CdSe CSQDs. The absence of scattering at higher wavelength confirms that the changes in optical response of the material is due to the synergistic effect.

To understand the nature of the quenching mechanism, Stern–Volmer (SV) plot was developed (Figure 5.7). The SV plot for TiO_2 nanoparticles exhibited a linear relationship across the concentration range,

characteristic of static quenching. This indicates the formation of non-emissive ground-state complexes between the QDs and TiO_2, leading to charge carrier suppression prior to excitation. The slope of the SV plot for nanotubes, while also indicative of static quenching, was lower than that of nanoparticles, suggesting comparatively reduced complexation efficiency despite the extended length and higher aspect ratio of the nanotubes.

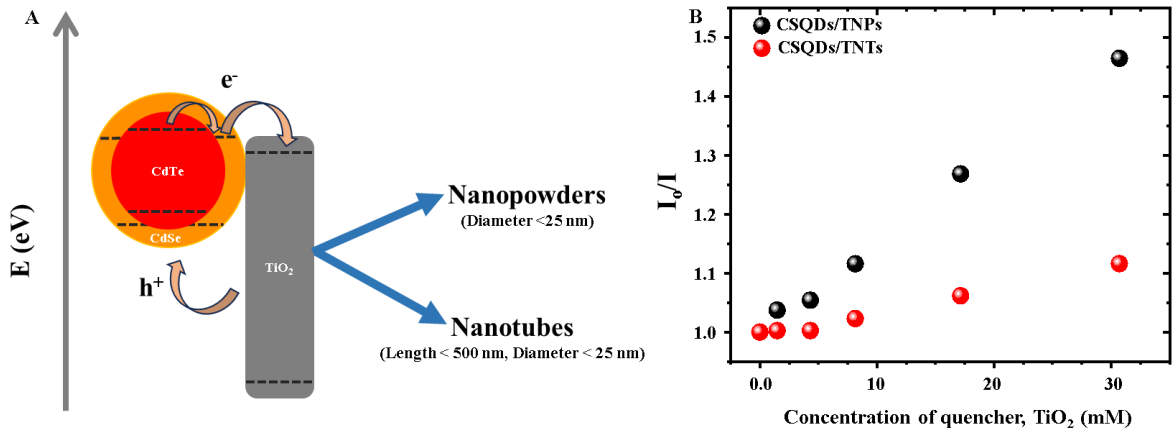

Figure 5.7) (A) Schematic representation of band alignment for CdTe-CdSe/TiO_2 heterostructures and (B) the Stern Volmer plot for the system

Literature suggests that static quenching dominates at lower quencher concentrations, while dynamic quenching becomes increasingly significant at higher concentrations[217]. Dynamic quenching involves collisional interactions between the quencher and excited fluorophore, leading to carrier extraction before radiative recombination occurs. This is typically manifested by shortened decay components and a positive deviation in the SV plot [151]. Overall, our data suggest that static quenching is the prevailing mechanism in the QD–TiO_2 system, with nanoparticles demonstrating superior quenching capability over nanotubes.

Interestingly, our previous findings involving perovskite nanocubes and TiO_2 nanoparticles indicated poor charge extraction in solution phase when long-chain ligands such as oleylamine and oleic acid were present[218]. In contrast, the current study demonstrates effective charge transfer from CSQDs capped with oleic acid to TiO_2 nanostructures. This difference could arise from several factors, including differences in driving force and electronic coupling between perovskite and II–VI semiconductor systems, distinct morphologies of CSQDs affecting surface ligand arrangements, and the effective interfacial contact area influenced by quencher size and dimensionality.

5.3.3.2 Thin film phase interactions

To evaluate the charge transfer interactions between core–shell quantum dots (CSQDs) and titanium dioxide (TiO_2) nanostructures in the absence of a liquid medium, a series of thin films were fabricated incorporating various configurations of these materials. Uniform thin films were prepared by spin-coating CdTe core QDs, CdTe/CdSe CSQDs, CSQDs combined with TiO_2 nanoparticles, and CSQDs with TiO_2 nanotubes onto glass substrates. Additionally, anodically grown TiO_2 nanotube arrays on titanium foils were employed as substrates, onto which the CSQDs were directly spin-coated and subsequently dried under ambient atmospheric conditions.

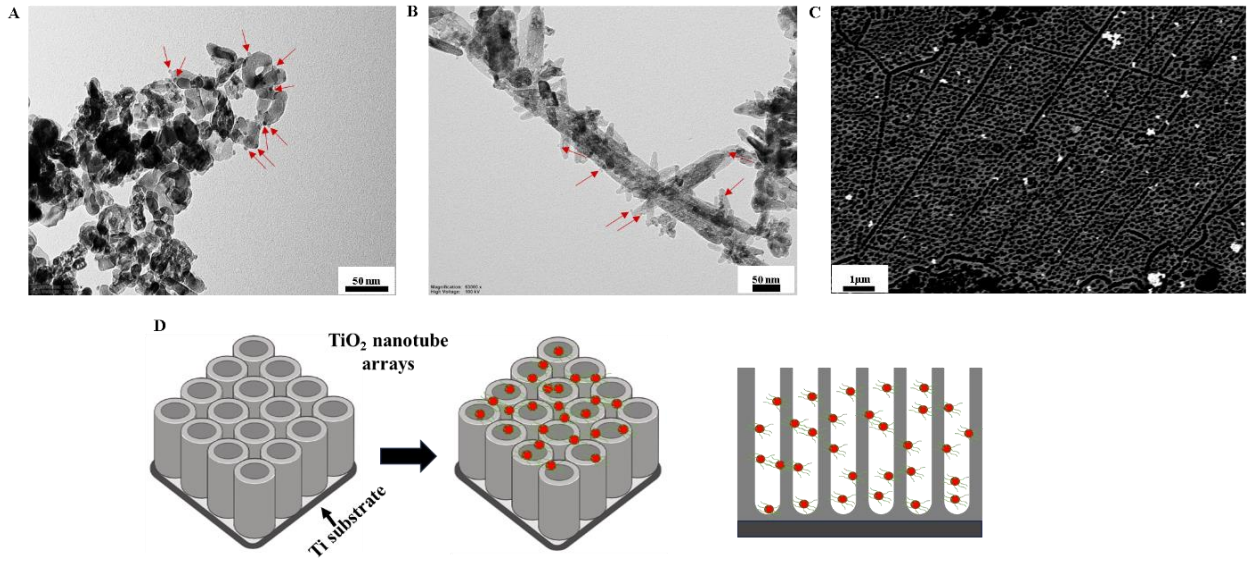

Figure 5.8 (A) TEM images of CdTe-CdSe/TNPs system (the red arrows point to CSQDs). (B) CdTe-CdSe/TNTs and (C,D) CdTe-CdSe/TNTAs system and its proposed cross section. The schematic is not according to scale

Figure 5.8 presents transmission electron microscopy (TEM) images of the CSQD–TiO_2 complexes, along with a SEM image and a schematic representation of the anodically grown TiO_2 nanotubes with CSQDs deposited on their surface. Figure 5.9 shows the structural and optical characterization of TiO_2 nanostructures.

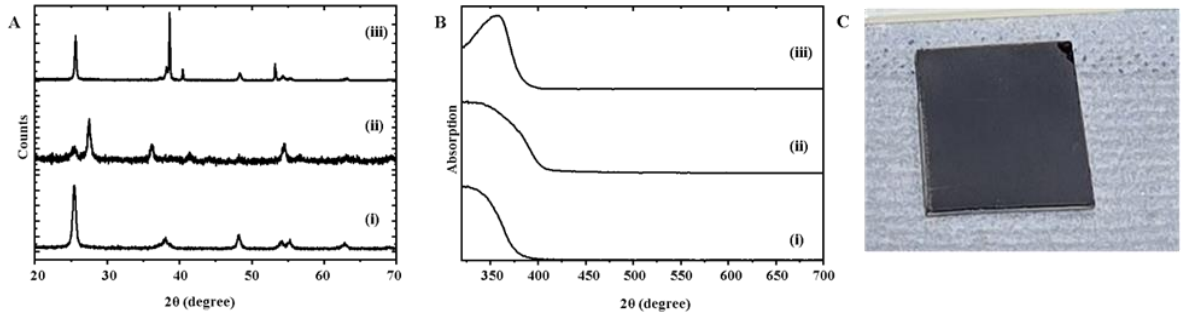

Figure 5.9) (A-C) XRD patterns (A) and UV-Vis absorption spectra (B) for (i) TNPs, (ii) TNTs (iii) TNTAs. Titania nanotubes arrays (TNTA) substrates are pictured (C)

In prior investigations, we explored the influence of surface ligands on the charge transfer behaviour of perovskite nanocubes interfaced with TiO_2 nanostructures. However, those systems lacked an intrinsic mechanism to prolong the excited-state lifetimes of charge carriers. In the present study, we specifically examine the quenching efficiency of TiO_2 nanostructures—distinguished by their diverse morphologies and size-dependent interfacial properties—under conditions that support extended carrier lifetimes, enabled by the type-II band alignment in CSQDs.

To resolve the spatial and temporal aspects of charge carrier dynamics in these thin-film systems, we employed confocal fluorescence lifetime imaging microscopy (FLIM). This technique enabled simultaneous measurement of fluorescence lifetimes and visualization of spatial heterogeneities within the film. The fluorescence decay curves were analysed by fitting to a tri-exponential decay function, from which the amplitude-weighted average lifetimes (τ_{avg}) were calculated.

5.3.3.2.1 FLIM measurements for thin films of CdTe QDs and CdTe-CdSe CSQDs

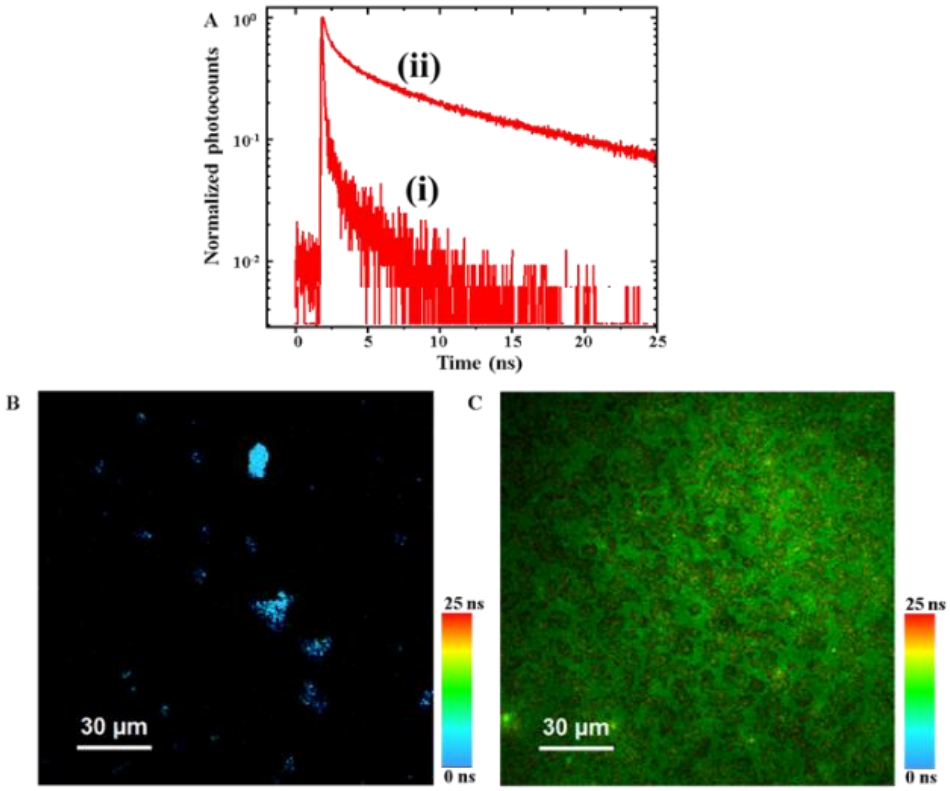

Figure 5.10) PL decay lifetime for thin films (A) (i) CdTe (ii) CdTe-CdSe core-shell quantum dot structures, and their corresponding FLIM images (B,C) respectively

Figure 5.10A display the time-resolved photoluminescence (TRPL) decay profiles for thin films of CdTe core QDs and CdTe/CdSe CSQDs, respectively, while the corresponding FLIM images are shown in Figure 5.10B and Figure 5.10C. Both materials exhibit significantly shorter lifetimes in the thin-film state compared to their solution-phase counterparts, which we attribute to enhanced carrier trapping at the film–substrate interface or within the QD film itself.

To ensure that the reading of TRPL lifetime obtained have minimum contributions from the instrument, we also show the instrument response functions in Figure 5.10A (dotted lines) corresponding to the readings acquired. The same data was used to produce the reconvolution fit.

Nonetheless, the CdTe/CdSe CSQDs exhibit a longer τ_{avg} than the CdTe core-only structures, consistent with the spatial separation of photo-generated electron–hole pairs facilitated by the type-II band alignment. This extended lifetime supports more efficient charge extraction pathways when interfaced with TiO_2 nanostructures, as investigated further in following sections

Table 5.2) PL lifetime components (τi) , corresponding fractional contribution(fi) of each decay time to the time resolved amplitude-weighted average PL lifetimes (τ) obtained from multiexponential fitting of PL decay profiles for thin films of CdTe and CdTe-CdSe CSQDs

	τ_1 (ns)	f_1	τ_2 (ns)	f_2	τ_3 (ns)	f_3	χ^2	τ_{Avg} (ns)
CdTe	0.09 ± 0.0043	0.92 ± 0.015	0.73 ± 0.12	0.07 ± 0.012	4.50 ± 0.24	0.02 ± 0.0019	1.01	0.2 ± 0.0081
CdTe-CdSe CSQDs	0.31 ± 0.006	0.44 ± 0.0035	2.10 ± 0.031	0.28 ± 0.0031	14.70 ± 0.08	0.28 ± 0.0019	1.347	4.8 ± 0.051

As shown in Table 5.2, upon the growth of a CdSe shell around the CdTe core, all three PL lifetime components τ_1, τ_2, and τ_3 exhibit an increase, resulting in a substantial enhancement of the average PL lifetime (τ_{avg}), which increases by a factor of approximately 21. In the bare CdTe core quantum dots (QDs), the PL decay is primarily governed by two fast components: τ_1 = 0.09 ns, contributing

approximately 92% to the total decay, and τ_2 = 0.73 ns, contributing around 7%. The long-lived component, τ_3 = 4.5 ns, represents less than 2% of the total decay, indicating its minor role in the overall recombination dynamics.

The lifetime component τ_1 = 0.09 ns can be a result of charge hopping among the closely packed CdTe QDs or trap assisted recombination.

The non-radiative recombination through defect states and surface traps can occur on timescales significantly faster than radiative recombination, particularly in II–VI semiconductor nanocrystals [219]. Given the inherently unstable nature of CdTe QDs, these structures are prone to the formation of surface defects over time, which give rise to additional non-radiative recombination pathways. Consequently, the decay component τ_2 is attributed to trap-assisted non-radiative recombination processes, likely corresponding to recombination from deep trap states that exclusively favour non-radiative pathways [220], [221].

The longer τ_3 component is associated with radiative band-edge recombination, which becomes prominent only after partial or full saturation of available trap states. Carriers in shallow trap states may undergo either slow de-trapping followed by radiative recombination at the B.E or direct non-radiative recombination. Therefore, τ_3 captures contributions from both mechanisms. This enables transient carrier trapping followed by rapid de-trapping into the conduction band, leading to delayed radiative emission. Overall, for the CdTe core QDs, the calculated amplitude-weighted average lifetime (τ_{avg}) is approximately 0.2 ns, emphasizing the dominant influence of ultrafast non-radiative decay processes mediated by trap states. The overcoating of a CdSe shell around the CdTe quantum dot (QD) core leads to significant modification of both the electronic band structure and surface trap landscape, resulting in enhancement of the average PL lifetime (τ_{avg}), which increases to 4.8 ns. This improvement is attributed to the formation of a type-II band alignment between the core and shell materials, as well as to effective passivation of surface trap states.

Specifically, the previously dominant τ_1 component slows down from 0.09 ns to 0.32 ns, with its relative contribution declining markedly from 92% to 44%. In contrast, the longer-lived decay components, τ_2 and τ_3, are substantially prolonged— τ_2 increases to 2.1 ns and τ_3 to 14.7 ns. Notably, the relative contributions of these components increase to 28% each, indicating their greater influence in the recombination dynamics of the core/shell system.

This redistribution of lifetime components and the extension of individual decay times indicate several key physical processes:

(i) Passivation of trap states – Prolonged lifetime and reduction in the relative contribution of the fast non-radiative components suggests that the CdSe shell effectively passivates defect states at or near the CdTe surface, thereby mitigating trap-mediated recombination.

(ii) Efficient de-trapping of carriers – The increased lifetime and contribution of τ_1 and τ_3 imply that carriers localized in shallow traps are more likely to be thermally or quantum-mechanically detrapped into the conduction band (CB) of CdTe and CdSe, increasing their probability for radiative recombination. Here we ascribe τ_1 and τ_3 to B.E radiative recombination in of CdTe and CdSe, respectively.

(iii) Interfacial carrier transfer – The type-II band alignment facilitates spatial separation of charge carriers, with electrons potentially transferring from the CB of CdTe to the CB of CdSe. Once transferred, these carriers may either recombine radiatively across the type-II interface or relax back into the CdTe valence band (VB) through intermediate states. The τ_2 component might represent the internal separation of charge carriers as it lies in the time domain.

Overall, the presence of the CdSe shell introduces additional recombination pathways while simultaneously suppressing non-radiative trap states, thereby favouring radiative recombination mechanisms and extending carrier lifetimes. These findings underscore the role of shell-induced

electronic structure modification and trap-state engineering in improving the optoelectronic performance of II–VI semiconductor core/shell nanocrystals.

5.3.3.2.2 FLIM measurements for thin films of CdTe-CdSe/TiO_2 nanoheterostructures

The incorporation of titanium dioxide (TiO_2) into the CdTe/CdSe core/shell quantum dot (CSQD) system induces significant quenching in the PL lifetime, attributable to efficient charge transfer from the CSQDs to TiO_2. Time-resolved photoluminescence (TRPL) measurements and corresponding fluorescence lifetime imaging microscopy (FLIM) images of the CSQD–TiO_2 complexes are shown in Figure 5.11.

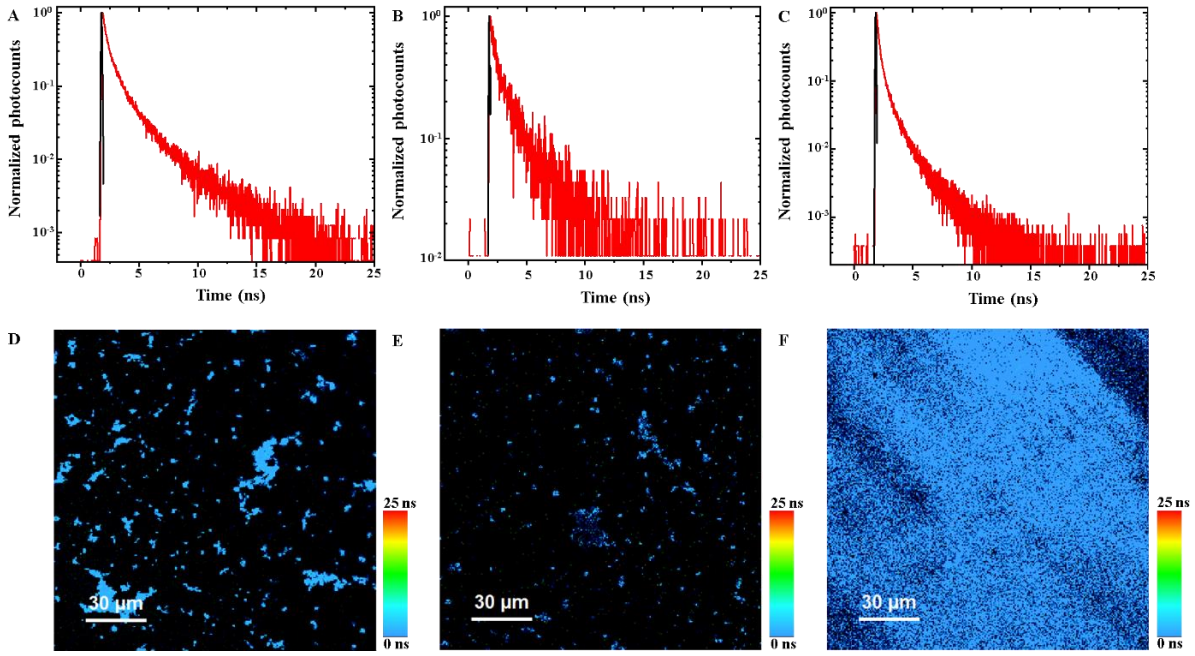

Figure 5.11) (A-C) PL decay lifetime for (A) CdTe-CdSe/TNPs, (B) CdTe-CdSe/TNTs, (C) CdTe-CdSe/TNTAs (the black lines show the instrument response function) and their respective FLIM images (D-F). The scale bar for FLIM images is 30 µm

Table 5.3 summarizes the extracted decay parameters of nanocomposite system thin films.

Table 5.3) Lifetime components and the corresponding relative contributions of CdTe-CdSe CSQDs after incorporation of TiO_2. The rate of charge transfer is based on average lifetime value.

	τ_1 (ns)	f_1	τ_2 (ns)	f_2	τ_3 (ns)	f_3	χ^2	τ_{Avg} (ns)	K_{ET} (ns^{-1})
CSQDs/TNP	0.24 ± 0.0071	0.67 ± 0.014	1.00 ± 0.03	0.27 ± 0.012	3.40 ± 0.15	0.04 ± 0.0031	1.1790	0.6 ± 0.0063	1.46
CSQDs/TNT	0.38 ± 0.047	0.59 ± 0.004	1.60 ± 0.2	0.40 ± 0.1	5.60 ± 0.55	0.04 ± 0.023	1.320	1.1 ± 0.11	0.7
CSQDs/TNTA	0.16 ± 0.003	0.80 ± 0.0063	0.67 ± 0.014	0.18 ± 0.0054	2.38 ± 0.052	0.02 ± 0.001	1.081	0.3 ± 0.0014	3.13

Upon introduction of TiO_2 nanoparticles to CSQD thin films, the average lifetime (τ_{avg}) drastically decreases from 4.8 ns to 0.6 ns (600 ps). The individual lifetime components also contract, τ_1 decreases from 0.31 ns to 0.21 ns, τ_2 from 2.1 ns to 1.0 ns and τ_3 from 15 ns to 3.4 ns. Additionally, the relative amplitude contribution of τ_1 increases from 44% to 68%, τ_2 remains essentially constant, while τ_3 drops sharply from 27% to 4%.

The reduction in τ_3 and its fractional contribution indicates that radiative recombination is being significantly suppressed due to ultrafast charge extraction by the TiO_2 nanoparticles, which competes with B.E recombination processes from the conduction band (CB) of CdSe. The reduction in τ_1 and increase in its relative contribution suggest that charge separation process has become more efficient

and prominent as compared to pristine CSQDs, due to quenching of charges from CdTe CB. The lifetime component τ_2 becomes faster and its relative contribution remains unchanged. This can be associated with TiO_2 competing with trap assisted recombination of charge carriers from shallow traps near to CB of CdTe, hence the increase in relative contribution for τ_1. Additionally, TiO_2 may introduce new non-radiative decay channels by altering the trap-state distribution at the CSQD interface. It is important to note that since the TRPL signals were recorded through a 440 nm optical filter, therefore TiO_2 does not get excited and the carrier recombination processes within the TiO_2 cannot be taken into account.

The CSQD–TiO_2 nanotube (TNT) complexes exhibit particular decay behaviour. For these samples, τ_1 increases slightly to 0.38 ns with a higher relative contribution of 59%. The τ_2 component decreases to 1.6 ns, and its contribution increases to 40%. While τ_3 reduces to 5.6 ns with a relative contribution of only 4%. The τ_{avg} in this case is 1.1 ns. These trends suggest that the TNTs show the same mechanism of quenching as TNPs but are less effective in suppressing the radiative recombination from CdTe CB but nonetheless, they still promote quenching.

When CSQDs are spin-coated directly onto anodically grown TNTAs, a further reduction in all three lifetime components is observed. Specifically, τ_1 falls to 0.16 ns, τ_2 to 0.6 ns, and τ_3 to 2.38 ns with relative contributions of 80%, 18%, and 2%, respectively. The τ_{avg} decreases further to 0.3 ns (300 ps), indicating more pronounced quenching compared to both TiO_2 nanoparticles and free-standing TNTs. It indicates that TNTAs are most efficient at quenching the charge carriers from CdSe shell and as well as from CdTe CB (radiative recombination). In addition, the charge carrier separation process becomes more efficient and dominant in the presence of TNTAs. The more severe quenching effect observed for the CSQDs/TNTA system, compared to CSQD/TNPs, is attributed to the morphological and interfacial advantages of the TNTAs. Figure 5.12 shows the EDS colour mapping for CSQDs/TNTA system. Considering much smaller size of CSQDs compared to the diameter of the TNTAs, we believe that CSQDs are able to penetrate into the nanotubes and develop better surface contact.

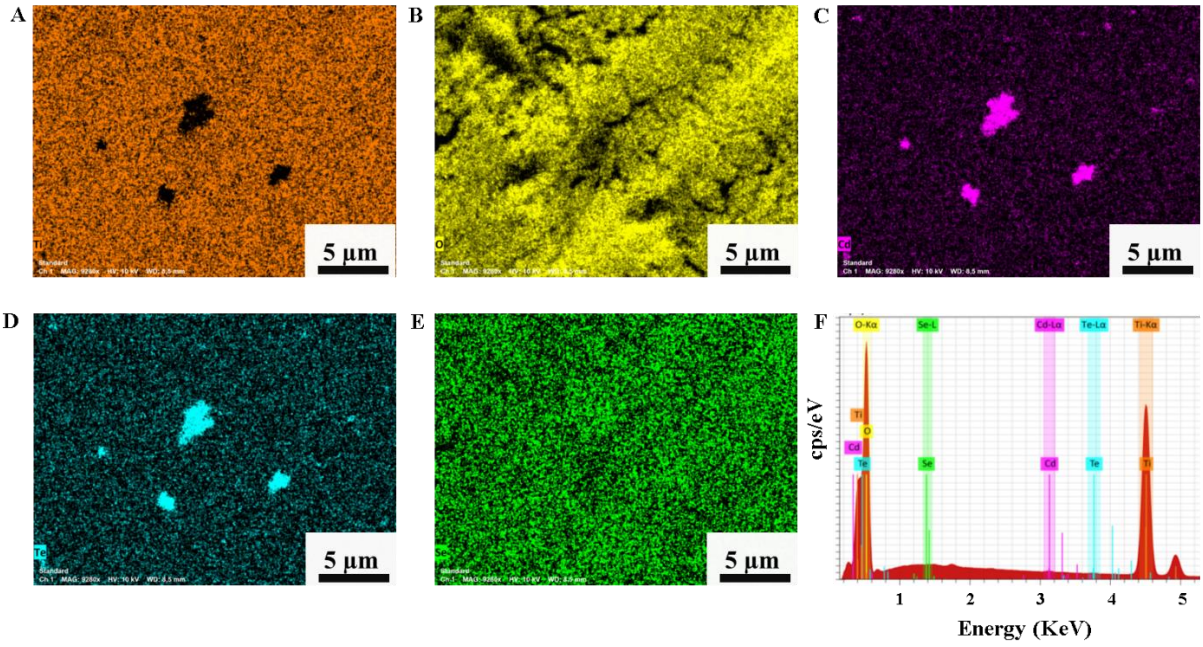

Figure 5.12) (A-E) EDS colour mapping for CSQDS/TNTA heterostructures A) Titanium, B) Oxygen, C) Cadmium, D) Tellurium and E) Selenium and (F) the corresponding spectra

Table 5.4) Quantitative analysis of EDS data shown in figure 5.15

Elements	At. No	Mass (%)	Mass Normalized (%)	Atom (%)	Absolute error (%) (1 sigma)	Relative error (%) (1 sigma)
Oxygen	8	37.9	41.4	67.9	41	10.5
Titanium	22	53.3	58.2	31.9	1.8	3.4
Selenium	34	0.12	0.12	0.04	0.03	30.5
Cadmium	48	0.16	0.17	0.04	0.04	24.9
Tellurium	52	0.11	0.11	0.02	0.04	43.1

The ligand-free surface of the TNTAs offers superior electronic coupling and physical contact area for the CSQDs, enhancing interfacial charge transfer. Moreover, the dimensional difference between the <6 nm CSQDs and the >150 nm TNTA pore openings suggests that QDs can infiltrate the tubular structure and adhere to the inner walls, significantly increasing the effective contact area. The energy-dispersive X-ray spectroscopy (EDS) mapping is shown in (Figure 5.12), it shows the distribution of Cd, Te, and Se within the TNTAs. In conclusion, the TNTA configuration outperforms both TiO_2 nanoparticles and nanotubes in terms of charge carrier quenching efficiency. This superior performance is ascribed to enhanced contact area, better surface interaction, and increased likelihood of QD internalization. These properties render the CSQD/TNTA architecture particularly promising for applications in liquid-phase photocatalysis, where solid-supported quenchers offer practical advantages in terms of separation and recovery over dispersed nanoparticles.

The apparent rate constants for charge transfer, calculated using equation 3-4, are estimates, as they are derived from differences in the reciprocals of intensity-weighted average lifetimes obtained from multiexponential fits, rather than from monoexponential lifetimes. A major fraction of the charge injection process occurs with a higher rate constant when considering only the fast component of the emission decay. For example, approximately 80% of the emission decay of CdTe-CdSe CSQDs on a TNTAs surface occurs with a lifetime of 0.16 ns, indicating that the majority of the charge injection takes place on an ultrafast timescale. Kamat et al. reported that the difference in conduction band positions between CdTe and TiO_2 contributes to the high-rate constant observed for charge transfer. The Table 5.5 shows the reported values for rate of charge transfer from Cd based core and coreshell quantum dots to TiO_2.

Table 5.5) comparison of reported values for rate of electron transfer from core and core-shell II-VI semiconductor to TiO_2

Material	Size	Acceptor	Configuration	K_{ET} (ns^{-1})	Reference
CdSe/ZnS CSQDs	3.6 nm 4.6 nm 6.4 nm	TNPs	Thin films on glass substrate	0.013 0.006 0.0047	[222]
CdSe/ZnS CSQDs	-	TNPs	-	0.03	[223]
CdSe/CdS CSQDs CdS/CdSe CSQDs CdSe QDs	2.9 nm 3.3 nm 2.2 nm 2.6 nm 1.7 nm	TNPs	Thin films on fluoride doped tin oxide	0.11 0.081 0.31 0.36 0.20	[224]
CdSe QDs	-	TNPs	-	0.1-0.3	[225]

CdSe/ZnS CSQDs				0.1-0.3	
CdSe QDs	-	TiO_2	-	$\sim 10^7$	[226]
CdTe	2.5nm 3 nm 3.5 nm 4 nm	TNPs	Thin films	0.30 0.28 0.05 0.009	[227]
CdTe-CdSe CSQDs	5.3 nm	TNPs TNTs TNTAs	Thin films Thin films Thin films	1.46 0.7 3.13	This work

By comparing the values of K_{ET} obtained from this study with the ones reported in the literature, three key conclusions can be drawn

- CdTe-CdSe CSQDs outperform other combinations of CSQDs for charge injection to TiO_2.
- Nanostructured TNTAs substrate performs better as a quencher when compared to conventional TiO_2 thin film substrates.
- Based on the Figure 5.3A (CdTe QDs size calculation using TEM analysis), section 5.3.2 (using peng's formula to calculate CdTe QDs size using absorption peak), Table 5.2 (less relative contribution for radiative contribution from CdTe thin films) and K_{ET} for 3.5 nm CdTe QDs to TiO_2, reported by Lekha et al [227] , we can deduce better performance of CdTe-CdSe CSQDs compared to CdTe QDs. Furthermore, the unstable nature and surface traps of CdTe core render them as less desirable candidates for photocatalytic applications.

These findings underscore the critical role of TiO_2 morphology in modifying electron transfer dynamics in QD-based hybrid systems. The enhancement in charge extraction with TNTAs, makes them a more promising architecture for optoelectronic applications such as photovoltaics and photocatalysis where efficient donor-acceptor interactions are essential.

Finally, to verify the synergistic effect in CSQDs/TNTAs nanocomposites, photocatalytic degradation of aqueous RhB was carried out under UV light irradiation. Figure 5.13 shows the experimental setup for dye degradation; observed PL decay and specific rate constants are plotted in Figure 5.14.

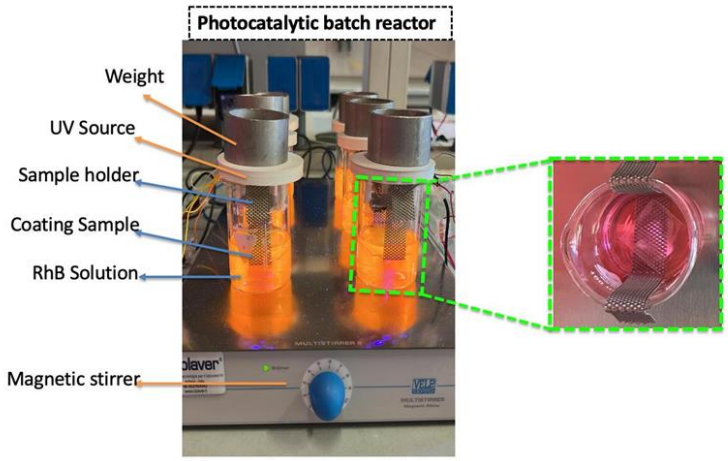

Operating Conditions	
Volume of RhB	40 mL
Testing duration	6 hours
Measurement repetition	1 h
Coatings distance from UV source	3 cm
Maximum absorbance of RhB	555 nm (Visible Region)
UV wavelength (λ)	365 nm
UV intensity	14.5 mW.cm^{-2}

Figure 5.13) Photocatalytic setup for dye degradation and the operating conditions

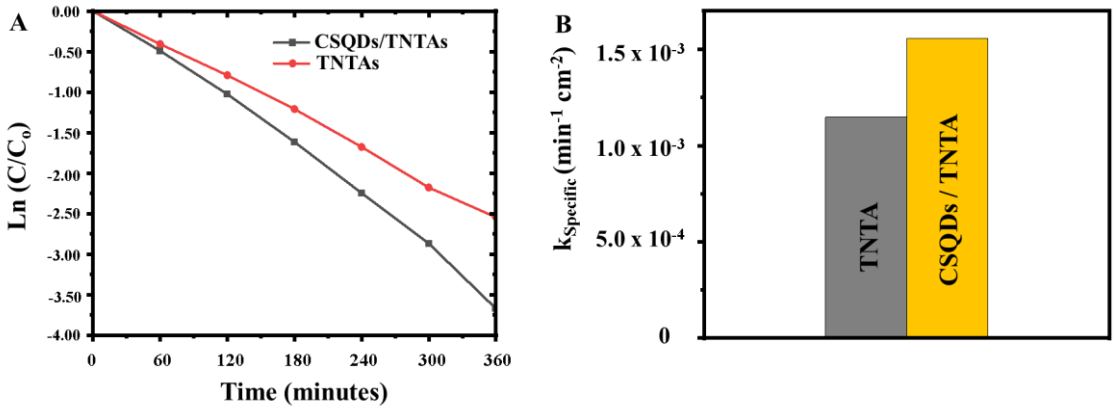

Figure 5.14) (A) The decay curves and (B) specific rate constants for pristine and CSQDs loaded TNTA during RhB degradation

A 36% increase in photocatalytic activity for CSQDs loaded TNTAs is observed. The photocatalytic performance of these nanoheterostructures also depends on the concentration of QDs loaded on the TNTAs [228]. Therefore, the photocatalytic output can be further tuned by varying the concentration of loaded CSQDs on the TNTAs.

5.4 Summary

To investigate the influence of TiO_2 morphology on charge transfer processes from CdTe/CdSe core–shell quantum dots (QDs), we systematically investigated their photophysical interactions with TiO_2 in both colloidal (solution) and solid-state (thin-film) configurations. Two types of TiO_2 architectures, nanoparticulate (TNPs) and one-dimensional nanotubes (TNTs), were employed to explore morphology-dependent electron extraction efficiency.

- In solution-phase studies, CdTe/CdSe QDs were dispersed with TiO_2 nanostructures in a non-polar solvent to assess their donor-acceptor interactions via photoluminescence quenching and lifetime analysis. Notably, the QDs exhibited more pronounced quenching behaviour when combined with TiO_2 nanoparticles compared to nanotubes. This suggests that the extended one-dimensional geometry and higher surface area of TNTs do not facilitate efficient interfacial contact and electron injection pathways. Time-resolved PL measurements confirmed accelerated carrier extraction in the presence of TNPs, with PL decreasing significantly relative to the QDs alone, indicative of enhanced charge transfer.

- In contrast, when transferred into the solid-state via spin-coating onto substrates, both TiO_2 morphologies induced additional photoluminescence quenching, though with distinct differences. Thin films containing QDs interfaced with TNTAs continued to exhibit superior quenching efficiency and reduced recombination lifetimes, further supporting the hypothesis that anisotropic morphology offers favourable pathways for directional charge transfer. Comparatively, TNPs and TNTs showed moderately slower quenching effects, likely limited by interfacial contact area and aggregation-induced recombination pathways.

5.5 Future outlook

As demonstrated, the CSQDs perform relatively better role in terms of acting as sensitizers for TNTAs, on comparison with TNPs and TNTs. Another configuration of TNTAs is ‘self-standing TNTAs’, where after the growth of TNTAs, they are detached from the surface of the Ti substrate (free-standing

membranes). This allows the nanotubular structures to have higher exposed surface area and dynamic interaction with the CSQDs. It could be interesting

- To grow the TNTAs in the presence of CSQDs as ligands for better surface coverage and interfacial contact.
- To synthesize the QDs in the presence of free-standing membranes

6 Summary, conclusions and future work

This thesis systematically explored the role of nanomaterial morphology, phase structure, surface chemistry, and interface engineering in optimizing charge transfer dynamics which could be essential for efficient photocatalytic hydrogen evolution. The collective findings provide valuable insights for designing advanced nanostructured materials for energy-related applications.

In Chapter 2, the influence of TiO_2 morphology on hydrogen evolution reaction (HER) performance was established. The results demonstrated that anatase-phase TiO_2 nanotube arrays (TNTAs), particularly with an optimized height of 8 μm, exhibited superior HER activity compared to nanoparticles. This highlights the critical role of morphology in tuning electronic properties and charge carrier dynamics.

Chapter 3 investigated the impact of ligand chain length on interfacial charge transfer between $CsPbBr_3$ PNCs and TiO_2 nanostructures. Short-chain ligand-modified PNCs exhibited enhanced electronic coupling and more effective charge transfer to TiO_2, with morphology-dependent effects being especially pronounced in solid-state configurations involving nanotube arrays. These results demonstrate the importance of both surface chemistry and TiO_2 architecture in determining interfacial behaviour.

Chapter 4 extended this analysis to Mn-doped perovskite systems, revealing that quenching mechanisms in liquid and thin-film phases are sensitive to both TiO_2 morphology and film configuration. While promising heterostructures can be engineered by fine-tuning these parameters, further ultrafast spectroscopic studies are required to fully understand the charge carrier dynamics in these systems.

In Chapter 5, CdTe/CdSe core–shell quantum dots interfaced with TiO_2 were studied. It was found that in solution, TiO_2 nanoparticles facilitated more efficient charge extraction than nanotubes, while in thin films, TNTAs promoted superior quenching and charge transfer, likely due to improved morphology and interfacial contact. Finally, the existence of synergetic effect in CdTe-CdSe core-shell quantum dots/TNTAs is demonstrated through photocatalytic dye degradation of aqueous Rhodamine B.

Collectively, this work demonstrates that the interplay between nanomaterial morphology, phase, and surface chemistry is critical to optimizing photocatalytic and charge transfer processes. These insights pave the way for the rational design of nanostructured hybrid materials with enhanced performance in photocatalytic and optoelectronic applications.

Building on the findings of this thesis, we propose the following future work:

1. Advanced Spectroscopic Analysis To gain deeper insights into the ultrafast dynamics of charge carriers in perovskite/TiO_2 and core–shell/TiO_2 heterostructures, time-resolved spectroscopy techniques such as femtosecond pump-probe spectroscopy could be employed. Such tools allow for a more precise understanding of charge separation, recombination, and transfer processes at the interface.
2. Improved Surface Engineering of Perovskite Nanocrystals While short-chain ligand exchange has shown promising improvements in charge transfer, further optimization of surface passivation strategies is needed to enhance stability and minimize

nonradiative losses. The use of ligands which could balance electronic coupling with material stability could be beneficial.

3. Wavefunction engineering and charge transfer Engineering of wavefunctions in core–shell quantum dot (CSQD) structures, for a given core material, is primarily determined by the shell's composition and thickness. A detailed investigation of how these parameters influence charge transfer from CSQDs to TiO_2 nanostructures can provide valuable insights for material selection and optimizing device performance.
4. Stability and Scalability Studies Given the limitations in long-term environmental stability of perovskite materials, particularly under operational conditions, future efforts should focus on improving material robustness through encapsulation, doping, or protective interfacial layers. In addition, scaling the optimized nanostructures for practical device integration should be investigated.
5. Exploration of Alternative Semiconductor Systems To overcome the intrinsic limitations of perovskite materials, future studies should explore more stable perovskite-inspired compounds or Zinc based semiconductor nanostructures. This could open pathways toward developing high-performance, stable hybrid photocatalysts. Especially, exploring the two-photon absorption can broaden the range solar energy harvesting.

By pursuing these directions, future research can build on the fundamental understanding established in this thesis and contribute to the advancement of high-efficiency, stable nanomaterial-based systems for sustainable energy applications.

References

[1] M. Nasrollahzadeh, S. M. Sajadi, M. Sajjadi, and Z. Issaabadi, 'An Introduction to Nanotechnology', *Interface Sci. Technol.*, pp. 1-27, 2019.

[2] B. Mekuye and B. Abera, 'Nanomaterials: An overview of synthesis, classification, characterization, and applications', in *Nanoselect*, 2023, pp. 486-501,.

[3] J. ALTMANN, 'Military Uses of Nanotechnology: Perspectives and Concerns', *Sage Publ. Ltd*, vol. 35, no. 1, pp. 61-79, 2004.

[4] Frank Babick, Johannes Mielke, Wendel Wohlleben, Stefan Weigel, and Vasile-Dan Hodoroaba, 'How reliably can a material be classified as a nanomaterial? Available particle-sizing techniques at work', *J. Nanoparticle Res.*, vol. 18, no. 158, 2016.

[5] E. Comission, 'Nanomaterials-Internal Market, Industry, Entrepreneurship and SMEs', *Eur. Com.*, 2025, [Online]. Available: https://single-market-economy.ec.europa.eu/sectors/chemicals/reach/nanomaterials_en.

[6] S. L. Altmann, *Band Theory of Solids An Introduction from the Point of View of Symmetry*. Oxford University Press, 2023.

[7] S. Ghimire and V. Biju, 'Relations of exciton dynamics in quantum dots to photoluminescence, lasing, and energy harvesting', *J. Photochem. Photobiol. C Photochem. Rev.*, vol. 34, pp. 137-151, 2018.

[8] O. Gençer, *Zinc (Zn) Doped Carbon (C) Based Quantum Dot (QD) Synthesis & Characterization*. Istanbul Technical University, 2021.

[9] J. Cassidy and M. Zamkov, 'Nanoshell quantum dots: Quantum confinement beyond the exciton Bohr radius', *J. Chem. Phys.*, vol. 152, no. 11, 2020.

[10] J. M. Coronado, F. Fresno, M. D. Hernández-Alonso, and R. Portela, *Design of Advanced Photocatalytic Materials for Energy and Environmental Applications*. London: Springer, 2013.

[11] S. V. Gaponenko and H. V. Demir, 'Quantum confinement effects in semiconductors', in *Applied Nanophotonics*, Cambridge University Press, 2018.

[12] S. Mannar, P. Mandal, A. Roy, and R. Viswanatha, 'Experimental Determination of the Molar Absorption Coefficient of Cesium Lead Halide Perovskite Quantum Dots', *J. Phys. Chem. Lett.*, vol. 13, no. 27, 2022.

[13] M. C. Brennan, J. Zinna, and M. Kuno, 'Existence of a Size-Dependent Stokes Shift in CsPbBr3 Perovskite Nanocrystals', *ACS Energy Lett.*, vol. 2, no. 7, pp. 1487-1488, 2017.

[14] A. N. Goldstein, C. M. Echer, and A. P. Alivisatos, 'Melting in Semiconductor Nanocrystals', *Science*, vol. 256, no. 5062, pp. 1425-1427, 1992.

[15] Yiming Zhao, 'Quantum Dots and Doped Nanocrystals: Synthesis, Optical Properties, and Bio-applications', 2013, doi: 10.13140/RG.2.2.32338.15047.

[16] S. Taylor-Harry and M. Adekanmbi, 'CONFINEMENT ENERGY OF QUANTUM DOTS AND THE BRUS EQUATION', *Int. J. Res.*, vol. 8, no. 11, pp. 318-323, 2020.

[17] G.-H. Chen, P.-H. Chen, C.-T. Lin, T.-W. Jang, P. Yang, and H.-S. Chen, 'Enhanced Photostability of Core/Shell Quantum Dots under Intense Blue Light Irradiation through Positive Photoaging Mechanism', *ACS Appl. Mater. Interfaces*, vol. 15, no. 45, 2023.

[18] A. Kipkorir, J. DuBose, J. Cho, and P. V. Kamatabe, 'CsPbBr3–CdS heterostructure: stabilizing perovskite nanocrystals for photocatalysis', *Chem. Sci.*, no. 44, 2021.

[19] C. B. Murray, D. J. Norris, and M. G. Bawendi, 'Synthesis and characterization of nearly monodisperse CdE (E = sulfur, selenium, tellurium) semiconductor nanocrystallites', *J. Am. Chem. Soc.*, vol. 115, no. 19, 1993.

[20] J. J. Li *et al.*, ‘arge-Scale Synthesis of Nearly Monodisperse CdSe/CdS Core/Shell Nanocrystals Using Air-Stable Reagents via Successive Ion Layer Adsorption and Reaction’, *J. Am. Chem. Soc.*, vol. 125, no. 41, pp. 12567-12575, 2003.

[21] C. B. Murray, C. R. Kagan, and M. G. Bawendi, ‘Synthesis and Characterization of Monodisperse Nanocrystals and Close-Packed Nanocrystal Assemblies’, *Annu. Rev. Mater. Res.*, vol. 30, pp. 545-610, 2000.

[22] N. Liu, C. Schneider, D. Freitag, E. M. Zolnhofer, K. Meyer, and P. Schmuki, ‘Noble-Metal-Free Photocatalytic H_2 Generation: Active and Inactive “Black” TiO_2 Nanotubes and Synergistic Effects’, *Chem. – Eur. J.*, vol. 22, no. 39, pp. 13810–13814, Sep. 2016, doi: 10.1002/chem.201602714.

[23] A. Raes, R. Ninakanti, L. Van Den Bergh, R. Borah, S. Van Doorslaer, and S. W. Verbruggen, ‘Black titania by sonochemistry: A critical evaluation of existing methods’, *Ultrason. Sonochem.*, vol. 100, p. 106601, Nov. 2023, doi: 10.1016/j.ultsonch.2023.106601.

[24] H. Huang, B. Pradhan, J. Hofkens, M. B. J. Roeffaers, and J. A. Steele, ‘Solar-Driven Metal Halide Perovskite Photocatalysis: Design, Stability, and Performance’, *ACS Energy Lett.*, vol. 5, no. 4, pp. 1107–1123, Apr. 2020, doi: 10.1021/acsenergylett.0c00058.

[25] A. J. Haider, Z. N. Jameel, and I. H. M. Al-Hussaini, ‘Review on: Titanium Dioxide Applications’, *Energy Procedia*, vol. 157, pp. 17–29, Jan. 2019, doi: 10.1016/j.egypro.2018.11.159.

[26] Q. Guo, C. Zhou, Z. Ma, and X. Yang, ‘Fundamentals of TiO_2 Photocatalysis: Concepts, Mechanisms, and Challenges’, *Adv. Mater.*, vol. 31, no. 50, p. 1901997, Dec. 2019, doi: 10.1002/adma.201901997.

[27] Z. Li, Z. Li, C. Zuo, and X. Fang, ‘Application of Nanostructured TiO_2 in UV Photodetectors: A Review’, *Adv. Mater.*, vol. 34, no. 28, p. 2109083, Jul. 2022, doi: 10.1002/adma.202109083.

[28] Y. Chen *et al.*, ‘Facet-engineered TiO2 drives photocatalytic activity and stability of supported noble metal clusters during H2 evolution’, *Nat. Commun.*, vol. 14, no. 1, p. 6165, Oct. 2023, doi: 10.1038/s41467-023-41976-2.

[29] D. Chen *et al.*, ‘Photocatalytic degradation of organic pollutants using TiO2-based photocatalysts: A review’, *J. Clean. Prod.*, vol. 268, p. 121725, Sep. 2020, doi: 10.1016/j.jclepro.2020.121725.

[30] R. Qian *et al.*, ‘Charge carrier trapping, recombination and transfer during TiO2 photocatalysis: An overview’, *Catal. Today*, vol. 335, pp. 78–90, Sep. 2019, doi: 10.1016/j.cattod.2018.10.053.

[31] Y. Tamaki, K. Hara, R. Katoh, M. Tachiya, and A. Furube, ‘Femtosecond Visible-to-IR Spectroscopy of TiO_2 Nanocrystalline Films: Elucidation of the Electron Mobility before Deep Trapping’, *J. Phys. Chem. C*, vol. 113, no. 27, pp. 11741–11746, Jul. 2009, doi: 10.1021/jp901833j.

[32] O. E. Dagdeviren *et al.*, ‘The Effect of Photoinduced Surface Oxygen Vacancies on the Charge Carrier Dynamics in TiO_2 Films’, *Nano Lett.*, vol. 21, no. 19, pp. 8348–8354, Oct. 2021, doi: 10.1021/acs.nanolett.1c02853.

[33] D. Wrana *et al.*, ‘Photoluminescence imaging of defects in TiO2: The influence of grain boundaries and doping on charge carrier dynamics’, *Appl. Surf. Sci.*, vol. 569, p. 150909, Dec. 2021, doi: 10.1016/j.apsusc.2021.150909.

[34] N. Jin *et al.*, ‘Type-I CdS/ZnS Core/Shell Quantum Dot-Gold Heterostructural Nanocrystals for Enhanced Photocatalytic Hydrogen Generation’, *J. Am. Chem. Soc.*, vol. 145, no. 40, pp. 21886-21896, 2023.

[35] N. Jin, Y. Nagaoka, Z. Liu, R. Li, and O. Chen, ‘Pressure-Modulated Energy Transfer Dynamics in Mn2+-Doped CdS/ZnS Core/Shell Quantum Dots’, *J. Am. Chem. Soc.*, vol. 147, no. 9, pp. 7965-7973, 2025.

[36] S. Schünemann, D. M. Gastel, and D. H. Tüysüz, 'A CsPbBr3/TiO2 Composite for Visible-Light-Driven Photocatalytic Benzyl Alcohol Oxidation', *ChemSusChem*, vol. 11, no. 13, pp. 2057-2061, 2018.

[37] J. Joy, A. Krishnamoorthy, A. Tanna, V. Kamathe, R. Nagar, and S. Srinivasan, 'Recent Developments on the Synthesis of Nanocomposite Materials via Ball Milling Approach for Energy Storage Applications', *Appl. Sci.*, vol. 12, no. 9312, 2022.

[38] F. Xu, K. Meng, B. Cheng, S. Wang, J. Xu, and J. Yu, 'Unique S-scheme heterojunctions in self-assembled TiO2/CsPbBr3 hybrids for CO2 photoreduction', *Nat. Commun.*, vol. 4613, 2020.

[39] H. Z. Z. Wang *et al.*, 'Type-I Heterostructure Based on WS2/PtS2 for High-Performance Photodetectors', *ACS Appl. Mater. Interfaces*, vol. 14, no. 33, 2022.

[40] X. Xue, C. L. M. L. T. H. Y. L. Y. Ge, W. D., and X. Xu, 'Type-I SnSe2/ZnS heterostructure improving photoelectrochemical photodetection and water splitting', *Sci. China Mater.*, vol. 66, 2022.

[41] N. Ma *et al.*, 'Self-surface-oxidation protection of Type-I Te/SnS2 heterostructure based photodetectors for high-stability and fast-speed underwater optical communication application', *Chem. Eng. J.*, vol. 505, p. 159413, 2025.

[42] X. Chen, C. Z. H. W. Y. S. C. C., and X. Zhou, 'Two-Dimensional ZnS/SnS2 Heterojunction as a Direct Z-Scheme Photocatalyst for Overall Water Splitting: A DFT Study', *Materials*, vol. 15, no. 11, p. 3789, 2022.

[43] J. Low, J. Yu, M. Jaroniec, S. Wageh, and A. A. Al-Ghamdi, 'Heterojunction Photocatalysts', *Adv. Mater.*, vol. 29, no. 20, 2017.

[44] G. Liao, C. L. X. Li, and B. Fang, 'Emerging polymeric carbon nitride Z-scheme systems for photocatalysis', *Cell Rep. Phys. Sci.*, 2021.

[45] X. Meng *et al.*, 'Boosting Hydrogen Evolution Performance of a CdS-Based Photocatalyst: In Situ Transition from Type I to Type II Heterojunction during Photocatalysis', *ACS Catal.*, vol. 12, no. 16, 2022.

[46] W. Song *et al.*, 'Unraveling the Transformation from Type-II to Z-Scheme in Perovskite-Based Heterostructures for Enhanced Photocatalytic CO2 Reduction', *J. Am. Chem. Soc.*, vol. 146, no. 5, 2024.

[47] M. Grätzel, 'Photoelectrochemical cells', *Nature*, vol. 414, 2001.

[48] R. D. Harris *et al.*, 'Electronic Processes within Quantum Dot-Molecule Complexes', *Chem. Rev.*, vol. 116, no. 21, 2016.

[49] J. K. Utterback, J. L. Ruzicka, H. R. Keller, L. M. Pellows, and G. Dukovic, 'Electron Transfer from Semiconductor Nanocrystals to Redox Enzymes', *Annu. Rev. Phys. Chem.*, vol. 71, 2020.

[50] A. Asaithambi, N. K. Tofighi, N. K. Tofighi, N. Curreli, N. Curreli, and I. Kriegela, 'Energy transfer and charge transfer between semiconducting nanocrystals and transition metal dichalcogenide monolayers', *Chem. Commun.*, vol. 59, no. 50, 2023.

[51] R. Rossetti and L. E. Brus, 'Picosecond resonance Raman scattering study of methylviologen reduction on the surface of photoexcited colloidal cadmium sulfide crystallites', *J. Phys. Chem.*, vol. 90, no. 4, 1986.

[52] R. Rossetti, S. M. Beck, and L. E. Brus, 'Direct observation of charge-transfer reactions across semiconductor: aqueous solution interfaces using transient Raman spectroscopy', *J. Am. Chem.*, vol. 106, no. 4, 1984.

[53] P. V. Kamat, N. M. Dimitrijevic, and R. W. Fessenden, 'Photoelectrochemistry in particulate systems. 6. Electron-transfer reactions of small cadmium sulfide colloids in acetonitrile', *J. Phys. Chem.*, vol. 91, no. 2, 1987.

[54] S. Logunov, T. Green, S. Marguet, and M. A. El-Sayed, 'Interfacial Carriers Dynamics of CdS Nanoparticles', *J. Phys. Chem. A*, vol. 102, no. 28, 1998.

[55] J. E. Evans, K. W. Springer, and J. Z. Zhang, ‘Femtosecond studies of interparticle electron transfer in a coupled CdS–TiO2 colloidal system’, *J. Chem. Phys.*, vol. 101, 1994.

[56] L. Amirav and A. P. Alivisatos, ‘Photocatalytic Hydrogen Production with Tunable Nanorod Heterostructures’, *J. Phys. Chem. Lett.*, vol. 1, no. 7, 2010.

[57] J. C. S. Ponseca, P. Chábera, J. Uhlig, P. Persson, and V. Sundström, ‘Ultrafast Electron Dynamics in Solar Energy Conversion’, *Chem. Rev.*, vol. 117, no. 16, 2017.

[58] Y. Zhang, G. Wu, F. Liu, C. Ding, Z. Zou, and Q. Shen, ‘Photoexcited carrier dynamics in colloidal quantum dot solar cells: insights into individual quantum dots, quantum dot solid films and devices’, *J.*, vol. 49, no. 1, 2020.

[59] X.-B. Li and C.-H. T. L.-Z. Wu, ‘Semiconducting quantum dots for artificial photosynthesis’, *Nat. Rev. Chem.*, vol. 2, 2018.

[60] Q. Hu, X. Yu, S. Gong, and X. Chen, ‘Nanomaterial catalysts for organic photoredox catalysis-mechanistic perspective’, *Nanoscale*, no. 43, 2021.

[61] Peter. Atkins, *PHYSICAL CHEMISTRY*. Oxford University Press, 2014.

[62] N. Kumar, M. Patel, T. T. Nguyen, S. Kim, and J. Kim, ‘Effect of TiO2 layer thickness of TiO2/NiO transparent photovoltaics’, *Prog. Photovolt.*, vol. 29, no. 8, pp. 943-952, 2021.

[63] K. Wang *et al.*, ‘Photovoltaics and its magnetic-field promotion effect in dye-sensitized solar cells with BiFeO3 + TiO2 composite photoanodes’, *Sol. Energy*, vol. 242, pp. 184–190.

[64] F. M. El-Hossary, A. Ghitas, A. M. A. El-Rahman, A. A. Ebnalwaled, and M. A. Shahat, ‘Characterization and Performance of PAni-TiO2 Photovoltaic Cells Treated by RF Plasma’, *IOP Conf. Ser. Mater. Sci. Eng.*, vol. 956, 2020.

[65] X. Hu *et al.*, ‘Mechanisms underlying the photocatalytic degradation pathway of ciprofloxacin with heterogeneous TiO2’, *Chem. Eng. J.*, vol. 380, p. 122366, 2020.

[66] S. Wu, H. Hu, Y. Lin, J. Zhang, and Y. H. Hu, ‘Visible light photocatalytic degradation of tetracycline over TiO2’, *Chem. Eng. J.*, vol. 382, 2019.

[67] R. Fatima *et al.*, ‘Photocatalytic degradation performance of various types of modified TiO2 against nitrophenols in aqueous systems’, *J. Clean. Prod.*, vol. 231, pp. 899-912, 2019.

[68] A. Meng, L. Zhang, B. Cheng, and J. Yu, ‘Dual Cocatalysts in TiO2 Photocatalysis’, *Adv. Mater.*, vol. 31, no. 30, p. 1807660, 2019.

[69] L. Wang and J. Yu, ‘Chapter 1 Principles of photocatalysis’, *Interface Sci. Technol. Elsevier*, pp. 1–52, 2023.

[70] P. V. Kamat, ‘Quantum Dot Solar Cells. Semiconductor Nanocrystals as Light Harvesters’, *J. Phys. Chem. C*, vol. 112, no. 48, 2008.

[71] I. Robel, V. Subramanian, M. Kuno, and P. V. Kamat, ‘Quantum Dot Solar Cells. Harvesting Light Energy with CdSe Nanocrystals Molecularly Linked to Mesoscopic TiO2 Films’, *J. Am. Chem. Soc.*, vol. 128, no. 7, 2006.

[72] P. A. Sant and P. V. Kamat, ‘Interparticle electron transfer between size-quantized CdS and TiO2 semiconductor nanoclusters’, *Phys. Chem. Chem. Phys.*, no. 2, 2002.

[73] I. Robel, M. Kuno, and P. V. Kamat, ‘Size-Dependent Electron Injection from Excited CdSe Quantum Dots into TiO2 Nanoparticles’, *J. Am. Chem. Soc.*, vol. 129, no. 14, 2007.

[74] J. Hua, M. Wang, M. Wang, H. L., and Y. Y. and, ‘Strongly coupled CdX (Xdouble bondS, Se and Te) quantum dots/TiO2 nanocomposites for photocatalytic degradation of benzene under visible light irradiation’, *Optik*, vol. 171, pp. 95-106, 2018.

[75] S. Subramanian, S. Ganapathy, S. Subramanian, and G. Venkataramani, ‘Investigations on Multiexciton Generation and Hot Electron Transfer Process in CdTe QD-Decorated TiO2 Nanostructures for Effective Photocatalytic Activity’, *Ind. Eng. Chem. Res.*, vol. 62, no. 46, 2023.

[76] Y. Li *et al.*, 'Sized dependence and microstructural defects on highly photocatalytic activity based on multisized CdTe quantum dots sensitized TiO2', *Surf. INTERFACE Anal.*, vol. 51, no. 10, 2019.

[77] E. Benavente *et al.*, 'Application of CdTe quantum dots sensitized titanate nanotubes in photocatalytic degradation of organic pollutants under visible light irradiation', *J. Environ. Chem. Eng.*, vol. 11, no. 3, p. 110025, Jun. 2023, doi: 10.1016/j.jece.2023.110025.

[78] X. Ma, Q. Xiang, Y. Liao, T. Wen, and H. Zhang, 'Visible-light-driven CdSe quantum dots/graphene/TiO2 nanosheets composite with excellent photocatalytic activity for E. coli disinfection and organic pollutant degradation', *Appl. Surf. Sci.*, vol. 457, no. 1, pp. 846-855, 2018.

[79] M. An *et al.*, 'CdS QDs modified three-dimensional ordered hollow spherical ZnTiO3-ZnO-TiO2 composite with improved photocatalytic performance', *J. Alloys Compd.*, vol. 895, no. 2, p. 162638, 2022.

[80] D. Lv *et al.*, 'Enhanced photocatalytic performance of hollow spherical CdS QDs@ZrO2–TiO2 composites with double Z-scheme heterostructures', *Int. J. Hydrog. Energy*, vol. 48, no. 71, pp. 27582-27598, 2023.

[81] C. Farrugia *et al.*, 'Suitability of Different Titanium Dioxide Nanotube Morphologies for Photocatalytic Water Treatment', *Nanomaterials*, vol. 11, no. 3, p. 708, Mar. 2021, doi: 10.3390/nano11030708.

[82] J. Lee, S. Moon, S. S. Patil, and K. Lee, 'Visible photoresponse of TiO2 nanotubes in comparison to that of nanoparticles and anodic thin film', *Catal. Today*, vol. 403, pp. 39–46, Nov. 2022, doi: 10.1016/j.cattod.2022.01.008.

[83] S. A. M and R. S. Hyam, 'Au nanoparticles decorated titanium dioxide nanotube arrays with enhanced photocatalytic dye degradation under ultraviolet and sunlight irradiation', *Results Surf. Interfaces*, vol. 12, p. 100140, Aug. 2023, doi: 10.1016/j.rsurfi.2023.100140.

[84] D. Nematov, A. Ashurov, and M. Umarzoda, 'TiO_2 for Photocatalysis and Energy Conversion: A Detailed Overview of the Synthesis, Applications, Challenges, Advances and Prospects for Sustainable Development', Aug. 26, 2024, *Physical Sciences*. doi: 10.20944/preprints202408.1733.v1.

[85] I. Concina, Z. H. Ibupoto, and A. Vomiero, 'Semiconducting Metal Oxide Nanostructures for Water Splitting and Photovoltaics', *Adv. Energy Mater.*, vol. 7, no. 23, p. 1700706, Dec. 2017, doi: 10.1002/aenm.201700706.

[86] P. Petrisková *et al.*, 'Preparation and photocatalytic activity of TiO2 nanotube arrays prepared on transparent spinel substrate', *Ceram. Int.*, vol. 47, no. 9, pp. 12970–12980, May 2021, doi: 10.1016/j.ceramint.2021.01.160.

[87] S. Abela *et al.*, 'Photocatalytic Activity of Titanium Dioxide Nanotubes Following Long-Term Aging', *Nanomaterials*, vol. 11, no. 11, p. 2823, Oct. 2021, doi: 10.3390/nano11112823.

[88] S. Durdu, M. Sancak, E. Yalcin, M. Usta, E. Akagunduz, and A. Altinkok, 'Surface characterization of TiO2 nanotube arrays produced on Ti6Al4V alloy by anodic oxidation', *Surf. Coat. Technol.*, vol. 428, p. 127903, Dec. 2021, doi: 10.1016/j.surfcoat.2021.127903.

[89] J. M. Herrmann, J. Disdier, and P. Pichat, 'Photoassisted platinum deposition on TiO2 powder using various platinum complexes', *J. Phys. Chem.*, vol. 90, no. 22, pp. 6028–6034, Oct. 1986, doi: 10.1021/j100280a114.

[90] W. Raza, A. B. Tesler, A. Mazare, and P. Schmuki, 'Solar Light-Induced Photoelectrochemical H_2 Generation Over Hierarchical TiO_2 Nanotube Arrays Decorated with CdS Nanoparticles', *J. Electrochem. Soc.*, vol. 171, no. 6, p. 066506, Jun. 2024, doi: 10.1149/1945-7111/ad52f2.

[91] Y. Liu, H. Wu, M. Li, J.-J. Yin, and Z. Nie, 'pH dependent catalytic activities of platinum nanoparticles with respect to the decomposition of hydrogen peroxide and scavenging of superoxide and singlet oxygen', *Nanoscale*, vol. 6, no. 20, pp. 11904–11910, Aug. 2014, doi: 10.1039/C4NR03848G.

[92] T. Luttrell, S. Halpegamage, J. Tao, A. Kramer, E. Sutter, and M. Batzill, ‘Why is anatase a better photocatalyst than rutile? - Model studies on epitaxial TiO2 films’, *Sci. Rep.*, vol. 4, no. 1, p. 4043, Feb. 2014, doi: 10.1038/srep04043.

[93] J. Zhang, P. Zhou, J. Liu, and J. Yu, ‘New understanding of the difference of photocatalytic activity among anatase, rutile and brookite TiO_2’, *Phys. Chem. Chem. Phys.*, vol. 16, no. 38, pp. 20382–20386, 2014, doi: 10.1039/C4CP02201G.

[94] G. Žerjav, K. Žižek, J. Zavašnik, and A. Pintar, ‘Brookite vs. rutile vs. anatase: What`s behind their various photocatalytic activities?’, *J. Environ. Chem. Eng.*, vol. 10, no. 3, p. 107722, Jun. 2022, doi: 10.1016/j.jece.2022.107722.

[95] J. M. Macak *et al.*, ‘TiO2 nanotubes: Self-organized electrochemical formation, properties and applications’, *Curr. Opin. Solid State Mater. Sci.*, vol. 11, no. 1–2, pp. 3–18, Feb. 2007, doi: 10.1016/j.cossms.2007.08.004.

[96] I. Paramasivam, H. Jha, N. Liu, and P. Schmuki, ‘A Review of Photocatalysis using Self-organized TiO_2 Nanotubes and Other Ordered Oxide Nanostructures’, *Small*, vol. 8, no. 20, pp. 3073–3103, Oct. 2012, doi: 10.1002/smll.201200564.

[97] X. Chen, S. Qin, N. Denisov, S.-Z. Kure-Chu, and P. Schmuki, ‘Pt-single atom decorated TiO2: Tuning anodic TiO2 nanotube structure and geometry toward a high-performance photocatalytic H2 production’, *Electrochimica Acta*, vol. 446, p. 142081, Apr. 2023, doi: 10.1016/j.electacta.2023.142081.

[98] J. Jeon, D. H. Kweon, B. J. Jang, M. J. Ju, and J. Baek, ‘Enhancing the Photocatalytic Activity of TiO_2 Catalysts’, *Adv. Sustain. Syst.*, vol. 4, no. 12, p. 2000197, Dec. 2020, doi: 10.1002/adsu.202000197.

[99] A. G. Muñoz, ‘Semiconducting properties of self-organized TiO2 nanotubes’, *Electrochimica Acta*, vol. 52, no. 12, pp. 4167–4176, Mar. 2007, doi: 10.1016/j.electacta.2006.11.035.

[100] Z. Liu *et al.*, ‘Highly Ordered TiO_2 Nanotube Arrays with Controllable Length for Photoelectrocatalytic Degradation of Phenol’, *J. Phys. Chem. C*, vol. 112, no. 1, pp. 253–259, Jan. 2008, doi: 10.1021/jp0772732.

[101] L. Chouhan, S. Ghimire, C. Subrahmanyam, T. Miyasaka, and V. Biju, ‘Synthesis, optoelectronic properties and applications of halide perovskites’, *Chem. Soc. Rev.*, vol. 49, no. 10, pp. 2869-2885, 2020.

[102] S. Ghimire *et al.*, ‘Highly Luminescent and Stable Halide Perovskite Nanocrystals by Interfacial Defect Passivation and Amphiphilic Ligand Capping’, *ACS Appl. Mater. Interfaces*, vol. 15, no. 34, 2023.

[103] S. Sun, D. Yuan, Y. Xu, A. Wang, and Z. Deng, ‘Ligand-Mediated Synthesis of Shape-Controlled Cesium Lead Halide Perovskite Nanocrystals via Reprecipitation Process at Room Temperature’, *ACS Nano*, vol. 10, no. 3, pp. 3648-3657, 2016.

[104] N. Fiuza-Maneiro, K. Sun, I. López-Fernández, S. Gómez-Graña, P. Müller-Buschbaum, and L. Polavarapu, ‘Ligand Chemistry of Inorganic Lead Halide Perovskite Nanocrystals’, *ACS Energy Lett.*, vol. 8, no. 2, pp. 1152–1191, Feb. 2023, doi: 10.1021/acsenergylett.2c02363.

[105] L. Protesescu† *et al.*, ‘Nanocrystals of Cesium Lead Halide Perovskites (CsPbX3, X = Cl, Br, and I): Novel Optoelectronic Materials Showing Bright Emission with Wide Color Gamut’, *Nano Lett.*, vol. 15, no. 6, 2015.

[106] Y. Li, X. Wang, W. Xue, W. Wang, W. Zhu, and L. Zhao, ‘Highly luminescent and stable CsPbBr3 perovskite quantum dots modified by phosphine ligands’, *Nano Res.*, vol. 12, no. 4, pp. 785–789, Apr. 2019, doi: 10.1007/s12274-019-2289-8.

[107] G. Almeida *et al.*, ‘The Phosphine Oxide Route toward Lead Halide Perovskite Nanocrystals’, *J. Am. Chem. Soc.*, vol. 140, no. 44, pp. 14878–14886, Nov. 2018, doi: 10.1021/jacs.8b08978.

[108] D. Yang *et al.*, ‘CsPbBr3 Quantum Dots 2.0: Benzenesulfonic Acid Equivalent Ligand Awakens Complete Purification’, *Adv. Mater.*, vol. 31, no. 30, p. 1900767, 2019, doi: 10.1002/adma.201900767.

[109] Y. Shynkarenko *et al.*, 'Direct Synthesis of Quaternary Alkylammonium-Capped Perovskite Nanocrystals for Efficient Blue and Green Light-Emitting Diodes', *ACS Energy Lett.*, vol. 4, no. 11, pp. 2703–2711, Nov. 2019, doi: 10.1021/acsenergylett.9b01915.

[110] F. Krieg *et al.*, 'Colloidal CsPbX3 (X = Cl, Br, I) Nanocrystals 2.0: Zwitterionic Capping Ligands for Improved Durability and Stability', *ACS Energy Lett.*, vol. 3, no. 3, pp. 641–646, Mar. 2018, doi: 10.1021/acsenergylett.8b00035.

[111] J. Pan *et al.*, 'Bidentate Ligand-Passivated CsPbI3 Perovskite Nanocrystals for Stable Near-Unity Photoluminescence Quantum Yield and Efficient Red Light-Emitting Diodes', *J. Am. Chem. Soc.*, vol. 140, no. 2, pp. 562–565, Jan. 2018, doi: 10.1021/jacs.7b10647.

[112] E. T. Vickers *et al.*, 'Improving Charge Carrier Delocalization in Perovskite Quantum Dots by Surface Passivation with Conductive Aromatic Ligands', *ACS Energy Lett.*, vol. 3, no. 12, pp. 2931–2939, Dec. 2018, doi: 10.1021/acsenergylett.8b01754.

[113] S. Akhil, V. G. V. Dutt, R. Singh, and N. Mishra, 'Surface-State-Mediated Interfacial Hole Transfer Dynamics between CsPbBr3 Perovskite Nanocrystals and Phenothiazine Redox Couple', *J. Phys. Chem. C*, vol. 125, no. 40, pp. 22133–22141, Oct. 2021, doi: 10.1021/acs.jpcc.1c07129.

[114] S. Kumar, J. Jagielski, T. Marcato, S. F. Solari, and C.-J. Shih, 'Understanding the Ligand Effects on Photophysical, Optical, and Electroluminescent Characteristics of Hybrid Lead Halide Perovskite Nanocrystal Solids', *J. Phys. Chem. Lett.*, vol. 10, no. 24, pp. 7560–7567, Dec. 2019, doi: 10.1021/acs.jpclett.9b02950.

[115] S. Biswas *et al.*, 'Exploring the Role of Short Chain Acids as Surface Ligands in Photoinduced Charge Transfer Dynamics from CsPbBr3 Perovskite Nanocrystals', *J. Phys. Chem. Lett.*, vol. 14, no. 7, pp. 1910–1917, Feb. 2023, doi: 10.1021/acs.jpclett.2c03772.

[116] M. Kazes, T. Udayabhaskararao, S. Dey, and D. Oron, 'Effect of Surface Ligands in Perovskite Nanocrystals: Extending in and Reaching out', *Acc. Chem. Res.*, vol. 54, no. 6, pp. 1409–1418, Mar. 2021, doi: 10.1021/acs.accounts.0c00712.

[117] X. Liu *et al.*, 'Ligand-modulated electron transfer rates from CsPbBr3 nanocrystals to titanium dioxide', *Nanophotonics*, vol. 10, no. 8, pp. 1967–1975, Jun. 2020, doi: 10.1515/nanoph-2020-0631.

[118] J. T. DuBose and P. V. Kamat, 'Surface Chemistry Matters. How Ligands Influence Excited State Interactions between CsPbBr3 and Methyl Viologen', *J. Phys. Chem. C*, vol. 124, no. 24, pp. 12990–12998, Jun. 2020, doi: 10.1021/acs.jpcc.0c03004.

[119] E. T. Vickers *et al.*, 'Enhancing Charge Carrier Delocalization in Perovskite Quantum Dot Solids with Energetically Aligned Conjugated Capping Ligands', *ACS Energy Lett.*, vol. 5, no. 3, pp. 817–825, Mar. 2020, doi: 10.1021/acsenergylett.0c00093.

[120] C. Wang, A. Malinoski, J. Yuan, C. Brea, and G. Hu, 'A Surface Engineering Approach for Promoting Dexter Energy Transfer from Lead Halide Perovskite Nanocrystals', *J. Phys. Chem. C*, vol. 127, no. 2, pp. 1135–1144, Jan. 2023, doi: 10.1021/acs.jpcc.2c07664.

[121] J. Pan *et al.*, 'Highly Efficient Perovskite-Quantum-Dot Light-Emitting Diodes by Surface Engineering', *Adv. Mater.*, vol. 28, no. 39, pp. 8718–8725, 2016, doi: 10.1002/adma.201600784.

[122] J. Duan, Y. Wang, X. Yang, and Q. Tang, 'Alkyl-Chain-Regulated Charge Transfer in Fluorescent Inorganic CsPbBr3 Perovskite Solar Cells', *Angew. Chem. Int. Ed.*, vol. 59, no. 11, pp. 4391–4395, 2020, doi: 10.1002/anie.202000199.

[123] Q. Shang, B. D. Piercy, M. D. Losego, and T. Lian, 'Effect of Surface Ligand on Charge Separation and Recombination at CsPbI3 Perovskite Quantum Dot/TiO2 Interfaces', *J. Phys. Chem. C*, vol. 123, no. 35, pp. 21415–21421, Sep. 2019, doi: 10.1021/acs.jpcc.9b06725.

[124] Y. Zhang *et al.*, 'A "Tips and Tricks" Practical Guide to the Synthesis of Metal Halide Perovskite Nanocrystals', *Chem. Mater.*, vol. 32, no. 13, pp. 5410–5423, Jul. 2020, doi: 10.1021/acs.chemmater.0c01735.

[125] J. Ye *et al.*, 'Elucidating the Role of Antisolvents on the Surface Chemistry and Optoelectronic Properties of CsPbBrxI3-x Perovskite Nanocrystals', *J. Am. Chem. Soc.*, vol. 144, no. 27, pp. 12102–12115, Jul. 2022, doi: 10.1021/jacs.2c02631.

[126] K. Ma *et al.*, 'Multifunctional Conjugated Ligand Engineering for Stable and Efficient Perovskite Solar Cells', *Adv. Mater.*, vol. 33, no. 32, p. 2100791, 2021, doi: 10.1002/adma.202100791.

[127] S. Sun, D. Yuan, Y. Xu, A. Wang, and Z. Deng, 'Ligand-Mediated Synthesis of Shape-Controlled Cesium Lead Halide Perovskite Nanocrystals *via* Reprecipitation Process at Room Temperature', *ACS Nano*, vol. 10, no. 3, pp. 3648–3657, Mar. 2016, doi: 10.1021/acsnano.5b08193.

[128] A. Pan *et al.*, 'Insight into the Ligand-Mediated Synthesis of Colloidal CsPbBr3 Perovskite Nanocrystals: The Role of Organic Acid, Base, and Cesium Precursors', *ACS Nano*, vol. 10, no. 8, pp. 7943–7954, Aug. 2016, doi: 10.1021/acsnano.6b03863.

[129] Y. Yuan, Z. Liu, Z. Liu, L. Peng, Y. Li, and A. Tang, 'Photoluminescence and self-assembly of cesium lead halide perovskite nanocrystals: Effects of chain length of organic amines and reaction temperature', *Appl. Surf. Sci.*, vol. 405, pp. 280–288, May 2017, doi: 10.1016/j.apsusc.2017.02.024.

[130] S. Yang *et al.*, 'Ultrathin Two-Dimensional Organic–Inorganic Hybrid Perovskite Nanosheets with Bright, Tunable Photoluminescence and High Stability', *Angew. Chem. Int. Ed.*, vol. 56, no. 15, pp. 4252–4255, 2017, doi: https://doi.org/10.1002/anie.201701134.

[131] S. Ghimire and C. Klinke, 'Two-dimensional halide perovskites: synthesis, optoelectronic properties, stability, and applications', *Nanoscale*, vol. 13, no. 29, pp. 12394–12422, 2021, doi: 10.1039/D1NR02769G.

[132] S. Ghimire, K. Oldenburg, S. Bartling, R. Lesyuk, and C. Klinke, 'Structural Reconstruction in Lead-Free Two-Dimensional Tin Iodide Perovskites Leading to High Quantum Yield Emission', *ACS Energy Lett.*, vol. 7, no. 3, pp. 975–983, Mar. 2022, doi: 10.1021/acsenergylett.1c02777.

[133] F. Haydous, J. M. Gardner, and U. B. Cappel, 'The impact of ligands on the synthesis and application of metal halide perovskite nanocrystals', *J. Mater. Chem. A*, vol. 9, no. 41, pp. 23419–23443, 2021, doi: 10.1039/D1TA05242J.

[134] J. De Roo *et al.*, 'Highly Dynamic Ligand Binding and Light Absorption Coefficient of Cesium Lead Bromide Perovskite Nanocrystals', *ACS Nano*, vol. 10, no. 2, pp. 2071–2081, Feb. 2016, doi: 10.1021/acsnano.5b06295.

[135] V. K. Ravi *et al.*, 'Origin of the Substitution Mechanism for the Binding of Organic Ligands on the Surface of CsPbBr3 Perovskite Nanocubes', *J. Phys. Chem. Lett.*, vol. 8, no. 20, pp. 4988–4994, Oct. 2017, doi: 10.1021/acs.jpclett.7b02192.

[136] S. R. Smock, T. J. Williams, and R. L. Brutchey, 'Quantifying the Thermodynamics of Ligand Binding to CsPbBr3 Quantum Dots', *Angew. Chem. Int. Ed.*, vol. 57, no. 36, pp. 11711–11715, 2018, doi: 10.1002/anie.201806916.

[137] S. Dey, H. Cohen, I. Pinkas, H. Lin, M. Kazes, and D. Oron, 'Band alignment and charge transfer in CsPbBr3–CdSe nanoplatelet hybrids coupled by molecular linkers', *J. Chem. Phys.*, vol. 151, no. 17, p. 174704, Nov. 2019, doi: 10.1063/1.5124552.

[138] R. A. Scheidt, E. Kerns, and P. V. Kamat, 'Interfacial Charge Transfer between Excited $CsPbBr_3$ Nanocrystals and TiO_2 : Charge Injection versus Photodegradation', *J. Phys. Chem. Lett.*, vol. 9, no. 20, pp. 5962–5969, Oct. 2018, doi: 10.1021/acs.jpclett.8b02690.

[139] R. Salazar *et al.*, 'Use of Anodic TiO_2 Nanotube Layers as Mesoporous Scaffolds for Fabricating CH_3 NH_3 PbI_3 Perovskite-Based Solid-State Solar Cells', *ChemElectroChem*, vol. 2, no. 6, pp. 824–828, Jun. 2015, doi: 10.1002/celc.201500031.

[140] H.-Y. Yang, W.-Y. Rho, S. K. Lee, S. H. Kim, and Y.-B. Hahn, 'TiO2 Nanoparticles/Nanotubes for Efficient Light Harvesting in Perovskite Solar Cells', *Nanomaterials*, vol. 9, no. 3, p. 326, Mar. 2019, doi: 10.3390/nano9030326.

[141] C. Zhen, T. Wu, R. Chen, L. Wang, G. Liu, and H.-M. Cheng, 'Strategies for Modifying TiO_2 Based Electron Transport Layers to Boost Perovskite Solar Cells', *ACS Sustain. Chem. Eng.*, vol. 7, no. 5, pp. 4586–4618, Mar. 2019, doi: 10.1021/acssuschemeng.8b06580.

[142] A. Kojima, K. Teshima, Y. Shirai, and T. Miyasaka, 'Organometal Halide Perovskites as Visible-Light Sensitizers for Photovoltaic Cells', *J. Am. Chem. Soc.*, vol. 131, no. 17, pp. 6050–6051, May 2009, doi: 10.1021/ja809598r.

[143] H. Huang, B. Pradhan, J. Hofkens, M. B. J. Roeffaers, and J. A. Steele, 'Solar-Driven Metal Halide Perovskite Photocatalysis: Design, Stability, and Performance', *ACS Energy Lett.*, vol. 5, no. 4, pp. 1107–1123, Apr. 2020, doi: 10.1021/acsenergylett.0c00058.

[144] K. Vighnesh, S. Wang, H. Liu, and A. L. Rogach, 'Hot-Injection Synthesis Protocol for Green-Emitting Cesium Lead Bromide Perovskite Nanocrystals', *ACS Nano*, vol. 16, no. 12, pp. 19618–19625, Dec. 2022, doi: 10.1021/acsnano.2c11689.

[145] F. Palazon *et al.*, 'Changing the Dimensionality of Cesium Lead Bromide Nanocrystals by Reversible Postsynthesis Transformations with Amines', *Chem. Mater.*, vol. 29, no. 10, pp. 4167–4171, May 2017, doi: 10.1021/acs.chemmater.7b00895.

[146] R. M. Silverstein, 'Spectrometric identification of organic compounds', vol. 39, no. 11, p. 546, 1962.

[147] M. C. Brennan, M. Kuno, and S. Rouvimov, 'Crystal Structure of Individual $CsPbBr_3$ Perovskite Nanocubes', *Inorg. Chem.*, vol. 58, no. 2, pp. 1555–1560, Jan. 2019, doi: 10.1021/acs.inorgchem.8b03078.

[148] C. C. Stoumpos *et al.*, 'Crystal Growth of the Perovskite Semiconductor $CsPbBr_3$: A New Material for High-Energy Radiation Detection', *Cryst. Growth Des.*, vol. 13, no. 7, pp. 2722–2727, Jul. 2013, doi: 10.1021/cg400645t.

[149] A. Swarnkar, R. Chulliyil, V. K. Ravi, M. Irfanullah, A. Chowdhury, and A. Nag, 'Colloidal $CsPbBr_3$ Perovskite Nanocrystals: Luminescence beyond Traditional Quantum Dots', *Angew. Chem.*, vol. 127, no. 51, pp. 15644–15648, Dec. 2015, doi: 10.1002/ange.201508276.

[150] J. K George, S. Ramu, V. V. Halali, and R. G. Balakrishna, 'Inner Filter Effect as a Boon in Perovskite Sensing Systems to Achieve Higher Sensitivity Levels', *ACS Appl. Mater. Interfaces*, vol. 13, no. 48, pp. 57264–57273, Dec. 2021, doi: 10.1021/acsami.1c17061.

[151] J. R. Lakowicz, *Principles of Fluorescence Spectroscopy*. Springer US, 2006.

[152] I. Vinçon, A. Barfüßer, J. Feldmann, and Q. A. Akkerman, 'Quantum Dot Metal Salt Interactions Unraveled by the Sphere of Action Model', *J. Am. Chem. Soc.*, vol. 145, no. 26, pp. 14395–14403, Jul. 2023, doi: 10.1021/jacs.3c03582.

[153] I. Vinçon, A. Barfüßer, J. Feldmann, and Q. A. Akkerman, 'Quantum Dot Metal Salt Interactions Unraveled by the Sphere of Action Model', *J. Am. Chem. Soc.*, vol. 145, no. 26, pp. 14395–14403, Jul. 2023, doi: 10.1021/jacs.3c03582.

[154] B. M. Sachith *et al.*, 'Long-Range Interfacial Charge Carrier Trapping in Halide Perovskite-C_{60} and Halide Perovskite-TiO_2 Donor–Acceptor Films', *J. Phys. Chem. Lett.*, vol. 12, no. 35, pp. 8644–8651, Sep. 2021, doi: 10.1021/acs.jpclett.1c01909.

[155] K. Zheng, K. Žídek, M. Abdellah, M. E. Messing, M. J. Al-Marri, and T. Pullerits, 'Trap States and Their Dynamics in Organometal Halide Perovskite Nanoparticles and Bulk Crystals', *J. Phys. Chem. C*, vol. 120, no. 5, pp. 3077–3084, Feb. 2016, doi: 10.1021/acs.jpcc.6b00612.

[156] K. P. Chiu, 'The influence of a trap state on the photoluminescence decay times under single pulse excitation', *Opt. Quantum Electron.*, vol. 55, no. 2, p. 163, Feb. 2023, doi: 10.1007/s11082-022-04433-w.

[157] C.-W. Wang, X. Liu, T. Qiao, M. Khurana, A. V. Akimov, and D. H. Son, 'Photoemission of the Upconverted Hot Electrons in Mn-Doped $CsPbBr_3$ Nanocrystals', *Nano Lett.*, vol. 22, no. 16, pp. 6753–6759, Aug. 2022, doi: 10.1021/acs.nanolett.2c02342.

[158] C. Reichardt and T. Welton, *Solvents and Solvent Effects in Organic Chemistry*, 1st ed. Wiley, 2010. doi: 10.1002/9783527632220.

[159] D. Parobek, Y. Dong, T. Qiao, and D. H. Son, 'Direct Hot-Injection Synthesis of Mn-Doped $CsPbBr_3$ Nanocrystals', *Chem. Mater.*, vol. 30, no. 9, pp. 2939–2944, May 2018, doi: 10.1021/acs.chemmater.8b00310.

[160] L. Wu *et al.*, 'Interfacial Manganese-Doping in $CsPbBr_3$ Nanoplatelets by Employing a Molecular Shuttle', *Angew. Chem. Int. Ed.*, vol. 61, no. 15, p. e202115852, Apr. 2022, doi: 10.1002/anie.202115852.

[161] Y. Bekenstein, B. A. Koscher, S. W. Eaton, P. Yang, and A. P. Alivisatos, 'Highly Luminescent Colloidal Nanoplates of Perovskite Cesium Lead Halide and Their Oriented Assemblies', *J. Am. Chem. Soc.*, vol. 137, no. 51, pp. 16008–16011, Dec. 2015, doi: 10.1021/jacs.5b11199.

[162] D. Parobek, Y. Dong, T. Qiao, and D. H. Son, 'Direct Hot-Injection Synthesis of Mn-Doped $CsPbBr_3$ Nanocrystals', *Chem. Mater.*, vol. 30, no. 9, pp. 2939–2944, May 2018, doi: 10.1021/acs.chemmater.8b00310.

[163] L. Dai *et al.*, 'Role of Magnetic Coupling in Photoluminescence Kinetics of Mn^{2+} -Doped ZnS Nanoplatelets', *ACS Appl. Mater. Interfaces*, vol. 14, no. 16, pp. 18806–18815, Apr. 2022, doi: 10.1021/acsami.1c25191.

[164] L. Dai, C. Strelow, R. Lesyuk, C. Klinke, T. Kipp, and A. Mews, 'Mn^{2+} -Doped ZnSe/ZnS Core/Shell Nanoplatelets as Low-Toxic UV-to-Vis Light-Converters with Enhanced Optical Properties', *ACS Appl. Nano Mater.*, vol. 6, no. 13, pp. 11124–11134, Jul. 2023, doi: 10.1021/acsanm.3c00679.

[165] L. Du *et al.*, 'Photogenerated carrier dynamics of Mn2+ doped CsPbBr3 assembled with TiO2 systems: Effect of Mn doping content', *J. Chem. Phys.*, vol. 160, no. 16, p. 164713, Apr. 2024, doi: 10.1063/5.0197068.

[166] M. A. Haase *et al.*, 'II–VI semiconductor color converters for efficient green, yellow, and red light emitting diodes', *Appl. Phys. Lett.*, vol. 96, no. 23, pp. 231116-231116, 2010.

[167] A. Kuddus, S. K. Mostaque, S. Mouri, and J. Hossain, 'Emerging II-VI wide bandgap semiconductor device technologies', *Phys. Scr.*, vol. 99, 2024.

[168] B. T. Diroll, B. Guzelturk, H. Po, C. Dabard, N. Fu, and L. Makke, '2D II–VI Semiconductor Nanoplatelets: From Material Synthesis to Optoelectronic Integration', *Chem. Rev.*, vol. 123, no. 7, pp. 3543-3624, 2023.

[169] Y. Al-Douri, M. M. Khan, and J. R. Jennings, 'Synthesis and optical properties of II–VI semiconductor quantum dots: a review', *J. Mater. Sci. Mater. Electron.*, vol. 34, 2023.

[170] M. T. Hill and M. C. Gather, 'Advances in small lasers', *Nat. Photonics*, vol. 8, pp. 908-918, 2014.

[171] G. Korotcenkov, *Handbook of II-VI Semiconductor-Based Sensors and Radiation Detectors*. Springer Nature Link, 2023.

[172] M. Yamaguch, F. Dimroth, J. F. Geisz, and N. J. Ekins-Daukes, 'Multi-junction solar cells paving the way for super high-efficiency', *J. Appl. Phys.*, vol. 129, no. 24, 2021.

[173] M. Peng, X. S., and Z. Wen, 'Recent Progress of Flexible Photodetectors Based on Low-Dimensional II–VI Semiconductors and Their Application in Wearable Electronics', *Adv. Funct. Mater.*, vol. 33, no. 11, 2022.

[174] T. Mazur, V. Prokopiv, M. Mazur, and U. Pysklynets, 'Solar cells based on CdTe thin films', *Phys. Chem. Solid State*, vol. 22, no. 4, 2021.

[175] S. Hussain, X. Yang, J. Yang, and Q. Li, 'Theoretical insights into the mechanism of photocatalytic reduction of CO2 and water splitting over II-VI zinc chalcogenide semiconductor', *Mater. Today Sustain.*, vol. 25, 2024.

[176] V. Lahariya, P. P. Pandey, and M. Ramrakhiani, '11 - II–VI semiconductor metal chalcogenide nanomaterials and polymer composites: fundamentals, properties, and applications', *Met.-Chalcogenide Nanocomposites*, pp. 187-220, 2024.

[177] A. Rahman and M. M. Khan, 'Chalcogenides as photocatalysts', *New J. Chem.*, vol. 45, pp. 19622-19635, 2021.

[178] W. Xia *et al.*, 'Highly Efficient Photocatalytic Conversion of CO_2 to CO Catalyzed by Surface-Ligand-Removed and Cd-Rich CdSe Quantum Dots', *ChemSusChem*, vol. 12, no. 20, pp. 4617–4622, Oct. 2019, doi: 10.1002/cssc.201901633.

[179] X. Liu *et al.*, 'Hydrothermal Synthesis of CdSe Quantum Dots and Their Photocatalytic Activity on Degradation of Cefalexin', *Ind. Eng. Chem. Res.*, vol. 52, no. 43, pp. 15015–15023, Oct. 2013, doi: 10.1021/ie4028395.

[180] X. Fan, S. Yu, B. Hou, and J. M. Kim, 'Quantum Dots Based Photocatalytic Hydrogen Evolution', *Isr. J. Chem.*, vol. 59, no. 8, pp. 762–773, Aug. 2019, doi: 10.1002/ijch.201900029.

[181] J. Hua, M. Wang, Y. Jiao, H. Li, and Y. Yang, 'Strongly coupled CdX (X S, Se and Te) quantum dots/TiO2 nanocomposites for photocatalytic degradation of benzene under visible light irradiation', *Optik*, vol. 171, pp. 95–106, Oct. 2018, doi: 10.1016/j.ijleo.2018.06.049.

[182] X. Ma, Q. Xiang, Y. Liao, T. Wen, and H. Zhang, 'Visible-light-driven CdSe quantum dots/graphene/TiO2 nanosheets composite with excellent photocatalytic activity for E. coli disinfection and organic pollutant degradation', *Appl. Surf. Sci.*, vol. 457, pp. 846–855, Nov. 2018, doi: 10.1016/j.apsusc.2018.07.003.

[183] E. Benavente *et al.*, 'Application of CdTe quantum dots sensitized titanate nanotubes in photocatalytic degradation of organic pollutants under visible light irradiation', *J. Environ. Chem. Eng.*, vol. 11, no. 3, p. 110025, Jun. 2023, doi: 10.1016/j.jece.2023.110025.

[184] Y. Li *et al.*, 'Sized dependence and microstructural defects on highly photocatalytic activity based on multisized CdTe quantum dots sensitized TiO_2', *Surf. Interface Anal.*, vol. 51, no. 10, pp. 968–981, Oct. 2019, doi: 10.1002/sia.6679.

[185] A. Caglar, H. Kivrak, and N. Aktas, 'The effect of titanium dioxide-supported CdSe photocatalysts enhanced for photocatalytic glucose electrooxidation under UV illumination', *Int. J. Hydrog. Energy*, vol. 47, no. 49, pp. 21130-21145, 2022.

[186] C. Wang, R. L. Thompson, J. Baltrus, and C. Matranga, 'Visible Light Photoreduction of CO2 Using CdSe/Pt/TiO2 Heterostructured Catalysts', *J. Phys. Chem. Lett.*, vol. 1, no. 1, 2009.

[187] S. Manchwari, J. Khatter, and R. Chauhan, 'Enhanced photocatalytic efficiency of TiO2/CdS nanocomposites by manipulating CdS suspension on TiO2 nanoparticles', *Inorg. Chem. Commun.*, vol. 146, p. 110082, 2022.

[188] L. Yang *et al.*, 'Fabrication of CdSe Nanoparticles Sensitized Long TiO2 Nanotube Arrays for Photocatalytic Degradation of Anthracene-9-carbonxylic Acid under Green Monochromatic Light', *J. Phys. Chem. C*, vol. 114, no. 11, 2010.

[189] M. Zhang *et al.*, 'Capability of coupled CdSe/TiO2 heterogeneous structure for photocatalytic degradation and photoconductivity', *Nanoscale Res. Lett.*, vol. 9, no. 1, 2014.

[190] C. W. Lai, K. S. Lau, and P. M. Chou, 'CdSe/TiO2 nanotubes for enhanced photoelectrochemical activity under solar illumination: Influence of soaking time in CdSe bath solution', *Chem. Phys. Lett.*, vol. 714, pp. 6-10, 2019.

[191] F.-X. Xiao, J. Miao, H.-Y. Wang, H. Yang, J. Chen, and B. Liu, 'Electrochemical construction of hierarchically ordered CdSe-sensitized TiO2 nanotube arrays: towards versatile photoelectrochemical water splitting and photoredox applications', *Nanoscale*, vol. 6, no. 12, pp. 6727-6737, 2014.

[192] J. C. Kim *et al.*, 'Enhanced photocatalytic activity in composites of TiO2nanotubes and CdS nanoparticles', *Chem. Commun.*, no. 48, pp. 5024-5026, 2006.

[193] P. F. G. M. Costa, L. G. Merízio, N. Wolff, H. Terraschke, and Camargo, 'Real-time monitoring of CdTe quantum dots growth in aqueous solution', *Sci. Rep.*, vol. 14, 2024.

[194] J. Yang and X. Zhong, 'CdTe based quantum dot sensitized solar cells with efficiency exceeding 7% fabricated from quantum dots prepared in aqueous media', *J. Mater. Chem. A*, vol. 4, pp. 16553-16561, 2016.

[195] D. Li, S. Wang, J. Wang, X. Zhang, and S. Liu, 'Synthesis of CdTe/TiO2 nanoparticles and their photocatalytic activity', *Mater. Res. Bull.*, vol. 48, no. 10, pp. 4283–4286, Oct. 2013, doi: 10.1016/j.materresbull.2013.06.052.

[196] Y. Gong *et al.*, 'All-solid-state Z-scheme CdTe/TiO2 heterostructure photocatalysts with enhanced visible-light photocatalytic degradation of antibiotic waste water', *Chem. Eng. J.*, vol. 350, pp. 257–267, Oct. 2018, doi: 10.1016/j.cej.2018.05.186.

[197] Y.-S. Li *et al.*, 'Enhanced photocatalytic activities of TiO2 nanocomposites doped with water-soluble mercapto-capped CdTe quantum dots', *Appl. Catal. B Environ.*, vol. 101, no. 1–2, pp. 118–129, Nov. 2010, doi: 10.1016/j.apcatb.2010.09.016.

[198] Q. Wang, X. Yang, L. Chi, and M. Cui, 'Photoelectrochemical performance of CdTe sensitized TiO2 nanotube array photoelectrodes', *Electrochimica Acta*, vol. 91, pp. 330–336, Feb. 2013, doi: 10.1016/j.electacta.2012.12.117.

[199] M. Su, J.-H. Yang, and Z.-P. L. X.-G. Gong, 'Exploring Large-Lattice-Mismatched Interfaces with Neural Network Potentials: The Case of the CdS/CdTe Heterostructure', *J. Phys. Chem. C*, vol. 126, no. 31, 2022.

[200] X. Cai, H. Mirafzal, K. Nguyen, V. Leppert, and D. F. Kelley, 'Spectroscopy of CdTe/CdSe Type-II Nanostructures: Morphology, Lattice Mismatch, and Band-Bowing Effects', *J. Phys. Chem. C*, vol. 116, no. 14, 2012.

[201] W. K. Bae *et al.*, 'Controlled Alloying of the Core–Shell Interface in CdSe/CdS Quantum Dots for Suppression of Auger Recombination', *ACS Nano*, vol. 7, no. 4, 2013.

[202] X. Chen, Y. Lou, A. C. Samia, and C. Burda, 'Coherency Strain Effects on the Optical Response of Core/Shell Heteronanostructures', *Nano Lett.*, vol. 3, no. 6, 2003.

[203] S. Y. Lee, D. Kang, S. Jeong, H. T. Do, and J. H. Kim, 'Photocatalytic Degradation of Rhodamine B Dye by TiO_2 and Gold Nanoparticles Supported on a Floating Porous Polydimethylsiloxane Sponge under Ultraviolet and Visible Light Irradiation', *ACS Omega*, vol. 5, no. 8, pp. 4233–4241, Mar. 2020, doi: 10.1021/acsomega.9b04127.

[204] M. Molaei, F. Farahmandzadeh, T. S. Mousavi, and M. Karimipour, 'Photochemical synthesis, investigation of optical properties and photocatalytic activity of CdTe/CdSe core/shell quantum dots', *Mater. Technol.*, vol. 37, no. 11, pp. 1818–1824, Sep. 2022, doi: 10.1080/10667857.2021.1988040.

[205] Y. Cho, M. Park, J. K. Kim, S. Kim, H. Suk Jung, and J. H. Park, 'Electrochemically controlled CdS@CdSe nanoparticles on ITO@TiO2 dual core–shell nanowires for enhanced photoelectrochemical hydrogen production', *Appl. Surf. Sci.*, vol. 505, p. 144569, Mar. 2020, doi: 10.1016/j.apsusc.2019.144569.

[206] J. Jia, P. Xue, X. Hu, Y. Wang, E. Liu, and J. Fan, 'Electron-transfer cascade from CdSe@ZnSe core-shell quantum dot accelerates photoelectrochemical H2 evolution on TiO2 nanotube arrays', *J. Catal.*, vol. 375, pp. 81–94, Jul. 2019, doi: 10.1016/j.jcat.2019.05.028.

[207] L. Carbone *et al.*, 'Synthesis and Micrometer-Scale Assembly of Colloidal CdSe/CdS Nanorods Prepared by a Seeded Growth Approach', *Nano Lett.*, vol. 7, no. 10, pp. 2942–2950, Oct. 2007, doi: 10.1021/nl0717661.

[208] E. A. Slejko and V. Lughi, 'Upconversion photoluminescence in colloidal CdSe/CdS nanocrystal-based solid films', *Nano-Struct. Nano-Objects*, vol. 26, p. 100742, Apr. 2021, doi: 10.1016/j.nanoso.2021.100742.

[209] H. Seo and S.-W. Kim, 'In Situ Synthesis of CdTe/CdSe Core−Shell Quantum Dots', *Chem. Mater.*, vol. 19, no. 11, 2007.

[210] S. Kim, B. Fisher, H.-J. Eisler, and M. Bawendi, 'Type-II Quantum Dots: CdTe/CdSe(Core/Shell) and CdSe/ZnTe(Core/Shell) Heterostructures', *J. Am. Chem. Soc.*, vol. 125, no. 38, 2003.

[211] N. Gheshlaghi, M. Faraji, and H. S. Pisheh, 'Interfacial strain and shell thickness effect on core squeeze/stretch in core/shell quantum dots', *SN Appl. Sci.*, vol. 2, 2020.

[212] A. K. Zak, W. A. Majid, M. Abrishami, and R. Yousefi, 'X-ray analysis of ZnO nanoparticles by Williamson–Hall and size–strain plot methods', *Solid State Sci.*, vol. 13, no. 1, 2011.

[213] W. W. Yu, L. Qu, W. Guo, and X. Peng, 'Experimental Determination of the Extinction Coefficient of CdTe, CdSe, and CdS Nanocrystals', *Chem. Mater.*, vol. 15, no. 14, pp. 2854–2860, Jul. 2003, doi: 10.1021/cm034081k.

[214] J. Zhang, X. Hu, and Q. Gong, 'Surface defect states of CdTexS1 − x quantum dots', *Phys. Lett. A*, vol. 373, no. 48, pp. 4475-4478, 2009.

[215] X. Xiang, L. Wang, J. Zhang, B. Cheng, J. Yu, and W. Macyk, 'Cadmium Chalcogenide (CdS, CdSe, CdTe) Quantum Dots for Solar-to-Fuel Conversion', *Adv. Photonics Res.*, vol. 3, no. 11, p. 2200065, 2022.

[216] N. Aghoutane, L. Pérez, D. Laroze, M. El-Yadri, and E. Feddi, 'Importance of core and shell sizes in the localization of the electron and hole in the formation of type I or type II excitons in spherical CdSe/ZnTe and CdSe/CdTe quantum dots', *Results Phys.*, vol. 44, p. 106158, 2023.

[217] A. S. Tanwar, R. Parui, R. Garai, M. A. Chanu, and P. K. Iyer, 'Dual "Static and Dynamic" Fluorescence Quenching Mechanisms Based Detection of TNT via a Cationic Conjugated Polymer', *ACS Meas. Sci. Au*, vol. 2, no. 1, 2021.

[218] S. A. B. Shah, S. Ghimire, R. Lesyuk, M. V. Diamanti, V. Lughi, and C. Klinke, 'Tailoring Charge Donor–Acceptor Interaction in CsPbBr3 Perovskite Nanocrystals through Ligand Exchange', *Small Sci.*, vol. 4, no. 5, p. 2300348, 2023.

[219] I. D. Fossé, S. C. Boehme, I. Infante, and A. J. Houtepen, 'Dynamic Formation of Metal-Based Traps in Photoexcited Colloidal Quantum Dots and Their Relevance for Photoluminescence', *Chem. Mater.*, vol. 33, no. 9, pp. 3349-3358, 2021.

[220] B. C. Fitzmorris, J. K. Cooper, J. Edberg, S. Gul, J. Guo, and J. Z. Zhang, 'Synthesis and Structural, Optical, and Dynamic Properties of Core/Shell/Shell CdSe/ZnSe/ZnS Quantum Dots', *J. Phys. Chem. C*, vol. 116, no. 47, 2012.

[221] M. C. Sekhar and A. Samanta, 'Ultrafast Transient Absorption Study of the Nature of Interaction between Oppositely Charged Photoexcited CdTe Quantum Dots and Cresyl Violet', *J. Phys. Chem. C*, vol. 119, no. 27, 2015.

[222] C. Chang, P. Tsai, Y. Chang, and K. Lin, 'Interfacial Electron Transfer from CdSe/ZnS Quantum Dots to TiO_2 Nanoparticles: Size Dependence at the Single-Molecule Level', *ChemPhysChem*, vol. 13, no. 11, pp. 2711–2720, Aug. 2012, doi: 10.1002/cphc.201200037.

[223] S. Jin and T. Lian, 'Electron Transfer Dynamics from Single CdSe/ZnS Quantum Dots to TiO_2 Nanoparticles', *Nano Lett.*, vol. 9, no. 6, pp. 2448–2454, Jun. 2009, doi: 10.1021/nl9011744.

[224] Z. Ning *et al.*, 'Wave-Function Engineering of CdSe/CdS Core/Shell Quantum Dots for Enhanced Electron Transfer to a TiO_2 Substrate', *J. Phys. Chem. C*, vol. 114, no. 35, pp. 15184–15189, Sep. 2010, doi: 10.1021/jp102978g.

[225] S. Chauhan and D. F. Watson, 'Photoinduced electron transfer from quantum dots to TiO_2 : elucidating the involvement of excitonic and surface states', *Phys. Chem. Chem. Phys.*, vol. 18, no. 30, pp. 20466–20475, 2016, doi: 10.1039/C6CP03813A.

[226] N. Rivera-González, S. Chauhan, and D. F. Watson, 'Aminoalkanoic Acids as Alternatives to Mercaptoalkanoic Acids for the Linker-Assisted Attachment of Quantum Dots to TiO_2', *Langmuir*, vol. 32, no. 36, pp. 9206–9215, Sep. 2016, doi: 10.1021/acs.langmuir.6b02704.

[227] P. Lekha, A. Balakrishnan, K. R. V. Subramanian, and S. V. Nair, 'Size dependent electron transfer from CdTe quantum dots linked to TiO2 thin films in quantum dot sensitized solar cells', *Mater. Chem. Phys.*, vol. 141, no. 1, pp. 216–222, Aug. 2013, doi: 10.1016/j.matchemphys.2013.04.047.

[228] M. Cheng, S. Bai, Y. Xia, X. Zhu, R. Chen, and Q. Liao, 'Highly efficient photocatalytic conversion of gas phase CO2 by TiO2 nanotube array sensitized with CdS/ZnS quantum dots under visible light', *Int. J. Hydrog. Energy*, vol. 46, no. 62, pp. 31634–31646, Sep. 2021, doi: 10.1016/j.ijhydene.2021.07.067.